Article

Mapping and engineering RNA-driven architecture of the multiphase nucleolus

Sofia A. Quinodoz[1,2,12], Lifei Jiang[3,12], Aya A. Abu-Alfa[3], Troy J. Comi[4], Hongbo Zhao[1,4], Qiwei Yu[5], Lennard W. Wiesner[1], Jordy F. Botello[3], Anita Donlic[1], Elizabeth Soehalim[4], Prashant Bhat[6,7], Christiane Zorbas[8], Ludivine Wacheul[8], Andrej Košmrlj[9,10], Denis L. J. Lafontaine[8✉], Sebastian Klinge[11✉] & Clifford P. Brangwynne[1,2,3,4,5,10✉]

Biomolecular condensates are key features of intracellular compartmentalization[1,2]. As the most prominent nuclear condensate in eukaryotes, the nucleolus is a multiphase liquid-like structure in which ribosomal RNAs (rRNAs) are transcribed and processed, undergoing multiple maturation steps to form the small (SSU) and large (LSU) ribosomal subunits[3–5]. However, how rRNA processing is coupled to the layered organization of the nucleolus is poorly understood owing to a lack of tools to precisely monitor and perturb nucleolar rRNA processing dynamics. Here we developed two complementary approaches to spatiotemporally map rRNA processing and engineer de novo nucleoli. Using sequencing in parallel with imaging, we found that rRNA processing steps are spatially segregated, with sequential maturation of rRNA required for its outward movement through nucleolar phases. By generating synthetic nucleoli in cells using an engineered rDNA plasmid system, we show that defects in SSU processing can alter the ordering of nucleolar phases, resulting in inside-out nucleoli and preventing rRNA outflux, while LSU precursors are necessary to build the outermost layer of the nucleolus. These findings demonstrate how rRNA is both a scaffold and substrate for the nucleolus, with rRNA acting as a programmable blueprint for the multiphase architecture that facilitates assembly of an essential molecular machine.

Biomolecular condensates have emerged as a ubiquitous feature of intracellular compartmentalization[1,2,6], forming through phase separation and related phase transitions of interacting multivalent biomolecules[7,8]. Nuclear bodies like nucleoli and speckles are examples of such structures, concentrating DNA, RNA and proteins involved in multiple functions, including transcription and RNA processing. Among their protein and nucleic acid components, RNA can have a central role in the formation of various condensates, while the physicochemical environment within condensates is thought to impact their RNA-associated functions[9,10]. However, dissecting this relationship between the structure of condensates and the biochemical reactions occurring within them has remained a key challenge.

The nucleolus provides an ideal model for studying condensate structure–function relationships. It is a multiphase condensate composed of three nested subcompartments: the innermost fibrillar centre (FC), middle dense fibrillar component (DFC) and outer granular component (GC)[11–13] (Fig. 1a). Precursor rRNA (pre-rRNA) is transcribed as a 13.3 kb transcript by RNA polymerase I (Pol I) at the FC–DFC boundary and fluxes radially outward as it is processed and assembled into preribosomal ribonucleoproteins (RNPs)[3,4,14,15]. For example, pre-rRNA is cleaved and modified by small nucleolar RNA (snoRNA)-guided RNPs (snoRNPs) and other processing enzymes as it progresses through the nucleolus. While rRNA maturation correlates with its outward flux, it remains unclear whether rRNA movement between phases is driven by rRNA processing, or is simply due to rRNA processing coinciding with outward transport. This question has been difficult to address owing to the tight coupling between nucleolar structure and function (rRNA transcription and processing): inhibition of Pol I transcription or disruption of rRNA processing induces considerable reorganization of nucleolar morphology[12,16–22]. Despite these connections, how rRNA and its maturation directly contribute to the formation and organization of the multiphase nucleolus and, in turn, whether these phases gate rRNA outflux, remain poorly understood.

Addressing these questions has been hampered by the absence of techniques for dissecting where and when specific pre-rRNA processing steps occur in the nucleolar phases, and how these steps contribute to nucleolar organization. Traditional methods like pulse–chase radiolabelling or northern blotting lack spatial resolution[23,24], while RNA fluorescence in situ hybridization (FISH) reveals spatial localization but not processing dynamics[25,26]. Moreover, approaches to understand nucleolar

[1]Department of Chemical and Biological Engineering, Princeton University, Princeton, NJ, USA. [2]Howard Hughes Medical Institute, Chevy Chase, MD, USA. [3]Department of Molecular Biology, Princeton University, Princeton, NJ, USA. [4]Omenn-Darling Bioengineering Institute, Princeton University, Princeton, NJ, USA. [5]Lewis-Sigler Institute for Integrative Genomics, Princeton University, Princeton, NJ, USA. [6]Division of Biology and Biological Engineering, California Institute of Technology, Pasadena, CA, USA. [7]David Geffen School of Medicine, University of California, Los Angeles, Los Angeles, CA, USA. [8]RNA Molecular Biology, Fonds de la Recherche Scientifique (F.R.S./FNRS), Université libre de Bruxelles (ULB), Gosselies, Belgium. [9]Department of Mechanical and Aerospace Engineering, Princeton, NJ, USA. [10]Princeton Materials Institute, Princeton, NJ, USA. [11]Laboratory of Protein and Nucleic Acid Chemistry, The Rockefeller University, New York, NY, USA. [12]These authors contributed equally: Sofia A. Quinodoz, Lifei Jiang. ✉e-mail: denis.lafontaine@ulb.be; klinge@rockefeller.edu; cbrangwy@princeton.edu
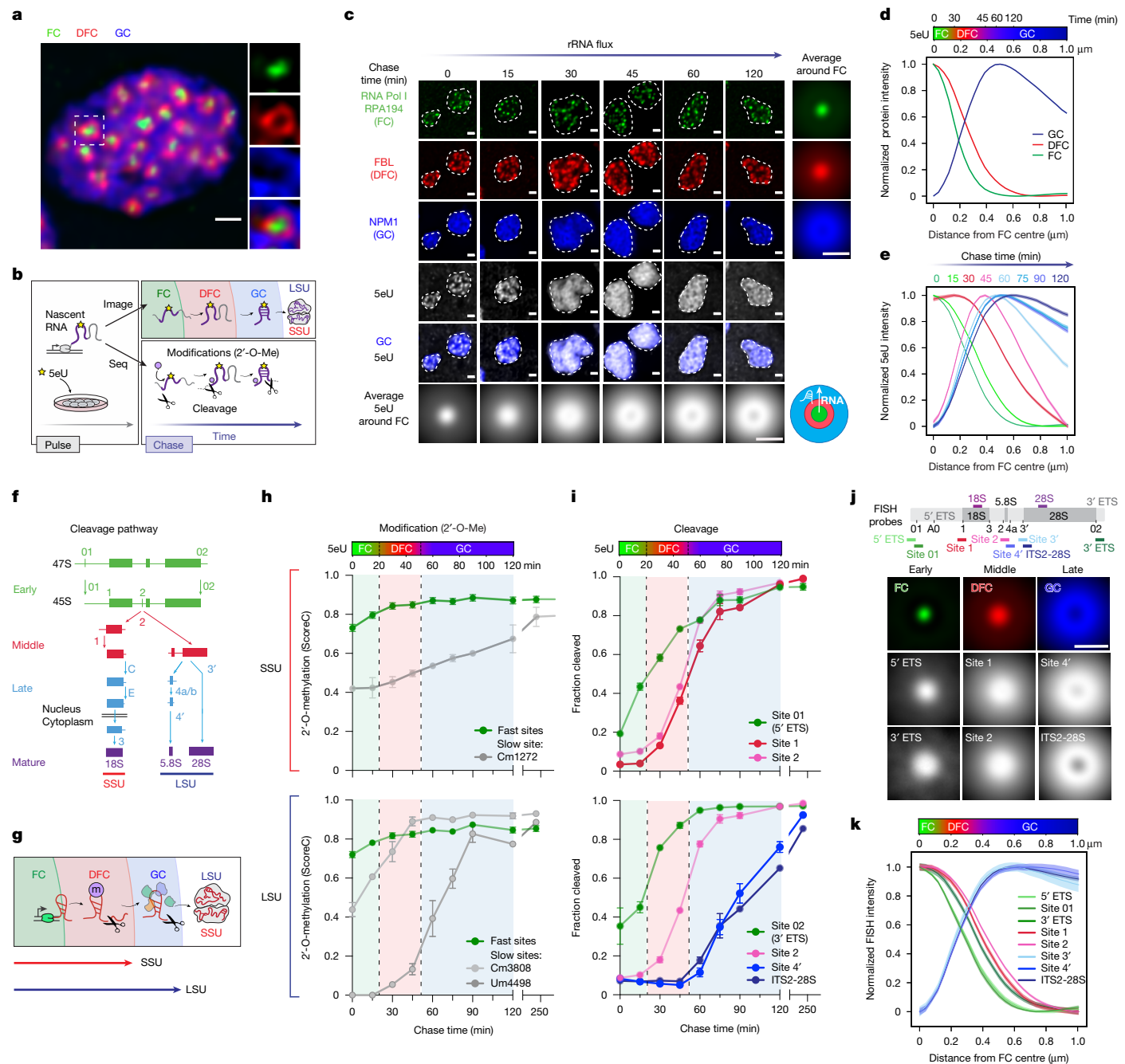
Fig. 1 | Sequencing and imaging of nascent rRNA flux provides a spatiotemporal map of processing in the nucleolus. FCs, DFCs and GCs in MCF10A cells were visualized through RNA Pol I subunit RPA194 (immunofluorescence (IF)), FBL (IF) and endogenously tagged mTagBFP2–NPM1, respectively. **a**, The three nucleolar phases: FC (green), DFC (red) and GC (blue). **b**, Cells were pulsed with 5eU (15 min) to label nascent RNA and chased to measure the rRNA flux (imaging) or cleavage and modification (sequencing). **c**, The radial outflux of 5eU-labelled pre-rRNA over time in nucleoli (dashed lines); the averaged signal around the FCs is shown. **d**, Min–max-normalized FC, DFC and GC intensities by distance from the FC centre from 4,274 nucleoli. The colour bar indicates FC, DFC and GC localization. **e**, Min–max-normalized 5eU intensities by distance from the FC centre across chase timepoints. n = 717, 459, 499, 603, 470, 451, 550 and 525 nucleoli. **f**, Pre-rRNA cleavage steps categorized as early (green), middle (red), late (blue) and mature (purple) based on **i**.

g, Schematic of pre-rRNA cleavage, modification (m), and outflux during assembly into SSU (in the FC and DFC) and LSU (in the FC, DFC and GC) based on **i**. **h**, 18S and 28S pre-rRNA 2′-O-methylation (2′-O-Me) (ScoreC) detected using 5eU–seq over time. The colour bar relates the chase time to 5eU peak localization (Extended Data Fig. 2a). The dashed lines demarcate the phase boundaries. n = 2 per timepoint. **i**, The fraction of pre-rRNA cleaved at early, middle and late sites over time. n = 2 per timepoint. **j**, Schematic of the RNA-FISH probes (top). Bottom, the averaged intensity around FCs (example images are shown in Extended Data Fig. 2e). **k**, The min–max-normalized RNA-FISH intensity by distance from the FC centre. n = 72 (5′ ETS), 95 (3′ ETS), 24 (site 01), 111 (site 1), 230 (site 2), 38 (site 3′), 105 (site 4′), 318 (ITS2-28S), 72 (18S) and 310 (28S) nucleoli. For **a**, **c** and **j**, scale bars, 1 μm. Data are mean ± s.e.m. (**d**, **e**, **h**, **i** and **k**).

assembly are limited by the repetitive nature of rDNA genes, which makes it challenging to endogenously mutate and directly study how the rRNA sequence contributes to nucleolar morphology[27–29]. A number of studies

have used 'bottom-up' in vitro reconstitution approaches using purified nucleolar proteins and rRNAs to form nucleoli mimics[13,30,31], but they are vast simplifications of the complexity of real nucleoli.

Here, to overcome these challenges, we introduce and use two complementary approaches that reveal insights into the relationship between rRNA processing and nucleolar structure. By combining a pulse–chase nucleotide analogue approach with sequencing and imaging, we precisely measure the kinetics of pre-rRNA cleavage and modification at single-nucleotide resolution. Our findings reveal that rRNA processing occurs in a spatially segregated manner within the nucleolus, with sequential maturation steps driving the outward progression of rRNA through nucleolar phases. Most small-subunit assembly steps occur within the DFC phase, while large-subunit assembly steps occur in both the DFC and GC phases. We also use an engineerable rDNA plasmid system to assemble synthetic nucleoli in living cells. By mutating rDNA, we find that LSU precursors are necessary for the formation of the GC phase. Notably, perturbing SSU pre-rRNA processing in both synthetic and endogenous nucleoli leads to a marked 'inversion' of nucleolar phases and a lack of rRNA outflux from the DFC, establishing an essential role of SSU processing in nucleolar phase organization and RNA flux through the nucleolar phases. Finally, we develop a mathematical model predicting how altered concentrations of rRNA intermediates could change interfacial tensions to shape the multiphase nucleolus. Taken together, our study provides a detailed dissection of how rRNA sequences and processing build and arrange the nucleolar phases, providing a programmable blueprint to assemble the multiphase nucleolus that contributes to proper rRNA flux and ribosome assembly.

Mapping rRNA processing in time and space

To measure rRNA processing in time and space, we developed a 5-ethynyl uridine (5eU) nucleotide analogue-based pulse–chase labelling approach to measure both the nucleolar RNA localization using super-resolution fluorescence microscopy and the processing state using RNA sequencing (RNA-seq; Fig. 1b). This approach requires modifying existing nascent RNA-seq strategies[32] to remove the background signal arising from the abundance of mature rRNAs, which we found impairs the detection of nascent pre-rRNA processing (Extended Data Fig. 1a–d). In brief, we labelled nascently transcribed RNA for 15 min (pulse) with the 5eU nucleotide analogue and then chased with excess unlabelled uridine over time. As 5eU nucleotides can be conjugated with a dye using click chemistry (5eU-imaging)[19], we can visualize the radial outflux of nascently transcribed rRNA from the FC–DFC interface, where RNA Pol I is synthesizing rRNA, to the outer GC layer over time[33] (Fig. 1b). Alternatively, 5eU nucleotides can be conjugated with biotin, enabling the purification of these nascently transcribed RNAs with streptavidin beads followed by sequencing (5eU–seq)[32] to measure both rRNA cleavage and modification (2′-O-methylation using RiboMethSeq[34]) steps in one experiment, at the single-nucleotide resolution (Extended Data Fig. 1a,b,h,i). Importantly, 5eU incorporation does not substantially impair pre-rRNA synthesis, processing or modification (Extended Data Fig. 1e–g).

Using this approach, we can quantitatively measure both rRNA localization (Fig. 1c–e and Extended Data Fig. 2a,b) and processing (Fig. 1f–i) over time. We find that the timing of rRNA cleavage steps is correlated with rRNA movement through the nucleolar phases (Fig. 1i). Specifically, early cleavage steps (sites 01 and 02) begin immediately after transcription (around 0–15 min) (Fig. 1i), which coincides with 5eU rRNA localization near the FC–DFC boundary at early chase timepoints (Fig. 1c–e), consistent with these cleavage steps occurring co-transcriptionally or immediately after transcription[35,36]. Next, we observed subsequent cleavage steps (sites 1 and 2) as rRNA fluxes from the DFC to GC (about 30–60 min), and late cleavages occur as RNA fluxes from the GC to nucleoplasm (around 60–120 min) (Fig. 1c–e,i). This spatiotemporal map suggests that nucleolar SSU-processing (18S rRNA precursors) steps may be largely completed before RNA enters the GC, while LSU-processing (5.8S/28S rRNA precursors) steps, which

take markedly longer, may occur throughout the nucleolus (Fig. 1f,g,i). This is consistent with research in yeast showing that the nuclear dwelling time of SSU precursors is far less than those of LSU[37]. Moreover, the vast majority of 2′-O-methylations on rRNA occur within 30 min after transcription (defined as fast sites; Fig. 1h), consistent with findings that most 2′-O-methylations are placed co-transcriptionally in yeast[36]. However, a handful of post-transcriptional 2′-O-methylations (for example, 28S Um4498, Gm4499) occur substantially later (around 60–90 min) (Fig. 1h and Extended Data Fig. 1h–j), corresponding to when 5eU rRNA moves into the GC phase.

To validate the 5eU–seq and imaging approach, we performed RNA SABER-FISH[38] (hereafter, RNA-FISH) using cleavage-spanning probes designed to no longer hybridize after cleavage (Fig. 1f,j). RNA-FISH shows early pre-rRNA species (site 01) at the FC–DFC boundary, consistent with previous work[25] (Fig. 1j,k and Extended Data Fig. 2c–e). Site 1 and 2 RNA-FISH signals are primarily localized within the DFC and at the DFC–GC boundary (Fig. 1j,k and Extended Data Fig. 2c–e), consistent with their cleavages occurring as 5eU rRNA moves from the DFC to GC (around 30–60 min) (Fig. 1i). Late LSU cleavage steps (such as ITS2), which occur (around 60–120 min) after 5eU RNA enters the GC (Fig. 1i), are indeed localized within the GC (Fig. 1j,k and Extended Data Fig. 2c–e), confirming that the late LSU-processing steps occur in the GC, while nucleolar SSU-processing steps are completed before RNA enters the GC (Fig. 1g,i). Using a kinetic model to deconvolve the contributions of individual rRNA intermediates, these FISH data were directly compared to our 5eU–seq and imaging data and appear comparable (Supplementary Note 1). Taken together, this map of where different rRNA processing steps occur demonstrates that the cleavage steps are spatially segregated in different phases of the nucleolus.

Processing controls flux and morphology

Our findings above show that rRNA processing is correlated with rRNA outflux through the nucleolus; however, it is unclear whether these processing steps are strictly required for rRNA movement through the nucleolus. To test this, we perturbed rRNA processing with chemical inhibitors or knockdowns (KDs) of processing factors and measured the impact on rRNA processing, flux and nucleolar morphology (Fig. 2a). First, we treated cells with flavopiridol (FVP)—a CDK9 (Pol II) inhibitor that is known to block rRNA processing but not Pol I transcription[17]. Using 5eU–seq to label nascently transcribed rRNA after 1 h of FVP treatment, we observed a major impairment of all but one rRNA cleavage step—only the earliest co-transcriptional 01 cleavage proceeds normally (Fig. 2b and Extended Data Fig. 3a,b,f). Notably, 2′-O-methylation levels also decreased substantially (Fig. 2d and Extended Data Fig. 3c–e), with stronger reductions on 28S than 18S (Extended Data Fig. 3g). Consistent with previous studies, FVP-treated nucleoli form a typical 'necklace' morphology[17], whereby the outer GC phase appears detached from the inner phases (Fig. 2e and Extended Data Fig. 4a,c).

Given that FVP inhibits almost all of the processing steps, we next performed pulse–chase 5eU imaging analysis of cells pretreated with FVP for 1 h to determine whether unprocessed rRNA species can flux into the GC phase. While newly transcribed rRNAs move into the GC after a 60-min chase in the DMSO-control cells (Fig. 2c), unprocessed 5eU-labelled rRNAs in the FVP-treated cells accumulate around the GC surface, but do not partition into the GC (Fig. 2c and Extended Data Fig. 4d,e). RNA-FISH confirmed that only processed rRNA enters the GC: probes targeting early and middle cleavage sites appear excluded from the GC, while late probes localize inside the GC (Extended Data Fig. 4f). Supporting this, FVP-washout experiments demonstrated that restarting pre-rRNA processing led to 5eU-labelled RNA and processed rRNA species entering the GC, coincident with the reattachment of the FC and DFC with the GC phase, within about 30–60 min (Extended Data Fig. 4b,c,f–h and Supplementary Videos 1 and 2). This timing is consistent with when rRNA cleavage and flux into the GC occurs (around
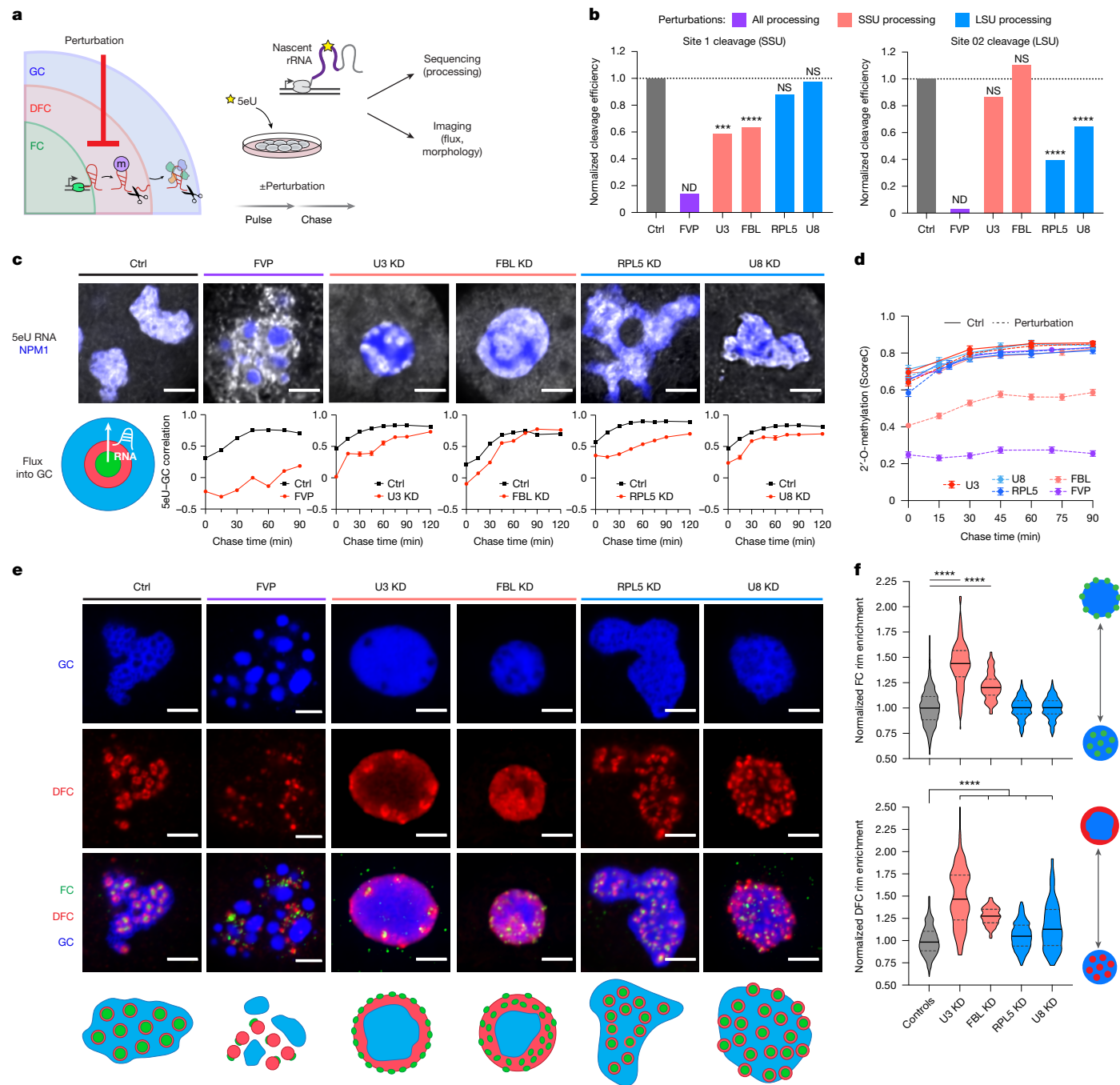
Fig. 2 | Impaired rRNA processing impacts rRNA flux and alters the nucleolar morphology. a, Pre-rRNA processing was perturbed in MCF10A cells and analysed using 5eU–seq (processing) or 5eU imaging (flux and morphology). **b**, The normalized cleavage efficiency (treatment versus control; Methods) for 5′ ETS (1) or 3′ ETS (02) sites measured by 5eU–seq after treatment with 2 µM FVP (general processing inhibitor, purple), KD of SSU-processing factors (U3 snoRNA or FBL, red) or LSU-processing factors (RPL5 or U8 snoRNA, blue). *P* values were calculated using two-tailed *t*-tests; ***$P = 0.0004$, ****$P < 0.0001$. $n = 12$ (FVP), 8 (U3), 15 (FBL), 8 (RPL5) and 6 (U8) measurements. ND, not determined; NS, not significant; estimation of cleavage efficiency and statistical testing was not possible for FVP due to complete cleavage inhibition (Extended Data Fig. 3f). **c**, Representative images of 5eU-labelled RNA (white) in nucleoli (mTagBFP2–NPM1) after a 60 min chase in control and treated cells (top). Bottom, 5eU–GC (NPM1) correlation from 0–120 min. $n \geq 50$ cells per

timepoint per condition. Example images are provided in Extended Data Figs. 4e and 6. **d**, The average 18S and 28S rRNA 2′-O-methylation levels (ScoreC) over 0–90 min from 5eU–seq for controls (solid lines) and treatments (dashed). $n = 101$–208 measurements per timepoint. **e**, Representative images and schematics of GC (NPM1, blue), DFC (FBL, red) and FC (RPA194, green) (IF) for all conditions except FBL KD, where mTagBFP2–NPM1, NOP56–mCherry and RPA16–GFP are visualized. RPA194 puncta outside the nucleoli are immunostaining background, and were not observed in the fluorescence-tagged lines (Extended Data Fig. 5d,e). **f**, FC and DFC nucleolar rim enrichment in controls and perturbations (normalized to control). The violin plots show the median (solid line) and quartiles (dashed lines). Statistical analysis was performed using two-tailed Mann–Whitney *U*-tests; ****$P < 0.0001$. $n = 1,116$ (controls), 97 (FBL), 228 (RPL5), 153 (U3) and 105 (U8) cells. All scale bars, 3 µm. For **c** and **d**, data are mean ± s.e.m.

30–60 min) (Fig. 1c,i). Taken together, our results suggest that rRNA processing is required for the flux of rRNAs into the GC, and that this processing-gated movement of RNAs has a key role in shaping nucleolar morphology.

As FVP broadly affects rRNA processing and other cellular functions (Pol II inhibition)[16,39], we next tested more specific perturbations of rRNA processing. We used antisense oligonucleotides (ASOs) to deplete the box C/D snoRNA U3 (ref. 40), a key SSU processome component that is involved in 5′ ETS cleavage[40,41] (Extended Data Fig. 5a–c). U3 KD disrupted the two cleavages within the 5′ ETS (01 and 1) in the SSU pathway (Fig. 2b and Extended Data Fig. 3h) while LSU processing remained unaffected, as expected[40] (Fig. 2b and Extended Data Fig. 3h). Given that rRNA processing rates were reduced, we next performed 5eU imaging and found that RNA flux into the GC was slowed as well (Fig. 2c). Together, these data show that 5eU–seq enables quantitative measurement of rRNA cleavage and modification rates at single-nucleotide resolution and, when coupled with 5eU imaging, reveals that pre-rRNA processing rates are tightly connected to rRNA movement through the nucleolus.

SSU defects cause 'inside-out' nucleoli

We next examined the consequences of processing defects on nucleolar morphology after U3 KD. Notably, U3 KD results in an 'inside-out' morphology whereby the FC and DFC phases move towards the nucleolar periphery, reversing the order of the nucleolar phases (Fig. 2e,f and Extended Data Fig. 5d,e). This phenotype begins within 8 h and fully develops within 24–48 h (Extended Data Fig. 5h–j); furthermore, the number of nucleoli reduces from about 2–3 per cell to 1 per cell after U3 KD (Extended Data Fig. 5g). Importantly, the inversion is distinct from the well-known nucleolar segregation phenotype[17,22], whereby FCs also move towards the periphery of the nucleolus, but fuse to form large caps due to transcriptional inhibition (Extended Data Fig. 5e,f). Instead, the number of FCs remains high after U3 snoRNA KD, consistent with active Pol I transcription (Extended Data Fig. 5e,f).

We next examined whether nucleolar inversion could be phenocopied by knocking down fibrillarin (FBL), another U3 snoRNP component (Extended Data Fig. 5k–l). 5eU–seq reveals that partial KD of FBL slows SSU cleavage and broadly reduces modifications (Fig. 2b,d and Extended Data Fig. 3j,k), consistent with its function as a 2′-O-methyltransferase and SSU processome component[41,42]. Notably, the levels of 28S modifications change more substantially than 18S (Extended Data Fig. 3k), except for the late-forming Gm4499 modification, not placed by FBL[43], which is unaffected (Extended Data Fig. 5m). FBL KD also results in a partially inverted morphology, like that seen with U3 KD (Fig. 2e,f), underscoring the role of SSU processing in nucleolar morphology. Inversion is not a generic trait of processing defects, as depletion of RPL5 (uL18) or the box C/D snoRNA U8, which are primarily involved in LSU processing, results in distinct nucleolar morphologies and slowed rRNA flux (Fig. 2c,e,f and Extended Data Figs. 5n–p and 6). In addition to impaired LSU processing (Fig. 2b), these RPL5 and U8 KDs also impact certain sites in the SSU pathway (Extended Data Fig. 3l,n), consistent with studies showing that LSU-processing defects can impair SSU maturation[18,40]. Note that 2′-O-methylation is not broadly impacted after U3, U8 or RPL5 KD (Extended Data Fig. 3i,m–o). Together, these findings suggest that rRNA processing shapes both nucleolar morphology and rRNA flux.

Engineering synthetic nucleoli in cells

To better understand how pre-rRNA processing shapes nucleolar morphology, we engineered synthetic nucleoli in living cells using a plasmid system that was previously shown to produce mature ribosomal subunits[44,45]. These rDNA plasmids contain unique sequences in 18S and 28S (18S* and 28S*), enabling visualization of plasmid rRNA using

FISH[44,45] (Fig. 3a and Extended Data Fig. 7a). Transient transfection led to the formation of a de novo nucleolus with characteristic FCs and ring-like DFCs embedded within a GC phase, recapitulating the size and morphology of native nucleoli (Fig. 3b,c and Extended Data Fig. 8a,b and 9b). Synthetic nucleoli were distinguished from native nucleoli using FISH for both plasmid-specific sequences (18S*/28S*) and endogenous rRNA sequences absent in the plasmid (Δ1,2,3 segments of 5′ ETS) (Fig. 3a–d and Extended Data Fig. 8c). Moreover, we observed plasmid-derived rRNAs in the cytoplasm (Fig. 3b,f,h), where they incorporate into monosomes and polysomes (Extended Data Fig. 8d), demonstrating that they are functional. Finally, despite not being tethered to chromosomes, synthetic nucleoli recruit heterochromatin, marked by DNA and H3K9me2/3, to their periphery—another hallmark of endogenous nucleoli[46–48] (Fig. 3e and Extended Data Fig. 10a).

Notably, synthetic nucleoli sometimes fuse with endogenous nucleoli, generating hybrid nucleoli containing endogenous and plasmid-derived rRNA (Fig. 3b–d). In these hybrids, 18S* rRNA localizes in discrete territories while 28S* rRNA spreads throughout the GC (Extended Data Fig. 8e). This is consistent with our observations that LSU processing continues into the GC and takes much longer than SSU processing (Fig. 1i).

LSU precursors build the GC phase

Given the spatiotemporal differences in SSU and LSU processing observed in these synthetic nucleoli (Extended Data Fig. 8e) and 5eU–seq (Fig. 1i), we used this engineerable system to test whether SSU or LSU precursors independently shape the nucleolar phases. To do this, we generated truncated plasmids expressing only SSU or LSU pre-rRNAs (Fig. 3f and Extended Data Fig. 7b). Notably, plasmids expressing only SSU precursors form ring-like DFC structures like those in native nucleoli, but lack a surrounding GC (Fig. 3f,g). These synthetic structures recruit FC and DFC components (such as the Pol I subunit RPA194 and the SSU processome component NOP56) (Figs. 3f,g and 4f), but lack GC components, such as the well-established GC marker NPM1 and the two LSU-processing factors SURF6 and RRP1 (Fig. 3f,g and Extended Data Fig. 8f). This is consistent with previous findings showing a partial 18S rRNA sequence, which failed to recruit NPM1[29]. Conversely, plasmids encoding only a large-subunit precursor (5.8S and 28S pre-rRNAs) generate a synthetic structure containing both DFC and GC components (Fig. 3f,g), suggesting that LSU rRNA is necessary to build the GC phase. Nonetheless, the ring-like DFC morphology within LSU-only nucleoli was less pronounced, indicating that SSU pre-rRNAs have a key role in shaping the DFC.

Notably, 18S rRNA expressed from the SSU-only plasmid is exported into the cytoplasm (Fig. 3f,h) and incorporated into monosomes and polysomes (Extended Data Fig. 8d), further suggesting that the GC may be dispensable for SSU processing (Supplementary Note 3). Conversely, a signal for 28S* rRNA from the LSU-only plasmid was not observed in the cytoplasm, even when co-transfected with an SSU-only plasmid, suggesting that LSU assembly is compromised in the absence of upstream SSU pre-rRNA elements (Fig. 3f,h, Extended Data Fig. 8g,h and Supplementary Note 4). Taken together, these findings demonstrate that LSU precursors, but not SSU precursors, actively build the GC phase, consistent with LSU precursors undergoing cleavage in the GC.

SSU processing drives nucleolar layering

Having shown that plasmid-expressed pre-rRNAs recruit assembly factors generating each nucleolar subphase, we next used this system to directly examine how rRNA processing shapes nucleolar morphology. Indeed, although altered nucleolar morphology is often linked to rRNA processing defects[18,49,50], it remains unclear whether this arises directly through defective processing or secondary effects such as cellular stress. This engineered plasmid system enables us to directly
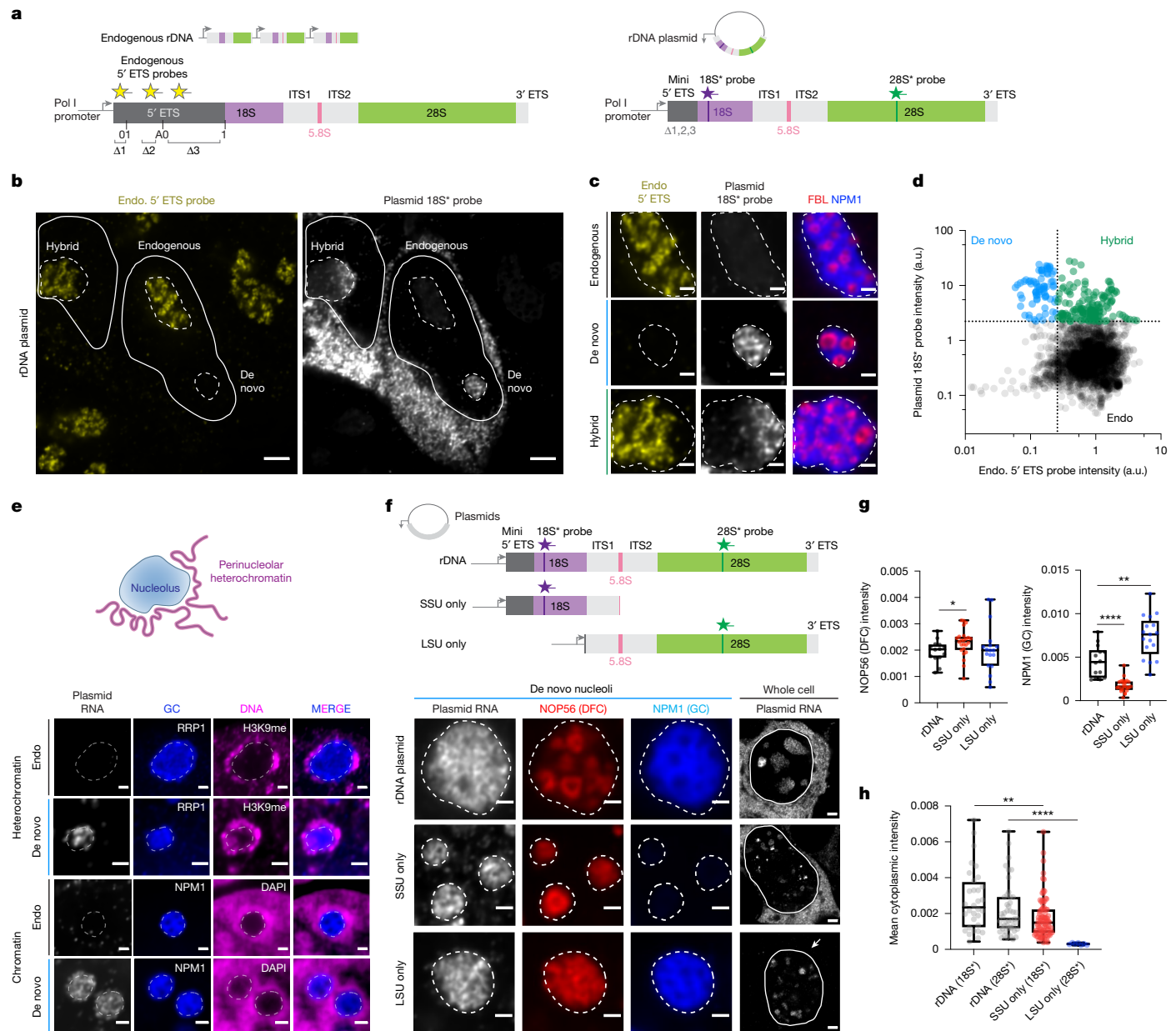
Fig. 3 | Engineered synthetic nucleoli in cells recapitulate normal multiphase architecture with the expression of the LSU precursors required for GC recruitment. a, Schematics of endogenous rDNA and a plasmid expressing an rDNA sequence containing three deletions (Δ1, Δ2 and Δ3) in the 5′ ETS region and unique insertions in 18S and 28S (18S* and 28S*). **b**, RNA-FISH detection of endogenous pre-rRNA (endo 5′ ETS probes; yellow) and plasmid-derived pre-rRNA (18S* probe; white) in HEK293T cells. The dashed lines show individual nucleoli; the solid lines indicate individual nuclei. **c**, Representative images of nucleoli classified as de novo (plasmid derived), endogenous and hybrid (fusion), labelled for DFC (FBL IF) and GC (NPM1 IF). The FISH probe control is shown in Extended Data Fig. 8c. **d**, RNA-FISH intensities of 18S* and endogenous 5′ ETS probes across nucleolar classes. a.u., arbitrary units. **e**, Heterochromatin (H3K9me2/3) and chromatin (DAPI) staining around endogenous and de novo nucleoli (GC: RRP1 IF, NPM1 IF). **f**, Schematics of SSU-only and LSU-only plasmids with truncated rDNA sequences (Extended Data Fig. 7a,b). Left, representative

images of de novo nucleoli formed from rDNA, SSU-only and LSU-only plasmids, visualized by RNA-FISH (28S* for rDNA and LSU only, 18S* for SSU only) and nucleolar markers DFC (NOP56–mCherry), GC (mTagBFP2–NPM1). Right, the corresponding cytoplasmic FISH signals. **g**, Quantification of the mean nucleolar DFC (NOP56–mCherry) and GC (mTagBFP2–NPM1) intensity from **f**. *$P = 0.0248$, **$P = 0.0012$, ****$P < 0.0001$. $n = 24$ (wild type, WT), 14 (SSU only) and 17 (LSU only) nucleoli. **h**, Quantification of cytoplasmic RNA-FISH intensities for rDNA, SSU-only and LSU-only plasmids from **f**. **$P = 0.0016$, ****$P < 0.0001$. $n = 32$ (WT; 18S* rRNA), 47 (WT; 28S* rRNA), 90 (SSU-only) and 7 (LSU-only) cells. Scale bars, 3 μm (**b** and **f** (right; whole cells)) and 1 μm (others). The box plots show the median (centre lines), 25th–75th percentiles (box limits) and minimum–maximum values (whiskers). HEK293T cells were used for all of the experiments. Statistical analysis was performed using two-tailed Mann–Whitney U-tests.

test the effect of rRNA processing on nucleolar architecture without broad changes to cellular function.

As KD of U3 snoRNP components (that is, U3 snoRNA or FBL) results in inverted nucleoli (Fig. 2e), we predicted that designing sequence-specific changes in the plasmid rDNA to block U3-mediated

processing should result in a similar morphological inversion. We designed plasmids containing U3 snoRNA in addition to the rDNA locus (Fig. 4a). Using the human SSU processome structure as a template[44], we mutated two sites (5′ and 3′ hinges) within the 5′ ETS rRNA spacer that directly base-pair with U3 snoRNA[51–53] (Fig. 4a,b and Extended Data
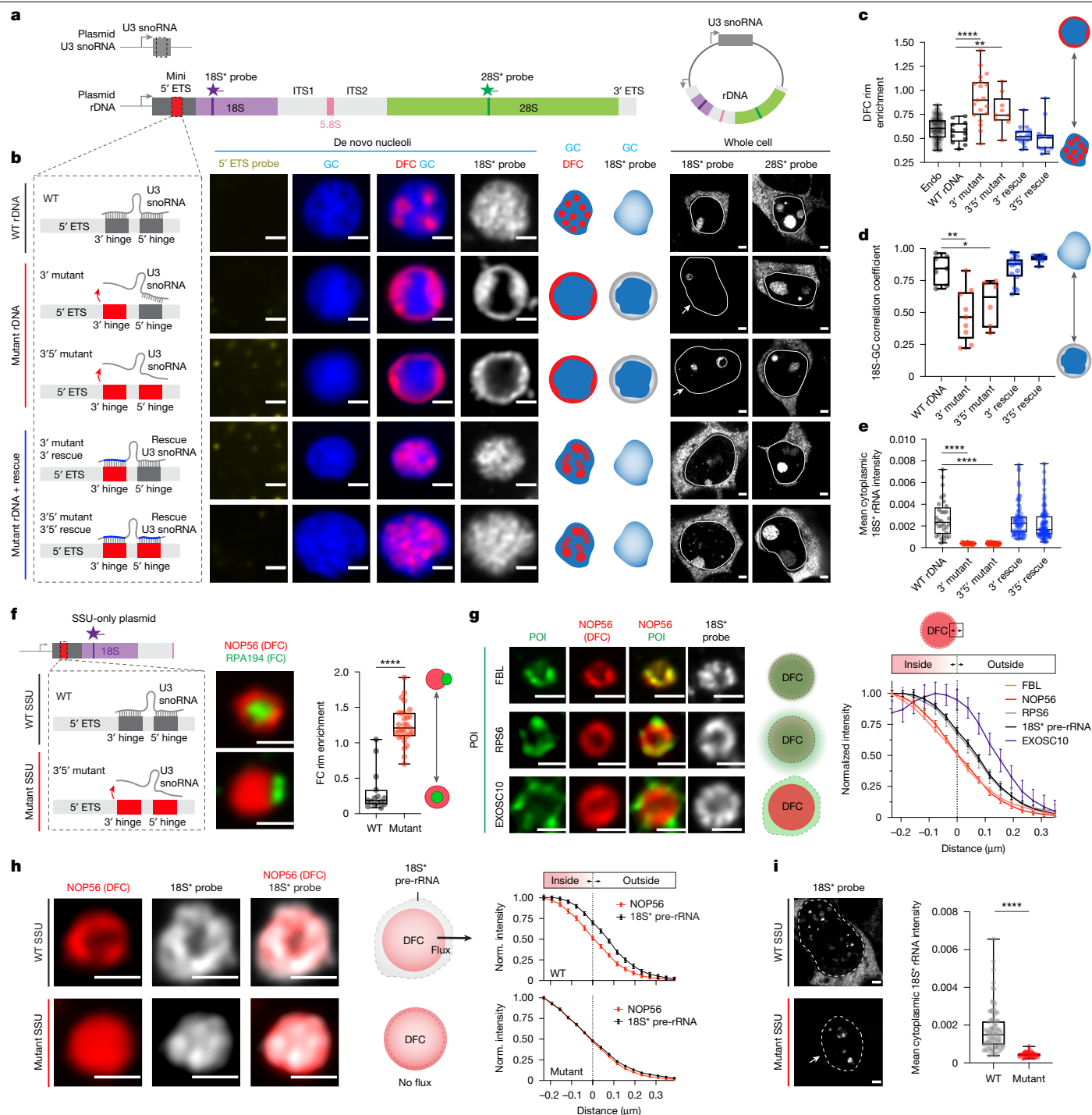
Fig. 4 | U3-mediated SSU processing drives the layering of the multiphase nucleolus and rRNA outflux. a, Plasmids co-expressing U3 snoRNA and rDNA with various mutations (red) (Extended Data Fig. 7c–g). **b**, Synthetic nucleoli from normal, 3' and 3'5' hinge mutants or base-pairing-rescued plasmids, visualized by GC (mTagBFP2–NPM1), DFC (NOP56–mCherry), identified by a lack of endogenous rRNA and the presence of 18S* rRNA. Right, cytoplasmic 18S* and 28S* rRNA signals. Scale bars, 1 μm (left), 3 μm (right). The solid lines indicate nuclei; the arrows indicate a lack of cytoplasmic 18S* signal. See Extended Data Fig. 9a,b for morphologies reproduced with IF and all phases visualized. **c**, Quantification of DFC rim enrichment. ****$P < 0.0001$, **$P = 0.0024$. $n = 95, 12, 19, 9, 18$ and 13 nucleoli. **d**, The Pearson correlation between 18S* rRNA and NPM1. *$P = 0.0221$, **$P = 0.0012$. $n = 7, 9, 6, 15$ and 8 nucleoli. **e**, Quantification of the cytoplasmic 18S* signal from **b**. ****$P < 0.0001$. $n = 32, 38, 58, 79$ and 102 cells. **f**, Morphology (left) and FC rim enrichment score (right) of de novo

nucleoli (FC, RPA194 IF; DFC, NOP56–mCherry) from WT ($n = 15$) or 3'5' hinge mutant ($n = 29$) SSU-only plasmids (Extended Data Fig. 7b). ****$P < 0.0001$. **g**, Localization of proteins of interest (POI, green: FBL (IF), EXOSC10 (IF) and RPS6–Halotag) relative to DFCs (NOP56–mCherry) of WT SSU-only nucleoli (left). Right, the radial distribution of 18S* RNA and POIs around the DFC boundary (dashed line, 0 μm). $n = 74$ (Nop56, 18S), 87 (FBL), 21 (RPS6) and 12 (EXOSC10) nucleoli. **h**, The 18S* RNA distribution around DFCs (NOP56) in WT ($n = 74$) versus mutant ($n = 164$) SSU-only nucleoli. **i**, The cytoplasmic 18S* rRNA levels from WT ($n = 90$) and mutant SSU ($n = 34$) plasmids. Scale bar, 3 μm. ****$P < 0.0001$. Statistical analysis was performed using two-tailed Mann–Whitney U-tests. For **g** and **h**, data are mean ± s.e.m. Scale bars, 1 μm (**f**–**h**). The box plots in **c**–**f** and **i** show the median (centre lines), 25th–75th percentiles (box limits) and minimum–maximum values (whiskers). HEK293T cells were used for all experiments.
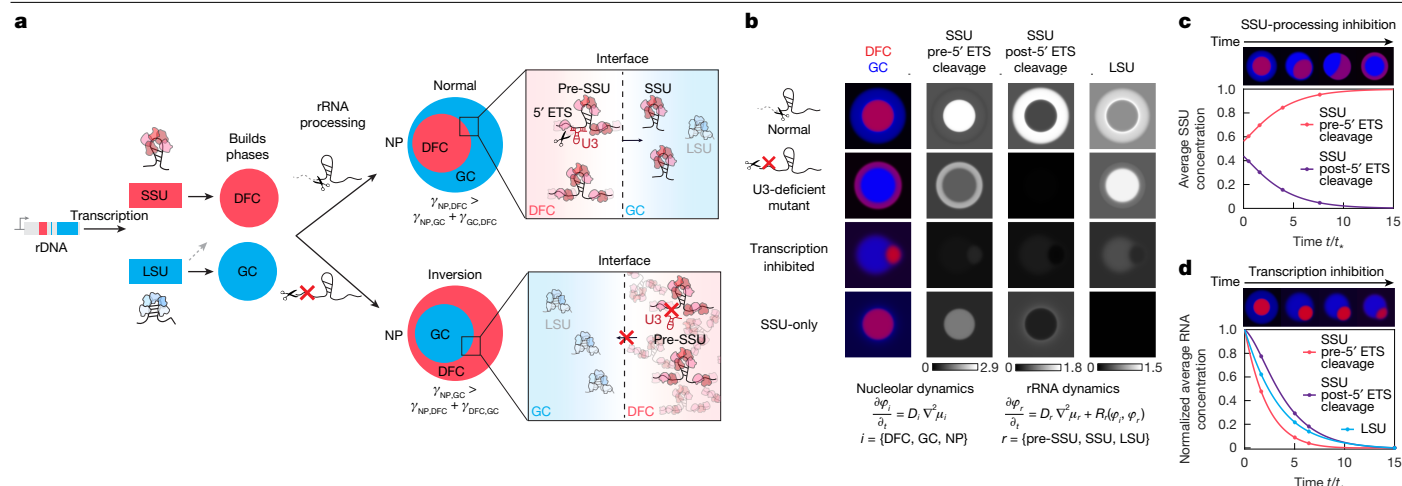
Fig. 5 | An RNA-dependent multiphase model of nucleolar architecture.
a, The proposed model of how rRNA transcription and processing shape the multiphase nucleolus. A 13.3 kb pre-rRNA is transcribed from rDNA, processed and cleaved to assemble the SSU and LSU. Here we show that the LSU precursors are necessary for assembling the nucleolar GC phase (blue) and SSU processing drives the ordering of the DFC (red) and GC (blue) phases. Different arrangements of multiphase structures (such as normal or inversion) can arise from changes in interfacial tensions across multiple interfaces: nucleoplasm (NP)–DFC ($\gamma_{NP,DFC}$), NP–GC ($\gamma_{NP,GC}$) and GC–DFC ($\gamma_{GC,DFC}$). Under normal U3-mediated cleavage of the 5′ ETS from SSU pre-rRNA, the DFC localizes inside the GC. After impaired U3-mediated SSU processing, SSU pre-rRNAs build up in the DFC phase and no longer flux into the GC phase. This results in a change in the interfacial tensions and the nucleolar morphology inverts, whereby the GC is now enveloped by the DFC. **b**, Different nucleolar morphologies are recapitulated in a phase-field model that considers the partitioning of different rRNA precursors (for example, SSU before and after 5′ ETS cleavage) into the different nucleolar phases (DFC and GC). For simplicity, the FC and DFC are modelled as one nucleolar phase. Changes in U3-mediated processing, RNA Pol I transcription or LSU production (SSU-only) alter the concentrations of rRNA precursors in each phase, resulting in different nucleolar morphologies. **c**, Modelling of impaired SSU processing (5′ ETS cleavage) over time leads to an accumulation of SSU precursors (before 5′ ETS cleavage) and inversion of the nucleolar phases. **d**, Modelling of RNA Pol I transcriptional inhibition over time; a decreased concentration (normalized to the concentration at $t = 0$) of all SSU and LSU rRNA precursors results in the nucleolar cap morphology.

Fig. 7c–g). These constructs formed synthetic nucleoli that recapitulate the inversion phenotype observed after U3 KD, with FCs and DFCs localizing at the GC periphery (Figs. 2e and 4b,c and Extended Data Fig. 9a,b). Inversion is observed with multiple DFC markers (Extended Data Fig. 9a,c), including FBL and NOP56 (components of box C/D snoRNPs), NOPP140 (important for snoRNP biogenesis and function), UTP23, ESF1 and KRR1 (SSU assembly factors)[44,54], as well as GC marker NPM1 and LSU assembly factors RRP1 and SURF6 (ref. 45). Notably, the co-existence of a normal endogenous nucleolus in the same cell as an inverted synthetic nucleolus demonstrated that inversion is a direct result of impaired SSU processing rather than altered cellular function (Extended Data Fig. 9d).

Inspired by previous research in yeast[51], we next produced U3 variants to rescue base-pairing with the mutant rRNA (Fig. 4b and Extended Data Fig. 7c–g). These compensatory mutations largely restored the order of nucleolar phases (Fig. 4b,c) and rescued cytoplasmic export of 18S rRNA (Fig. 4b,e), indicating that both the nucleolar structure and processing are largely rescued. As a control, 28S rRNA expressed from these plasmids was successfully exported to the cytoplasm in all conditions (Fig. 4b and Extended Data Fig. 9e). Notably, inverted synthetic nucleoli are no longer associated with peripheral heterochromatin (Extended Data Fig. 10a), which is also reproduced in endogenous nucleoli after U3 KD (Extended Data Fig. 10b). This suggests that FC and DFC localization at the edge of the nucleolus impairs heterochromatin tethering, consistent with studies suggesting that nucleolar heterochromatin association occurs through the GC[46–48].

As loss of U3 snoRNA function inverted the nucleolar phases (FC– DFC–GC becomes GC–DFC–FC; Fig. 2e), we next used the SSU-only plasmid, which generates synthetic nucleoli lacking a GC (Fig. 3f), to dissect the role of rRNA processing in the reorganization of the FC and DFC subphases (Fig. 4f). While the wild-type SSU-only plasmid produced the classical arrangement of an FC embedded inside a ring-like DFC, a mutant SSU-only plasmid deficient in U3 base-pairing instead resulted in an FC on the surface of the DFC (Fig. 4f). This mirrors the peripheral FC localization observed in synthetic nucleoli produced from rDNA plasmids lacking U3 binding (Extended Data Fig. 9b). These results demonstrate that base-pairing between U3 snoRNA and the 5′ ETS, which is essential for SSU-mediated processing, is required for the ordering of the FC and DFC phases, even in the absence of a GC.

Pre-rRNA processing gates rRNA outflux

Given that pre-rRNA processing is tightly coupled with its movement through the nucleolus (Fig. 2), we next used synthetic nucleoli to study whether impaired U3 processing alters the outflux of 18S pre-rRNA from the DFC. In contrast to wild-type synthetic nucleoli, in which 18S rRNA precursors are localized throughout the nucleolus, U3-binding mutant 18S precursors remain localized in the DFC, and do not move into the GC (Fig. 4b,d; see the schematics of RNA distribution in grey). Compensatory mutations in U3 snoRNA restore RNA flux into the GC (Fig. 4b,d,e), indicating that U3-mediated processing is required for 18S pre-rRNA outflux.

We next used the SSU-only plasmid system (Fig. 4f), which provides a unique opportunity to study the outflux of SSU precursors without the complicating presence of the GC. 18S rRNA precursors and factors demarcating various SSU-processing stages are radially organized around the DFC (Fig. 4g and Extended Data Fig. 10c,d). Early processing factors (NOP56, FBL, KRI1 and KRR1) localized closest within the DFC. 18S pre-rRNA and ribosomal proteins RPS4X and RPS6 extend beyond the DFC, consistent with ribosomal proteins remaining part of maturing ribosomal particles as they are exported. Further out, the RNA exosome component EXOSC10 is localized around the periphery of the DFC. This positioning of the RNA exosome, marking the degradation of 5′ ETS and release of DFC assembly factors[44], further underscores that processing and removal of dozens of assembly factors could enable SSU precursors to be released from the DFC.

To test whether processing directly enables outflux from the DFC, we used the mutant SSU-only plasmids defective in U3-mediated processing and found that 18S precursors, ribosomal protein RPS6 and the late processing factor EXOSC10 are no longer localized at the DFC periphery (Fig. 4h and Extended Data Fig. 10e,f), indicating that successful SSU processing is required for outflux. Indeed, mutant SSU-only nucleoli show accumulation of 18S pre-rRNA and early processing factors (ESF1, NAT10, NOP56 and FBL) within enlarged DFCs (Extended Data Fig. 10g–i), consistent with the retention of unprocessed intermediates in the DFC phase. This lack of outflux of mutant 18S rRNA is also correlated with loss of cytoplasmic 18S rRNA export (Fig. 4i). Together, in both mutant SSU-only and mutant rDNA nucleoli, 18S rRNA precursors appear trapped within the DFC phase and do not flux outward into the GC or nucleoplasm (Fig. 4b,d,h–i). These results suggest that the DFC phase, composed of multivalent interactions between early processing factors and pre-rRNA, can serve as a checkpoint to prevent the outflux of unprocessed SSU intermediates.

Modelling RNA-dependent nucleolar form and function

Our findings indicate that irreversible steps in pre-rRNA processing like rRNA cleavage directly shape the morphology of the nucleolus. Specifically, we hypothesize that rRNA processing modulates the biophysical properties of its liquid-like phases. As a multiphase condensate, the organization of the nucleolar layers is thought to be governed by interfacial tensions ($\gamma_{i,j}$) between phases (i,j), which depend on local concentrations of rRNA species and associated proteins[13,55–57] (Fig. 5a). To examine this physical picture, we adapted a phase-field model from material science using a Flory–Huggins framework[1,7,58,59]. The model comprises three phases—DFC, GC and nucleoplasm (for simplicity, FC and DFC were modelled as a single component, DFC)—and pre-rRNA. Pre-rRNA production, processing, degradation and flux were incorporated based on the kinetic model presented earlier (Methods and Supplementary Notes 1 and 2). A three-body interaction term between rRNA and two of the nucleolar components was essential to capture the effect of rRNA on interfacial tensions[60].

This minimal model recapitulates the inversion morphology observed after inhibition of 5′ ETS cleavage, which results in a significant increase in unprocessed species in the DFC and a lack of mature 18S rRNA in the GC (Fig. 5a–c and Supplementary Note 2). This altered rRNA composition in each phase changes their interfacial tensions, resulting in a relocalization and inversion of the GC and DFC phases (Fig. 5c and Supplementary Video 3). Moreover, our model can also explain two other marked nucleolar morphologies: classical nucleolar caps in response to reduced concentrations of all rRNA intermediates, mimicking Pol I inhibition, or the SSU-only phenotype lacking a GC observed after selective reduction of LSU intermediates (Fig. 5b,d and Supplementary Video 4). While this model is a major simplification of the full complexity of pre-rRNA processing, it nonetheless clearly demonstrates how changes in rRNA processing can reshape nucleolar morphology by altering interfacial tensions (Fig. 5).

Discussion

The nucleolus has been known for almost two centuries, but the precise origin of its multiphase architecture and its relationship to the critical function of ribosome biogenesis has been veiled by a lack of tools to probe this structure–function relationship. Here we have developed and used a set of tools to map and dissect nucleolar organization and function, identifying the essential components required to generate and topologically program the nucleolus. By combining spatiotemporal mapping of pre-rRNA processing, engineering synthetic nucleoli in human cells and mathematical modelling of the determinants of multiphase nucleolar architecture, we bridge the gap between molecular-scale functions of the nucleolus and its structure at the

micrometre scale. Indeed, the approaches developed here provide single-nucleotide resolution of cleavage and modification rates and allow for the parallel measurement of processing in space and time, revealing how the sequential maturation of rRNA is required for its outward flux. The ability to precisely engineer a synthetic nucleolus based on nucleotide-level changes within a recombinant rDNA locus highlights that both rRNA transcription and accurate ribosome assembly blueprint the architecture of the multiphase nucleolus.

A key finding is that, although nucleolar rRNA is generated by the transcription of a single 13.3 kb pre-rRNA transcript, its cleavage, chemical modifications and overall maturation results in SSU and LSU precursors that differentially contribute to the nucleolar structure: SSU processing controls the order of the phases, whereas the LSU is required for GC formation. Moreover, faithful pre-rRNA processing is required for the flux of pre-ribosomal particles through the successive phases. Specifically, pre-ribosomal particles that cannot undergo key maturation events remain trapped within the DFC phase, suggesting that the nucleolar phases could ensure the fidelity of ribosome assembly by preventing the release of immature precursors into the next compartment. Our study therefore underscores the role of nucleolar multiphase organization in functional staging, whereby the physical separation of nucleolar phases may serve as distinct processing or 'retention' compartments segregating the different reactions driving the sequential maturation of SSU and LSU particles.

Together, we used a set of tools to identify how pre-rRNAs build and arrange the nucleolar phases that facilitate their processing, revealing how defects in ribosome assembly can manifest in substantial changes in the topology of the nucleolus. Our work therefore not only underscores basic principles of how RNA and its processing gives rise to the multiphase architecture of the nucleolus, but also provides a foundational toolkit for dissecting how ribosome biogenesis and nucleolar morphology are dysregulated in disease.

Online content

Any methods, additional references, Nature Portfolio reporting summaries, source data, extended data, supplementary information, acknowledgements, peer review information; details of author contributions and competing interests; and statements of data and code availability are available at https://doi.org/10.1038/s41586-025-09207-4.

1. Shin, Y. & Brangwynne, C. P. Liquid phase condensation in cell physiology and disease. *Science* **357**, eaaf4382 (2017).
2. Banani, S. F., Lee, H. O., Hyman, A. A. & Rosen, M. K. Biomolecular condensates: organizers of cellular biochemistry. *Nat. Rev. Mol. Cell Biol.* **18**, 285–298 (2017).
3. Henras, A. K., Plisson-Chastang, C., O'Donohue, M.-F., Chakraborty, A. & Gleizes, P.-E. An overview of pre-ribosomal RNA processing in eukaryotes. *Wiley Interdiscip. Rev. RNA* **6**, 225–242 (2015).
4. Vanden Broeck, A. & Klinge, S. Eukaryotic ribosome assembly. *Annu. Rev. Biochem.* **93**, 189–210 (2024).
5. Klinge, S. & Woolford, J. L. Jr. Ribosome assembly coming into focus. *Nat. Rev. Mol. Cell Biol.* **20**, 116–131 (2019).
6. Alberti, S., Gladfelter, A. & Mittag, T. Considerations and challenges in studying liquid-liquid phase separation and biomolecular condensates. *Cell* **176**, 419–434 (2019).
7. Brangwynne, C. P., Tompa, P. & Pappu, R. V. Polymer physics of intracellular phase transitions. *Nat. Phys.* **11**, 899–904 (2015).
8. Pappu, R. V., Cohen, S. R., Dar, F., Farag, M. & Kar, M. Phase transitions of associative biomacromolecules. *Chem. Rev.* **123**, 8945–8987 (2023).
9. Rangadurai, A. K. et al. Phase separation modulates the thermodynamics and kinetics of RNA hybridization. *J. Am. Chem. Soc.* **146**, 19686–19689 (2024).
10. Nott, T. J., Craggs, T. D. & Baldwin, A. J. Membraneless organelles can melt nucleic acid duplexes and act as biomolecular filters. *Nat. Chem.* **8**, 569–575 (2016).
11. Boisvert, F.-M., van Koningsbruggen, S., Navascués, J. & Lamond, A. I. The multifunctional nucleolus. *Nat. Rev. Mol. Cell Biol.* **8**, 574–585 (2007).
12. Lafontaine, D. L. J., Riback, J. A., Bascetin, R. & Brangwynne, C. P. The nucleolus as a multiphase liquid condensate. *Nat. Rev. Mol. Cell Biol.* **22**, 165–182 (2021).
13. Feric, M. et al. Coexisting liquid phases underlie nucleolar subcompartments. *Cell* **165**, 1686–1697 (2016).
14. Mullineux, S.-T. & Lafontaine, D. L. J. Mapping the cleavage sites on mammalian pre-rRNAs: where do we stand? *Biochimie* **94**, 1521–1532 (2012).
15. Thiry, M., Cheutin, T., O'Donohue, M. F., Kaplan, H. & Ploton, D. Dynamics and three-dimensional localization of ribosomal RNA within the nucleolus. *RNA* **6**, 1750–1761 (2000).

Article

16. Potapova, T. A. et al. Distinct states of nucleolar stress induced by anticancer drugs. *eLife* **12**, RP88799 (2023).
17. Burger, K. et al. Chemotherapeutic drugs inhibit ribosome biogenesis at various levels. *J. Biol. Chem.* **285**, 12416–12425 (2010).
18. Nicolas, E. et al. Involvement of human ribosomal proteins in nucleolar structure and p53-dependent nucleolar stress. *Nat. Commun.* **7**, 11390 (2016).
19. Bryant, C. J., McCool, M. A., Abriola, L., Surovtseva, Y. V. & Baserga, S. J. A high-throughput assay for directly monitoring nucleolar rRNA biogenesis. *Open Biol.* **12**, 210305 (2022).
20. Reynolds, R. C., Montgomery, P. O. & Hughes, B. Nucleolar 'caps' produced by actinomycin D. *Cancer Res.* **24**, 1269–1277 (1964).
21. Schoefl, G. I. The effect of actinomycin D on the fine structure of the nucleolus. *J. Ultrastruct. Res.* **10**, 224–243 (1964).
22. Shav-Tal, Y. et al. Dynamic sorting of nuclear components into distinct nucleolar caps during transcriptional inhibition. *Mol. Biol. Cell* **16**, 2395–2413 (2005).
23. Scherrer, K., Latham, H. & Darnell, J. E. Demonstration of an unstable RNA and of a precursor to ribosomal RNA in HeLa cells. *Proc. Natl Acad. Sci. USA* **49**, 240–248 (1963).
24. Alwine, J. C., Kemp, D. J. & Stark, G. R. Method for detection of specific RNAs in agarose gels by transfer to diazobenzyloxymethyl-paper and hybridization with DNA probes. *Proc. Natl Acad. Sci. USA* **74**, 5350–5354 (1977).
25. Yao, R.-W. et al. Nascent pre-rRNA sorting via phase separation drives the assembly of dense fibrillar components in the human nucleolus. *Mol. Cell* **76**, 767–783 (2019).
26. Shan, L. et al. Nucleolar URB1 ensures 3′ ETS rRNA removal to prevent exosome surveillance. *Nature* **615**, 526–534 (2023).
27. Mangan, H. & McStay, B. Human nucleoli comprise multiple constrained territories, tethered to individual chromosomes. *Genes Dev.* **35**, 483–488 (2021).
28. Fu, Y. et al. Real-time imaging of RNA polymerase I activity in living human cells. *J. Cell Biol.* **222**, e202202110 (2023).
29. Kopp, K. et al. Pol I transcription and pre-rRNA processing are coordinated in a transcription-dependent manner in mammalian cells. *Mol. Biol. Cell* **18**, 394–403 (2007).
30. King, M. R. et al. Macromolecular condensation organizes nucleolar sub-phases to set up a pH gradient. *Cell* **187**, 1889–1906 (2024).
31. Mitrea, D. M. et al. Nucleophosmin integrates within the nucleolus via multi-modal interactions with proteins displaying R-rich linear motifs and rRNA. *eLife* **5**, e13571 (2016).
32. Bhat, P. et al. Genome organization around nuclear speckles drives mRNA splicing efficiency. *Nature* **629**, 1165–1173 (2024).
33. Riback, J. A. et al. Viscoelasticity and advective flow of RNA underlies nucleolar form and function. *Mol. Cell* **83**, 3095–3107 (2023).
34. Marchand, V., Blanloeil-Oillo, F., Helm, M. & Motorin, Y. Illumina-based RiboMethSeq approach for mapping of 2′-O-Me residues in RNA. *Nucleic Acids Res.* **44**, e135 (2016).
35. Aubert, M., O'Donohue, M.-F., Lebaron, S. & Gleizes, P.-E. Pre-ribosomal RNA processing in human cells: from mechanisms to congenital diseases. *Biomolecules* **8**, 123 (2018).
36. Kos, M. & Tollervey, D. Yeast pre-rRNA processing and modification occur cotranscriptionally. *Mol. Cell* **37**, 809–820 (2010).
37. Trapman, J. & Planta, R. J. Maturation of ribosomes in yeast. I Kinetic analysis by labelling of high molecular weight rRNA species. *Biochim. Biophys. Acta* **442**, 265–274 (1976).
38. Kishi, J. Y. et al. SABER amplifies FISH: enhanced multiplexed imaging of RNA and DNA in cells and tissues. *Nat. Methods* **16**, 533–544 (2019).
39. Yasuhara, T. et al. Condensates induced by transcription inhibition localize active chromatin to nucleoli. *Mol. Cell* **82**, 2738–2753 (2022).
40. Langhendries, J.-L., Nicolas, E., Doumont, G., Goldman, S. & Lafontaine, D. L. J. The human box C/D snoRNAs U3 and U8 are required for pre-rRNA processing and tumorigenesis. *Oncotarget* **7**, 59519–59534 (2016).
41. Dragon, F. et al. A large nucleolar U3 ribonucleoprotein required for 18S ribosomal RNA biogenesis. *Nature* **417**, 967–970 (2002).
42. Sharma, S., Marchand, V., Motorin, Y. & Lafontaine, D. L. J. Identification of sites of 2′-O-methylation vulnerability in human ribosomal RNAs by systematic mapping. *Sci. Rep.* **7**, 11490 (2017).
43. Sharma, S. & Lafontaine, D. L. J. 'View from a bridge': a new perspective on eukaryotic rRNA base modification. *Trends Biochem. Sci.* **40**, 560–575 (2015).
44. Singh, S., Vanden Broeck, A., Miller, L., Chaker-Margot, M. & Klinge, S. Nucleolar maturation of the human small subunit processome. *Science* **373**, eabj5338 (2021).
45. Vanden Broeck, A. & Klinge, S. Principles of human pre-60S biogenesis. *Science* **381**, eadh3892 (2023).
46. Gupta, S. et al. The nucleolar granular component mediates genome-nucleolus interactions and establishes their repressive chromatin states. *Mol. Cell* **85**, 2165–2175.e6 (2025).
47. Rajshekar, S. et al. Affinity hierarchies and amphiphilic proteins underlie the co-assembly of nucleolar and heterochromatin condensates. Preprint at *bioRxiv* https://doi.org/10.1101/2023.07.06.547894 (2024).
48. Holmberg Olausson, K., Nistér, M. & Lindström, M. S. Loss of nucleolar histone chaperone NPM1 triggers rearrangement of heterochromatin and synergizes with a deficiency in DNA methyltransferase DNMT3A to drive ribosomal DNA transcription. *J. Biol. Chem.* **289**, 34601–34619 (2014).
49. Wandrey, F. et al. The NF45/NF90 heterodimer contributes to the biogenesis of 60S ribosomal subunits and influences nucleolar morphology. *Mol. Cell. Biol.* **35**, 3491–3503 (2015).
50. Németh, A. & Grummt, I. Dynamic regulation of nucleolar architecture. *Curr. Opin. Cell Biol.* **52**, 105–111 (2018).
51. Beltrame, M. & Tollervey, D. Base pairing between U3 and the pre-ribosomal RNA is required for 18S rRNA synthesis. *EMBO J.* **14**, 4350–4356 (1995).
52. Dutca, L. M., Gallagher, J. E. G. & Baserga, S. J. The initial U3 snoRNA:pre-rRNA base pairing interaction required for pre-18S rRNA folding revealed by in vivo chemical probing. *Nucleic Acids Res.* **39**, 5164–5180 (2011).
53. Marmier-Gourrier, N., Cléry, A., Schlotter, F., Senty-Ségault, V. & Branlant, C. A second base pair interaction between U3 small nucleolar RNA and the 5′-ETS region is required for early cleavage of the yeast pre-ribosomal RNA. *Nucleic Acids Res.* **39**, 9731–9745 (2011).
54. Dörner, K., Ruggeri, C., Zemp, I. & Kutay, U. Ribosome biogenesis factors-from names to functions. *EMBO J.* **42**, e112699 (2023).
55. Kaur, T. et al. Sequence-encoded and composition-dependent protein-RNA interactions control multiphasic condensate morphologies. *Nat. Commun.* **12**, 872 (2021).
56. Fisher, R. S. & Elbaum-Garfinkle, S. Tunable multiphase dynamics of arginine and lysine liquid condensates. *Nat. Commun.* **11**, 4628 (2020).
57. Sanders, D. W. et al. Competing protein-RNA interaction networks control multiphase intracellular organization. *Cell* **181**, 306–324 (2020).
58. Berry, J., Weber, S. C., Vaidya, N., Haataja, M. & Brangwynne, C. P. RNA transcription modulates phase transition-driven nuclear body assembly. *Proc. Natl Acad. Sci. USA* **112**, E5237–E5245 (2015).
59. Flory, P. J. Thermodynamics of high polymer solutions. *J. Chem. Phys.* **9**, 660–660 (1941).
60. Martin, E. W. et al. Valence and patterning of aromatic residues determine the phase behavior of prion-like domains. *Science* **367**, 694–699 (2020).

Methods

Statistics and reproducibility

All statistical tests were performed using GraphPad Prism 10, using either two-tailed Mann–Whitney U-tests or two-tailed t-tests, as specified in the legends. Tests for normality were performed when appropriate. Sample sizes were not predetermined. For all experiments, cells were randomized such that within a biological or technical replicate all cells were analysed equally with no sub-sampling. Microscopy imaging, western blotting and quantitative PCR with reverse transcription (RT–qPCR) were repeated independently at least three times with similar results. P values and the numbers of observations (n) are provided in the figure legends.

Cell culture and cell lines used in this study

All cells were cultured in a humidified chamber at 37 °C with 5% CO_2 and 1% streptomycin and penicillin (Gibco, 15140122). HEK293T cells (ATCC), HEK293T cells tagged with UBTF–sfGFP, NPM1–mtagRFP and FBL–Halotag (gift from the Leonetti laboratory), HCT116 cells (gift from Y. Kang) and MCF7 cells (gift from Y. Kang) were cultured in DMEM (GIBCO, 11995065) supplied with 10% FBS (R&D Systems, S11150H). MCF10A (gift from Y. Kang) cells were cultured in DMEM/F12 medium (Thermo Fisher Scientific, 11320082) supplied with 5% horse serum (Sigma-Aldrich, H1138), 20 ng ml^{-1} EGF (Novoprotein, C029), 10 ng ml^{-1} insulin (Sigma-Aldrich, 91077 C) and 1 µg ml^{-1} hydrocortisone (Sigma-Aldrich, H0888). All cells were checked for *Mycoplasma* and authenticated. For imaging, cells were treated with trypsin (trypsin-EDTA 0.05%, Thermo Fisher Scientific, 25300054) for dissociation and then seeded into 96-well glass-bottom dishes (Cellvis, P96-1.5H-N) coated with bovine fibronectin (Sigma-Aldrich, F1141) diluted 1:4 in 1× DPBS (Thermo Fisher Scientific, 14190144). All rDNA plasmid transfection experiments were performed in HEK293T cells, and all other experiments were performed in MCF10A cells unless otherwise noted.

Recombinant human rDNA plasmid designs

A plasmid containing a previously described minimized 5′ ETS (mini 5′ ETS) that is compatible with human SSU biogenesis was used as a starting point (pSK_M323) for the design of plasmids described in this Article[44] (Extended Data Fig. 7a). The structure of the human SSU processome in state pre-A1 (Protein Data Bank: 7MQ8) was used to redesign the 3′ and 5′ hinge RNA duplexes between U3 snoRNA and the 5′ ETS (Extended Data Fig. 7c,d). Nucleotide substitutions were introduced that maintain the overall nucleotide composition of the duplexes while only allowing matching variants to base pair (Extended Data Fig. 7e,f). Variants of 3′ and 5′ hinges of the 5′ ETS and U3 snoRNA were combined (pSK_M432-pSK_M435) by including variants of the complete human U3 gene upstream of the RNA polymerase I promoter, resulting in a bidirectional promoter for pre-rRNA (RNA polymerase I) and U3 snoRNA (RNA polymerase II) (Extended Data Fig. 7g). Plasmids coding for either wild-type or mutant SSU pre-rRNAs were generated by terminating transcripts after the first 48 nucleotides of the 5.8S gene and a plasmid coding for the LSU pre-rRNAs contained the first 53 nucleotides of the mini 5′ ETS followed by ITS1, 5.8S, ITS2, 28S and the 3′ ETS (Extended Data Fig. 7b). A probe for ITS2 was introduced from a previously published plasmid (pSK_M349) that was shown to give rise to mature human LSUs[45].

Plasmid construction

FM5-Nop56-mcherry was a gift from D. W. Sanders. FM5-mTagBFP2-NPM1, FM5-RPA16-GFP and FM5-RPS6-Halotag lentiviral DNA plasmids were generated using the FM5 lentiviral vector (gift from D. W. Sanders)[57]. A DNA fragment encoding human RPS6 was amplified from original plasmids (DNASU Plasmid Repository, HsCD00043827) by PCR using the Q5 High-Fidelity 2X Master Mix (NEB) with oligonucleotides synthesized by IDT. gBlocks encoding RPA16 or RPS4X proteins were ordered from IDT. DNA fragments containing *NPM1* and *RPA16* were PCR amplified from gifted plasmids from J. A. Riback. The In-Fusion HD cloning kit (Takara) was used to insert the fragments into the desired linearized vector featuring a GS-linker–fluorescent tag fusion. All of the constructs were confirmed by Sanger sequencing (GENEWIZ).

IF analysis

Cells were fixed in 96 well glass bottom plates with 4% PFA for 10 min, washed with 1× PBS twice and then permeabilized with 1× PBST (with 0.5% Triton X-100) for 15 min. The samples were then blocked in 2% BSA in PBS for 30 min and then incubated with primary antibodies in 2% RNase-free BSA (VWR, 97061-420) for 2 h at 37 °C (a detailed antibody list is provided in Supplementary Table 1). Three 1× PBS washes were conducted for 5 min each. For non-conjugated antibodies, anti-mouse or anti-rabbit secondary antibodies with the desired fluorophores were used at a 1:1,000 dilution for 2 h at 37 °C. Three 1× PBS washes were conducted with 5 min each before imaging.

RNA-FISH

SABER FISH was performed as previously described[38,61]. Probes were designed across the ribosomal RNA sequence and additional hairpin sequences are appended at the 3′ end of the probe for primer exchange reaction concatemerization with hairpin_28 (paired with 488 fluorescent oligos for imaging) or hairpin_25 (paired with 647 fluorescent oligos for imaging). A list of all of the probe sequences is provided in Supplementary Table 1. Note that, because early cleavage sites are cleaved and degraded rapidly, we used FISH probes tiling 5′ ETS (upstream of 01 site) and 3′ ETS (downstream of 02 site) to improve detection. For probing ribosomal RNAs transcribed from synthetic plasmids, 18S* and 28S* probes were designed (Supplementary Table 1) to probe the unique (around 16–20 nucleotides) insertion within the 18S and 28S sequence from plasmids[44]. Moreover, an antisense 18S* probe was designed to ensure the RNA-FISH signal specifically comes from RNA instead of DNA (Extended Data Fig. 8c and Supplementary Table 1). To specifically probe endogenous ribosomal RNA, we used probes hybridized to parts of the 5′ ETS region that are excluded from the synthetic rDNA plasmids (Δ1,2,3)[44]. Moreover, as a unique sequence is inserted within 28S (28S*), we designed a FISH probe flanking the insertion, located upstream and downstream of 28S*, for selective hybridization to endogenous 28S rRNA (endogenous 28S in Supplementary Table 1). For analysing whether plasmid-derived RNAs are exported to the cytoplasm, we used the endogenous 28S probe for segmenting the nuclei and cytoplasm (details are provided in the the 'Quantitative image analysis' section). IF analysis was conducted after completing all of the FISH steps, starting from the blocking step as described in the 'IF analysis' section. Murine RNase inhibitors (NEB, M0314L) were used at a 1:200 dilution in all of the steps of IF to preserve the RNA-FISH signals.

Microscopy

A Nikon CSU-W1 SoRa spinning-disc confocal microscope equipped with a Yokogawa SoRa pixel reassignment-based super-resolution device was used for rapid super-resolution imaging. The system was built around the Nikon Ti2-E fully motorized microscope and is equipped with dual Hamamatsu Fusion BT sCMOS cameras. The W1 Sora system is equipped with 405, 488, 514, 532, 561, 594 and 640 nm laser lines. For this work, a Nikon CFI Plan Apo Lambda D ×60 oil (MRD71670) lens was used with a ×2.8 SoRa magnification and 405, 488, 561 and 640 nm lasers. A Mad City Labs piezo z stage was used for z-stack acquisition. All acquisitions were performed using the Fusion BT in Ultra Quiet readout using correlated double sampling. In some cases, Denoise.ai (Nikon software) was used for images shown and analysed in this study.

Article

Lentiviral packaging and transduction

Lentiviruses were made using HEK293T cells seeded in a six-well plate at 70–80% confluence. The desired plasmids were transfected together with helper plasmids VSVG and PSP using Lipofectamine 3000 (Invitrogen, L3000008) according to previously described protocols[57,62]. Viruses were collected 48 h after transfection and filtered through syringe filters with a 0.45-µm pore size (VWR). Lentiviral transduction was conducted in 96-well plates at 30% cell confluency for 2 days and cells were then expanded to make stable expression lines and sorted using fluorescence-activated cell sorting for polyclonal lines, with a tight window for each fluorescent protein intensity.

Transient transfection

rDNA plasmids (including engineered mutant plasmids) were transfected into HEK293T cells (for one well of a 24-well plate, 600 ng plasmids were transfected into 150,000 HEK293T cells) using lipofectamine 3000 (Invitrogen). Unless otherwise stated, for all plasmid transfection experiments, cells were seeded into 96-well glass-bottom plates 24 h after transfection and fixed for SABER FISH 48 h after transfection. Specifically, all cytoplasmic export analyses were performed at 48 h after transfection (Figs. 3f–h and 4e,i and Extended Data Fig. 9e). This ensured that all plasmids were compared at the same time after transfection. For the wild-type and mutant SSU-only plasmid transfection experiments comparing nucleolar morphology and radial outflux in Fig. 4f–h and Extended Data Fig. 10c–h, we optimized the timing of transfection to be 24 h to achieve the optimal number of de novo SSU nucleoli.

Endogenous N-terminal tagging of NPM1 with mTagBFP2 using CRISPR–Cas9

Endogenous N-terminal tagging of NPM1 in MCF10A cells was performed as previously described[63,64]. An oligonucleotide pair encoding an NPM1-targeting gRNA (TGTCCATCGAATCTTCCAT) was cloned into a modified lentiCRISPRv2-puro plasmid (from A. Lin) through the BsmBI restriction site. MCF10A cells were transfected using the FuGENE HD transfection reagent (Promega, E2311) with plasmids containing the cloned gRNA and a donor plasmid. The donor plasmid was constructed by cloning the tag with a flexible linker flanked by 300 bp homology arms complementary to the N terminus of the NPM1 gene into the pUC19 vector (Thermo Fisher Scientific, SD0061). Then, 3 days after transfection, mTagBFP2-positive cells were single-cell sorted into 96-well plates. These single-cell clones were then cultured and expanded for tagging validation through western blotting and junction PCR of the specific genomic locus (Extended Data Fig. 2f,g) and imaging to confirm correct subcellular localization.

All ribosomal RNA processing perturbations used in this study

CX-5461 Pol I inhibition. Cells were treated with 10 µM final CX-5461 (MedChem Express, HY-13323) for 90 min before fixation and imaging. DMSO was used for the control group.

FVP broad rRNA processing inhibition. Cells were treated with FVP at a final concentration of 2 µM (MedChem Express; HY-10005). As a control, cells were treated with DMSO. For the 5eU imaging and 5eU–seq, cells were pretreated for 1 h to broadly inhibit processing prior to a 15 min pulse and subsequent 0–90 min chase. All pulse–chase medium contained 2 µM FVP to ensure that processing inhibition was maintained throughout the 5eU pulse–chase labelling. For imaging the reformation of the multiphase nucleolus after FVP washout, cells were treated with 2 µM FVP for 2 h and then washed twice quickly with 1× DPBS before imaging in regular medium. Videos were taken at 37 °C with 5% CO_2, every 2 min after FVP removal for 90 min. For 5eU imaging after FVP washout, cells were treated with 2 µM FVP for 2 h and then washed twice quickly with 1× DPBS before a 15 min 5eU pulse followed by a 0–90 min chase.

RPL5 shRNA. For shRNA vector cloning into a lentiviral plasmid for expressing shRNAs with puromycin selection, RPL5 shRNA (GATGA TAGTTCGTGTGACAAA) sequences and a negative control (GCTCT TAACTAACGTCACCTA) sequence were separately cloned into pLKO.1 TRC vector after digestion with AgeI and EcoRI. Lentiviruses were produced as described above and added to cells for 5eU–seq and imaging experiments with MCF10A cells at 30% confluency. After 1 day, virus-containing medium was removed and replaced with fresh medium including 5 µg ml⁻¹ of puromycin. After selection for another 3–4 days, cells in the negative control well that were not treated with virus were dying as expected, indicating that selection was effective. Selection was terminated by replacing the puromycin medium with normal MCF10A medium. Cells were then split for 5eU sequencing, imaging or RNA extraction followed by RT–qPCR (a list of the primer sequences used is provided in Supplementary Table 1) 4–5 days after adding shRNA viruses.

U3/U8 snoRNA ASO. U3 and U8 snoRNA ASO treatment was performed as previously described[40] with several adaptations. For 5eU–seq experiments, in each well of a 6-well plate, 1.5 µl of 40 µM (stock) ASO diluted in 125 µl Opti-MEM (Thermo Fisher Scientific, 31985062) was combined with 7.5 µl Lipofectamine RNAiMAX (Thermo Fisher Scientific, 13778075) diluted in 125 µl Opti-MEM. After a 30 min incubation at room temperature, 1.75 ml of a suspension containing 250,000 cells in antibiotic-free medium (see the 'Cell culture and cell lines used in this study' section) was added to each well. Cells were incubated for 1.5 days before analysis using 5eU–seq (Fig. 2b,d and Extended Data Fig. 3h,i,n,o). For imaging experiments, in each well of a 96-well plate coated with bovine fibronectin (Sigma-Aldrich, F1141) diluted 1:4 in 1× DPBS (Thermo Fisher Scientific, 14190144), 0.05 µl of 40 µM ASO diluted in 4.165 µl Opti-MEM was combined with 4.165 µl Lipofectamine RNAiMAX diluted in 0.25 µl Opti-MEM. After a 30 min incubation at room temperature, 100 µl of a suspension containing 8,000 cells in antibiotic-free medium was added to each well. For 5eU-imaging experiments, cells were incubated for 2.5 days before fixation (Fig. 2c and Extended Data Fig. 6e). For experiments monitoring the inversion morphology, cells were treated again with ASO after 2.5 days according to the protocol described above, then incubated for an additional 2 days before fixation (Fig. 2e,f). We also tested the morphology change at shorter times (at 8, 12, 24 and 48 h), and observed that FCs and DFCs start moving towards the edge of the nucleolus within 8–12 h, with the phenotype fully developing within 24–48 h (Extended Data Fig. 5h–j). All incubations were performed at 37 °C and 5% CO_2. ASO sequences were published in a previous paper[40] and are listed in Supplementary Table 1.

FBL siRNA. FBL siRNA treatment was performed as described in the U3 and U8 snoRNA ASO treatment protocol with the following modifications. For 5eU–seq experiments and western blotting, 2 µl of 20 µM FBL siRNA (Supplementary Table 1) or control siRNA (Thermo Fisher Scientific, 4390843) diluted in 250 µl Opti-MEM was combined with 6 µl Lipofectamine RNAiMAX diluted in 250 µl Opti-MEM. For imaging experiments, 0.066 µl of 20 µM FBL siRNA or control siRNA diluted in 8.33 µl Opti-MEM was combined with 8.33 µl Lipofectamine RNAiMAX diluted in 0.2 µl Opti-MEM. For all of the experiments, cells were treated again after 24 h with FBL siRNA or control siRNA. Cells were incubated for an additional 3 days before performing 5eU–seq, collection for western blotting or fixation for 5eU imaging.

Total RNA isolation

For each well of a six-well plate, total RNA was collected in 200 µl 1× Buffer RLT (QIAGEN, 79216) and isolated using the QIAGEN RNeasy Mini Kit (74104), followed by 1 h of DNase treatment using TURBO DNase (Thermo Fisher Scientific, AM2238). DNase-digested RNA was then further purified using the Zymo RNA Clean and Concentrator-25 kit (R1017).

RNA electrophoresis

The RNA integrity after isolation was analysed and the ratios of 28S to 18S rRNA in U3 and U8 snoRNA ASO- and SCR ASO-treated samples were assayed using the Agilent RNA High Sensitivity Assay (Agilent, 5067-5579) on the 4150 TapeStation system (Agilent Technologies) according to the manufacturer's instructions.

RT–qPCR for validation of perturbation

U3 snoRNA, U8 snoRNA and *RPL5* mRNA KD efficiency were assayed using RT–qPCR using the Luna Universal One-Step RT-qPCR Kit (NEB, E3005) according to the manufacturer's instructions, except that each reaction was scaled to 60 µl to allow for four technical replicates (12.5 µl) per sample. U6 snoRNA served as the loading control. RT–qPCR was performed on the Applied Biosystems QuantStudio 3 Real-Time PCR System instrument (A28567). Primer sequences used are listed in Supplementary Table 1. All primers were synthesized by Integrated DNA Technologies (IDT). U3, U8 and U6 snoRNA absolute amounts were determined using standard curves prepared for each primer set. U3 and U8 KD efficiency was assayed by comparing the absolute amounts of U3 or U8 snoRNA normalized to the absolute amounts of U6 snoRNA, in U3 or U8 snoRNA ASO- versus SCR ASO-treated samples.

Polysome fractionation and analysis

HEK293T cells after 48 h of transfection with the wild-type rDNA plasmid, SSU-only rDNA plasmid or no transfection control were treated with 100 µg ml^{-1} cycloheximide (CHX) for 10 min at 37 °C with 5% CO_2 and polysome fractionation was performed as described previously with minor modifications[65]. Cells were then lysed in 400 µl polysome lysis buffer (25 mM HEPES, pH 7.3, 150 mM NaCl, 15 mM $MgCl_2$, 1% Triton X-100, 8% glycerol, 0.5% sodium deoxycholate, 100 µg ml^{-1} CHX, 1 mM DTT, RNase inhibitors (NEB, M0314L, 1:60 dilution) and DNase (Thermo Fisher Scientific, AM2239, 1:400)) by incubating on ice for 15 min, followed by two consecutive centrifugations at 800g for 5 min, one centrifugation at 8,000g for 5 min and one centrifugation at 20,000g for 5 min (all at 4 °C) to remove nuclei and mitochondria. A 50 µl portion of the resulting supernatant was set aside as the input, while the remainder was loaded onto a 10–50% (w/v) sucrose gradient prepared in polysome gradient buffer (25 mM HEPES, pH 7.3, 150 mM NaCl, 15 mM $MgCl_2$, 100 µg ml^{-1} CHX and 1 mM DTT). Ultracentrifugation was performed at 40,000 rpm for 2.5 h at 4 °C in a SW41 Ti rotor (Beckman Coulter). After ultracentrifugation, gradients were fractionated using a piston gradient fractionator (Biocomp) with continuous monitoring of absorbance at 254 nm to visualize ribosomal profiles. The fractions corresponding to 'monosomes (80S)' and 'polysomes (>2 ribosomes)' were collected and pooled separately. RNA was extracted from each fraction using ethanol precipitation followed by proteinase K (NEB, P8107S) digestion for 1 h at 50 °C, and cleaned using the Zymo RNA Clean and Concentrator-5 kit (R1016). Then, 25 ng of isolated RNA from input, monosome or polysome fractions was put into the RT–qPCR reaction. RT–qPCR was performed as described in the previous section using primers for 18S* (plasmid rRNA) and 18S (endogenous rRNA) (Supplementary Table 1). For each fraction (monosome or polysome), we calculated the incorporation of plasmid-derived rRNA across all ribosomes by normalizing the plasmid rRNA (18S*) abundance to the total rRNA (18S) abundance. Standard curves were generated to normalize for primer efficiencies.

5eU imaging

The 5eU imaging protocol was modified from previous studies[33]. In brief, cells were seeded 1 day before at 40% confluency in 96-well glass-bottom plates. The volumes of all reagents were kept at 100 µl for each well of the 96-well plate. 5eU (Thermo Fisher Scientific, E10345) solution was prepared at 0.5 mM in cell culture medium and added to cells with medium removed from the well. Cells were then kept in an incubator (37 °C with 5% CO_2) for 15 min (pulse). Next, 5eU

containing medium was removed and quickly washed twice with 1× DPBS containing 10 mM (excess) uridine (Sigma-Aldrich, U6381-5G) to outcompete the leftover 5eU. The culture medium containing 10 mM uridine was then added to the well before incubating for different chase timepoints (0 to 120 min) at 37 °C with 5% CO_2. Note that all solutions mentioned above were kept at 37 °C using a heat block to minimize temperature-induced effects on RNA transcription and processing. For wells with different chase times on the same 96-well plate, the starting time of the 5eU pulse was staggered so that all the chase timepoints ended at the same time. For fixation, 4% paraformaldehyde (PFA) diluted from 16% PFA (Thermo Fisher Scientific, PI28906) with 1× PBS was used for 15 min at room temperature. Fixed cells were then washed twice with 1× PBS and permeabilized with 1× PBST (1× PBS and 0.5% Triton X-100) for 15 min. For click chemistry, the Click-iT Plus Alexa Fluor 647 Picolyl Azide Toolkit (Thermo Fisher Scientific, C10643) was used according to the manufacturer's instructions, with the exception of using AZDye 647 Picolyl Azide (Click Chemistry Tools, CCT-1300-1) instead of the azide from the kit. After 30 min of applying the click chemistry reaction cocktail, cells were washed once with 1× PBS before imaging. For combining IF with 5eU imaging, IF steps were performed as described above before click chemistry.

5eU–seq

All 5eU pulse–chase labelling experiments combined with sequencing were performed in MCF10A cells except for method validation described in Extended Data Fig. 1c–g, which was performed on HEK293T cells. Cells were seeded for 5eU pulse–chase labelling such that their confluency was about 50–60% at the time of collection. Cells were pulse labelled with 5eU (Jena Biosciences, CLK-N002-10) for 15 min at 37 °C with 5% CO_2. Cells were then removed from the incubator and quickly washed twice with 1× DPBS to remove 5eU from the cells. Cells were then chased with medium containing 10 mM uridine (Sigma-Aldrich, U6381) to outcompete the leftover 5eU in cells over different chase timepoints. All solutions were kept at 37 °C using a heat block to minimize temperature-induced changes to the cells, which could impact RNA transcription and processing. After the given chase time, cells were collected in 1× buffer RLT (Qiagen, 79216) and frozen at −80 °C for RNA isolation. RNA isolation was performed using the Qiagen RNeasy Mini kit followed by DNase digestion (TURBO DNase, Invitrogen, AM2238) to remove genomic DNA. RNA concentrations were measured using the Qubit RNA BR (Thermo Fisher Scientific, Q10211) system and the RNA integrity was analysed on the Agilent RNA High Sensitivity (HS) Tapestation.

Total RNA (10–15 µg) isolated after 5eU pulse–chase was click-reacted with biotin picolyl azide (Click Chemistry Tools, 1167-25) as described previously[32] with the following modifications. Capture of biotinylated RNA was performed using 20 µl Dynabeads MyOne Streptavidin C1 beads (Invitrogen, 65002) after click chemistry. Captures and washes were performed as previously described except for a modification to the three 5 min washes of captured material, which was changed to 75 °C in no-salt urea buffer (4 M urea, 10 mM HEPES, pH 7.5, 10 mM EDTA, 0.5% Triton X-100, 0.2% SDS, 0.1% Na-DOC). We found that three rounds of sequential captures (as described previously[32]) as well an optimized protocol introduced here performing washes at high temperature and in a buffer lacking salt were essential to reduce the background of highly abundant mature rRNA (Extended Data Fig. 1a–d). RNA-seq library preparation was performed as previously described[66]. 5eU–seq libraries were then sequenced on the NovaSeq 6000 (Illumina) system with paired-end reads (either 150 × 150 or 100 × 200). The samples that failed quality control, such as failed click reactions, streptavidin captures or library amplifications, were excluded from downstream analyses.

High-performance computing

The analyses presented in this Article were performed on computational resources managed and supported by Princeton Research

Article

Computing, a consortium of groups including the Princeton Institute for Computational Science and Engineering (PICSciE).

Computational analysis of 5eU–seq cleavage and 2′-O-methylation

Sequencing read analysis pipeline. A custom snakemake pipeline was used to perform alignments, 2′-O-methylation analysis and cleavage analysis (https://github.com/SoftLivingMatter/5eU-seq-pipelines). Sequencing reads were trimmed with Trimmomatic (v.0.39)[67] to remove adaptor sequences and bases containing low quality scores. Trimmed reads were then aligned to the rDNA genome (GenBank: U13369.1) using STAR (v.2.7.11a)[68]. Reads were sorted and indexed using Samtools (v.1.9-4)[69] and only uniquely mapped reads were kept for further analysis. The fraction of reads that are cleaved at a given site was calculated as the number of non-spanning reads divided by the total number of reads (spanning and non-spanning) at a given site (Extended Data Fig. 1b) using featureCounts (v.1.6.4)[70] (Subread package). rRNA cleavage sites were annotated based on the positions described previously[14]. All rRNA cleavage sites used in this study were manually inspected to define the sites of cleavage based on where the 5′ or 3′ end of reads piled up, demarcating a precise cleavage site. Specifically, well-defined cleavage sites correspond to those that undergo endonuclease cleavage and can be mapped at a base-pair resolution using 5eU–seq (examples shown in Extended Data Fig. 1b). In cases in which endonucleolytic rRNA cleavage events are followed by gradual degradation, a broader window (several nucleotides) downstream of an annotated site was used (Supplementary Table 1).

Cleavage efficiency measurement. Cleavage efficiency, defined as 1 over the time to reach 50% cleavage (t_{50}), was estimated by fitting the observed 5eU–seq fraction cleaved over time (Extended Data Fig. 3) to a sigmoidal 4PL curve using Prism 10 software. We then computed the normalized cleavage efficiency (Fig. 2b) by dividing each by its respective control sample. Two-tailed t-tests were performed to estimate the significance of each treatment cleavage efficiency relative to its respective control. We note that, because FVP treatment completely blocks almost all rRNA cleavage steps, it is not possible to accurately estimate the time to reach 50% cleavage, so statistics were not determined.

2-O-methylation analysis. To determine 18S and 28S ribosomal RNA 2′-O-methylation levels over time, we applied RiboMethSeq computational analysis methods[34,71] to 5eU–seq sequencing reads. In brief, 2′-O-methylated nucleotides are substantially more resistant to alkaline hydrolysis compared to non 2′-O-methylated nucleotides, resulting in fewer RNA fragmentation events at these sites. To map the nucleotides where fragmentation occurred, sequencing adaptors are ligated to the 3′ ends of fragmented RNA and 3′ ends of cDNA. This enables the identification of 2′-O-methylation sites at the single-nucleotide resolution by performing end mapping of reads. Specifically, the 5′ ends of read 1 sequences, which correspond to the 3′ end of the fragmented RNA, are mapped to the reference rRNA sequence. Next, modification levels at a given position were estimated by calculating the number of 5′-end read counts at a given 2′-O-methylated site compared with that of their neighbouring nucleotides, defined as ScoreC (see below). Nucleotides that are 2′-O-methylated, due to their resistance to hydrolysis, have substantially fewer 5′ end read counts, and therefore appear as 'dips' or areas of low coverage in the end-mapping profile (Extended Data Fig. 1h,i).

We calculated ScoreC at known 2′-O-methylation sites[42] using a weighted average of the 5′ end read counts in a ±2 nucleotide window, recommended previously[72], around each site. Nucleotides in the ±1 and ±2 neighbouring positions were assigned weight contributions of 0.9 and 1, respectively. If a separate 2′-O-methylation site was found within the ±2 window around a site, the 5′ end read counts at the former were skipped and those at the immediately preceding nucleotide were

used alternatively. For the calculation of ScoreC, nucleotide positions of 2′-O-methylation sites on 18S rRNA were converted to those on 47S rRNA (U13369.1 human ribosomal DNA) by adding +3,655 to the 18S 2′-O-methylation positions (except for Am1678, Cm1703 and Um1804, to which +3,657 was added). For sites on 28S rRNA, nucleotides were converted to 28S 2′-O-methylation positions on 47S rRNA by adding +7,924, +7,920, +7,912, +7,911 and +7,903 for Am398 to Am400, Gm1316 to Gm2876, Cm3701 to Gm3944, Gm4042 to Cm4054, and Gm4196 to Gm4637, respectively. For data visualization, negative ScoreC values were clipped to zero. The heat map in Extended Data Fig. 3d was generated in Prism using the heat map function.

Defining fast and slow 2′-O-methylation sites. We measured the rates at which 2′-O-methylation occurs across all known 18S and 28S sites in our 5eU–seq data performed on MCF10A cells ($n = 2$ replicates) to determine which occur at a fast versus slow rate. 18S and 28S rRNA 2′-O-methylation sites that do not attain near steady state 2′-O-methylation levels within 30 min from transcription are defined as slow. All other 2′-O-methylation sites that meet this criterion and are defined as fast. Sites with high variation between replicates that made it challenging to confidently infer 2′-O-methylation rates were manually excluded. A table of high-confidence fast and slow 18S and 28S rRNA 2′-O-methylation sites is provided in Supplementary Table 1. We have provided examples of 5eU–seq data for individual high-confidence fast (Gm4494) and slow sites (18S-Cm1272, 28S-Cm3808, 28S-Um4498) in Extended Data Fig. 1i,j and Fig. 1h. The average of all high-confidence fast sites for each of 18S and 28S is shown in the SSU and LSU panels of Fig. 1h, respectively.

RiboMethSeq

RiboMethSeq for data in Extended Data Fig. 1g was conducted exactly as described previously[34]. For analysis, adapter sequences were trimmed from raw reads using Trimmomatic v0.39 with the following parameters: LEADING:30, TRAILING:30, SLIDINGWINDOW:4:15, AVGQUAL:30 and MINLEN:17. Quality control of the raw and trimmed reads was assessed using FastQC (v.0.11.9). Alignment to the reference rRNA sequence (18S: NR_003286.4; 5.8S: NR_003285.2; 28S: NR_003287.4) was done using Bowtie2 (v.2.3.5.1) with the default parameters. Sorting, indexing and extraction of mapped reads was done using Samtools (v.1.15.1), with the option -F 4 to exclude the unmapped reads. Subsequent analysis was conducted using R: the quantification of ribosomal RNA (rRNA) 2′-O-methylated residues was performed using the RNAmodR.RiboMethSeq package (v.1.18.0), the final processed data were exported using the writexl (v.1.5.0) package and display output was generated using Prism (v.10.3.0).

Pre-rRNA processing analysis by northern blotting

Total RNA was extracted from HEK293 cells labelled with or without 5eU with TRI reagent solution (AM9738, Thermo Fisher Scientific), according to the manufacturer's instructions. Then, 5 µg total RNA was resolved on a 1.2% agarose/6% PFA denaturing gel, transferred overnight by capillary onto a nylon Hybond N+ membrane (RPN203B, Cytiva), and hybridized with radioactively labelled probes (Supplementary Table 1). The probes were designed to detect all major pre-rRNA intermediates. The signal was acquired with a phosphorimager (FLA-7000, Fujifilm) and quantified using native multi-gauge software (v.3.1, Fujifilm).

Quantitative image analysis

All quantitative imaging measurements were performed using CellProfiler[73] v.4.2.6. Cell segmentation was performed using cellpose[74] v.2.3.2 and the RunCellpose plugin for cellprofiler. Full computational methods, pipelines and notebooks describing the calculation of the derived methods can be found at the GitHub repository (https://github.com/SoftLivingMatter/image-analysis-quinodoz-jiang-2024). To deploy cellprofiler plugins on HPC systems, a snakemake workflow[75] wrapper

was developed. It controls the resources and behaviour of each invocation and can be found at GitHub (https://github.com/softLivingMatter/snakemake-cellprofiler/).

Morphology. To quantitatively examine changes in cell morphology as a function of nucleolar perturbations, the following steps were performed in CellProfiler. First, the multichannel images were split into separate channels, such as GC, FC, DFC, FISH/5eU/other markers. The GC channel was used to define initial GC objects using minimum cross-entropy thresholding with a diameter range of 30–400 pixels, where each pixel corresponds to 0.0387 μm. Clumped objects were not separated as it produced too many falsely separated GC objects. As the images do not have a nuclear or cytoplasmic stain and some metrics are best measured across an entire cell, we computationally assigned nucleoli to the same cell based on if they were within 100 px to each other, producing a merged object mask. The mask was dilated by 50 px to measure metrics within the prospective nucleoplasm and find nucleolar features that may be outside the GC, such as FCs after FVP treatment, which causes detachment of the phases.

To find FC objects, the dilated GC objects were used to mask the FC image before performing 'enhancing speckles' with a feature size of 20 px using the Fast setting in the EnhanceOrSuppressFeatures module. The FC objects were found in the enhanced FC image using an adaptive, three-class Otsu threshold with the middle intensity class assigned to the background. This was selected to ensure that the identified FC objects were primarily in plane and in focus. The adaptive window was 100 px, clumped objects were separated by intensity and shape, and FC objects were selected with diameters of 7–50 px. As these FCs included objects within and outside of the GC, each FC was assigned to either a nucleolar or extra-nucleolar class using an overlap threshold of 50%. For example, an FC that overlaps an initial GC object by more than 50% was considered a nucleolar FC.

DFC objects were defined by masking the DFC image with the dilated GC objects. As the DFC phase organization is highly variable between treatments, the built-in IdentifyPrimaryObjects module was not able to perform adequately in all cases. Instead, DFCs were found by first thresholding with an adaptive, three-class otsu cut-off with a 150 px window. The middle class was assigned to background to ignore the diffuse DFC phase that develops after certain perturbations. The threshold image was converted to objects and then prospective DFCs were filtered to ensure they had an area of at least 20 px.

The GC, DFC and FC objects were combined to a single mask which was used as the support for measuring Pearson's correlation and overlap of the image channels. The size and shape of each object set was also measured and used for scaling some metrics, discussed below. The intensity of the FC channel was measured in FC objects, and GC and probe (for example, FISH probe or 5eU) were measured in the GC and DFC phases. The distribution of FC and DFC intensity was measured over the initial GC objects using 20 scaled bins. A binary image of the initial GC objects was also measured to facilitate combining bins during post-processing. Each object was related to its corresponding dilated GC object before exporting to a csv for further analysis in Python.

The raw data produced by cellprofiler was further processed using jupyter notebooks and custom analysis scripts. Each object csv was read into a pandas dataframe and merged into a final result by the image and dilated GC unique identifier. Values such as total area or FC count were summed to provide a per-cell measurement. Average intensities per cell were calculated by first multiplying the mean intensity from cellprofiler with the object area, summing the result, then dividing by the total area per cell. Rim enrichment was calculated by summing the radial distribution fraction for the bins of interest and dividing by the fraction of the GC object over the same range of bins. Investigation of a range of rim widths found that the outer 20% of the GC rim provided the best discrimination between U3 KD and control cells. Circularity was estimated as $4 \times \pi \times area/perimeter^2$.

RDF estimation. To facilitate broader utilization of Radial distribution function (RDF) measurements, we developed a cellprofiler plugin, MeasureRDF, for calculating the radial distributions of object sets, such as the intensities of FISH or 5eU signals within a 1 μm radius from the FC centre, on a given input image. A separate plugin allows for further flexibility in performing upstream object finding and filtering and simplifies integration into other analysis tasks. In contrast to the MeasureObjectIntensityDistribution method available in cellprofiler, the MeasureRDF plugin uses a fixed distance in pixels and attempts to resolve overlapping objects as described below.

In the point-based measurement mode, the MeasureRDF plugin operates on a set of objects as the point sources along with a containing object. Here we used the GC boundary as the masking objects and FCs as the point sources. For each GC, the set of FCs are considered together. The image intensities are mean-centred with unit variance and pixel distances from each FC are determined. The RDF distribution is estimated by minimizing the difference between the scaled image intensity and a superposition of each FC point source with the same RDF. This allows for deconvolution of neighbouring point sources while providing an averaged estimate of the RDF. The estimated intensities are rescaled to the original intensity units before reporting to the user. In all of the plots, the intensity is either min–max scaled between the minimum and maximum intensities in the RDF or max scaled by dividing by the maximum intensities in the RDF to highlight intensity dynamics.

To visualize the location of each phase from the FC centre, the RDF distributions of FC, DFC and GC can be plotted on a colour bar, where the intensity of a phase is mapped to a given colour (FC, green; DFC, red; GC, blue). To identify the boundaries between the distinct phases, the intensities of each phase were subtracted from the intensity of their adjacent phase before plotting. Specifically, the distance at which the intensity of pairs of phases is equal is used to estimate the boundary between phases. Finally, the 5eU RDF distributions were used to map the distance the 5eU RNA has travelled from the FC centre to its corresponding chase time. For each chase time, the location of maximum EU intensity (5eU peak) was determined and used in a piecewise-linear interpolation between time and distance.

The MeasureRDF plugin can also operate in a boundary-measurement mode, which was used for the SSU-only and nucleolar periphery analyses performed in Fig. 4 and Extended Data Fig. 10a–f. In this setting, the source object boundaries are considered at $r = 0$, defined as the radial position of 50% DFC or GC normalized intensity, and the image intensity is measured as a function of distance from the boundary. The distance of each pixel to the object boundary is determined and used to estimate the RDF curve. In cases in which neighbouring point sources overlap, pixel intensities are assigned to the closest object.

Engineered plasmid measurements. For the images of de novo nucleoli, we manually classified individual nucleoli as endogenous, de novo or hybrid on the basis of their intensities for plasmid-expressed 18S*/28S* RNA and endogenous 5′ ETS rRNA. Specifically, endogenous nucleoli were those with high endogenous 5′ ETS RNA-FISH and no detectable plasmid-expressed 18S*/28S* RNA-FISH signal. Conversely, de novo nucleoli were those with high 18S*/28S* plasmid RNA-FISH signal, and no detectable endogenous 5′ ETS signal. Hybrid nucleoli contained FISH signals for both channels. Figure 3d demonstrates the range of nucleolar intensities of 5′ ETS and plasmid-expressed FISH intensities observed before further manual classification, where only high-confidence de novo versus endogenous nucleoli were analysed and any ambiguous nucleoli were excluded.

As the SSU-only rDNA plasmid produced nucleoli without detectable NPM1 intensity, a separate workflow was required to evaluate a subset of the morphology measurements described above. First, each channel was background corrected by subtracting the bottom 5 percentile value of each image. Next, the DFC (NOP56 or FBL) channel was blurred with a 5-px sigma Gaussian filter, which was found to produce better

Article

segmentation of SSU-only nucleoli. The blurred DFC image was used to detect nucleoli with a two-class global Otsu threshold and diameters between 10 and 150 px without declumping. The initial nucleoli objects were dilated by 10 px to act as support for the rim-based RDF measurement. Each channel's intensity was measured in the nucleoli and the 10-px rim as well as the object size and shape. For quality control, we manually checked the segmented SSU-only nucleoli objects and excluded those that were out of focus or incorrectly segmented.

To measure cytoplasmic and nuclear intensities of the 18S* or 28S* RNA expressed from engineered plasmids, nuclei were segmented from the endogenous 28S FISH using cellpose with the nuclei model (inverted mask) and an expected object diameter of 300 px. The entire cell extents were then segmented from the endogenous 28S FISH stain (non-inverted mask) using the cyto2 cellpose model and an object diameter of 500 px. The whole-cell and nucleus objects were masked to ensure that each cell had a nucleus and vice versa. Then, the cell objects were masked with the nucleus to define the cytoplasm. The background subtracted endogenous 28S and engineered 18S* or 28S* RNA intensities were measured in the nuclei and cytoplasm.

Assumptions used for nucleolar phase-field modelling
As multiphase condensates, the organization of the nucleolar phases should be strongly impacted by the relative interfacial tensions ($\gamma_{i,j}$) between each of the phases (i,j), which is a measure of the energy per unit area associated with interfaces[13,55–57,76]. The relative interfacial tensions are expected to depend on the local concentrations of rRNA species and associated proteins (Fig. 5a), flux and biochemical nature of the underlying molecular species[77].

Specifically, we modelled the affinities and localization of different species to be consistent with our experimental observations: nascently transcribed pre-rRNA in the FC/DFC boundary, 18S rRNA precursors before 5′ ETS cleavage in the DFC, and 18S rRNA and 28S rRNA precursors in the GC (Fig. 5a). Importantly, these rRNAs are not alone and form hundreds of interactions with proteins. Indeed, owing to its interactions with many assembly proteins and RNAs, the SSU processome represents a high-valency particle, of which the maturation, including the cleavage and degradation of 5′ ETS, releases 50 assembly factors to generate a pre-40S particle[44,78–80].

A standard pairwise interaction term in the Flory–Huggins model encodes the affinity of rRNA to each nucleolar component and therefore the rRNA partitioning. Specifically, given our findings that U3-processing-deficient 18S precursors appear trapped within the DFC (Fig. 4b,d,h), our model assumes that these species have a high affinity for DFC, and a low affinity for the GC. Conversely, because 18S pre-rRNAs with normal processing flux into GC or nucleoplasm (Fig. 4b,d,h,i), we assume that 18S pre-rRNAs after 5′ ETS cleavage have a low affinity for the DFC and a higher affinity for the GC. Additional details are provided in Supplementary Note 2.

Reporting summary
Further information on research design is available in the Nature Portfolio Reporting Summary linked to this article.

Data availability
All data supporting the findings of this study are available in the Article and its Supplementary Information. All genomics data are available at the Gene Expression Omnibus (GEO) under accession numbers GSE296080 and GSE296162. Source data are provided with this paper.

Code availability
All codes and pipelines used for this study are provided at GitHub and Zenodo: https://github.com/SoftLivingMatter/image-analysis-quinodoz-jiang-2024 (https://zenodo.org/records/14908468)[81]; https://github.com/SoftLivingMatter/snakemake-cellprofiler (https://zenodo.org/records/14908470)[82]; and https://github.com/SoftLivingMatter/5eU-seq-pipelines (https://zenodo.org/records/14908466)[83]. Example images and analysis notebooks are provided at Zenodo (https://doi.org/10.5281/zenodo.14910509)[84].

61. Ietswaart, R. et al. Genome-wide quantification of RNA flow across subcellular compartments reveals determinants of the mammalian transcript life cycle. *Mol. Cell* **84**, 2765–2784 (2024).
62. Sanders, D. W. et al. Distinct tau prion strains propagate in cells and mice and define different tauopathies. *Neuron* **82**, 1271–1288 (2014).
63. Cong, L. et al. Multiplex genome engineering using CRISPR/Cas systems. *Science* **339**, 819–823 (2013).
64. Koch, B. et al. Generation and validation of homozygous fluorescent knock-in cells using CRISPR–Cas9 genome editing. *Nat. Protoc.* **13**, 1465–1487 (2018).
65. Simsek, D. et al. The mammalian Ribo-interactome reveals ribosome functional diversity and heterogeneity. *Cell* **169**, 1051–1065 (2017).
66. Banerjee, A. K. et al. SARS-CoV-2 disrupts splicing, translation, and protein trafficking to suppress host defenses. *Cell* **183**, 1325–1339 (2020).
67. Bolger, A. M., Lohse, M. & Usadel, B. Trimmomatic: a flexible trimmer for Illumina sequence data. *Bioinformatics* **30**, 2114–2120 (2014).
68. Dobin, A. et al. STAR: ultrafast universal RNA-seq aligner. *Bioinformatics* **29**, 15–21 (2013).
69. Li, H. et al. The Sequence Alignment/Map format and SAMtools. *Bioinformatics* **25**, 2078–2079 (2009).
70. Liao, Y., Smyth, G. K. & Shi, W. featureCounts: an efficient general purpose program for assigning sequence reads to genomic features. *Bioinformatics* **30**, 923–930 (2014).
71. Birkedal, U. et al. Profiling of ribose methylations in RNA by high-throughput sequencing. *Angew. Chem. Int. Ed.* **54**, 451–455 (2015).
72. Pichot, F. et al. Holistic optimization of bioinformatic analysis pipeline for detection and quantification of 2'-O-methylations in RNA by RiboMethSeq. *Front. Genet.* **11**, 38 (2020).
73. Stirling, D. R. et al. CellProfiler 4: improvements in speed, utility and usability. *BMC Bioinform.* **22**, 433 (2021).
74. Pachitariu, M. & Stringer, C. Cellpose 2.0: how to train your own model. *Nat. Methods* **19**, 1634–1641 (2022).
75. Mölder, F. et al. Sustainable data analysis with Snakemake. *F1000Res.* **10**, 33 (2021).
76. Simon, J. R., Carroll, N. J., Rubinstein, M., Chilkoti, A. & López, G. P. Programming molecular self-assembly of intrinsically disordered proteins containing sequences of low complexity. *Nat. Chem.* **9**, 509–515 (2017).
77. Sanchez-Burgos, I., Herriott, L., Collepardo-Guevara, R. & Espinosa, J. R. Surfactants or scaffolds? RNAs of varying lengths control the thermodynamic stability of condensates differently. *Biophys. J.* **122**, 2973–2987 (2023).
78. Cheng, J. et al. 90S pre-ribosome transformation into the primordial 40S subunit. *Science* **369**, 1470–1476 (2020).
79. Du, Y. et al. Cryo-EM structure of 90S small ribosomal subunit precursors in transition states. *Science* **369**, 1477–1481 (2020).
80. Riback, J. A. et al. Composition-dependent thermodynamics of intracellular phase separation. *Nature* **581**, 209–214 (2020).
81. Quinodoz, S. A. et al. Image analysis code for 'Mapping and engineering RNA-driven architecture of the multiphase nucleolus'. *Zenodo* https://doi.org/10.5281/zenodo.14908467 (2025).
82. Quinodoz, S. A. et al. Snakemake CellProfiler wrapper for 'Mapping and engineering RNA-driven architecture of the multiphase nucleolus'. *Zenodo* https://doi.org/10.5281/zenodo.14908469 (2025).
83. Quinodoz, S. A. et al. 5eU-seq pipelines for 'Mapping and engineering RNA-driven architecture of the multiphase nucleolus'. *Zenodo* https://doi.org/10.5281/zenodo.14908465 (2025).
84. Quinodoz, S. A. et al. Example images and analysis notebooks for 'Mapping and engineering RNA-driven architecture of the multiphase nucleolus'. *Zenodo* https://doi.org/10.5281/zenodo.14910508 (2025).
85. Birkedal, U. et al. Profiling of ribose methylations in RNA by high-throughput sequencing. *Angew. Chem. Weinheim Bergstr. Ger.* **127**, 461–465 (2015).

Author contributions S.A.Q., L.J., C.P.B., S.K. and D.L.J.L. designed the study. S.A.Q., L.J., A.A.A.-A., L.W.W., J.F.B., A.D., E.S., L.W., P.B. and C.Z. performed experiments. S.A.Q., L.J., A.A.A.-A., T.J.C., C.Z. and L.W.W. performed imaging and genomic data analysis. H.Z. and Q.Y., with advice from A.K. and C.P.B., performed simulation and kinetic modelling. S.A.Q., L.J., D.L.J.L., S.K. and C.P.B. wrote the manuscript with input from all of the authors. S.A.Q. and L.J. made the figures with contributions from all of the authors.

Competing interests C.P.B. is a scientific founder, scientific advisory board member, shareholder and consultant for Nereid Therapeutics. The other authors declare no competing interests.

Additional information
Supplementary information The online version contains supplementary material available at https://doi.org/10.1038/s41586-025-09207-4.
Correspondence and requests for materials should be addressed to Denis L. J. Lafontaine, Sebastian Klinge or Clifford P. Brangwynne.
Peer review information *Nature* thanks David Shechner and the other, anonymous, reviewer(s) for their contribution to the peer review of this work
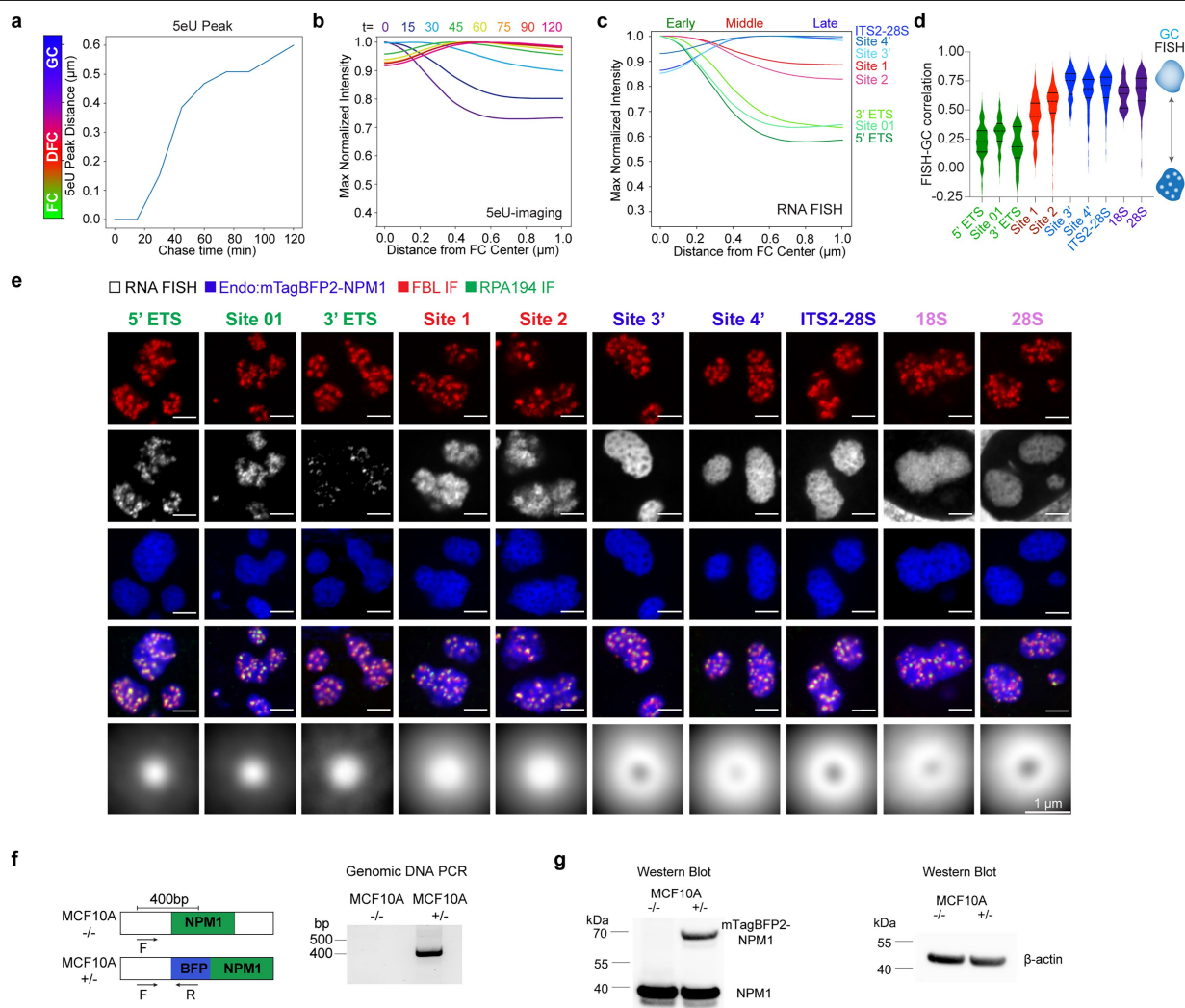**Reprints and permissions information** is available at http://www.nature.com/reprints.

Article
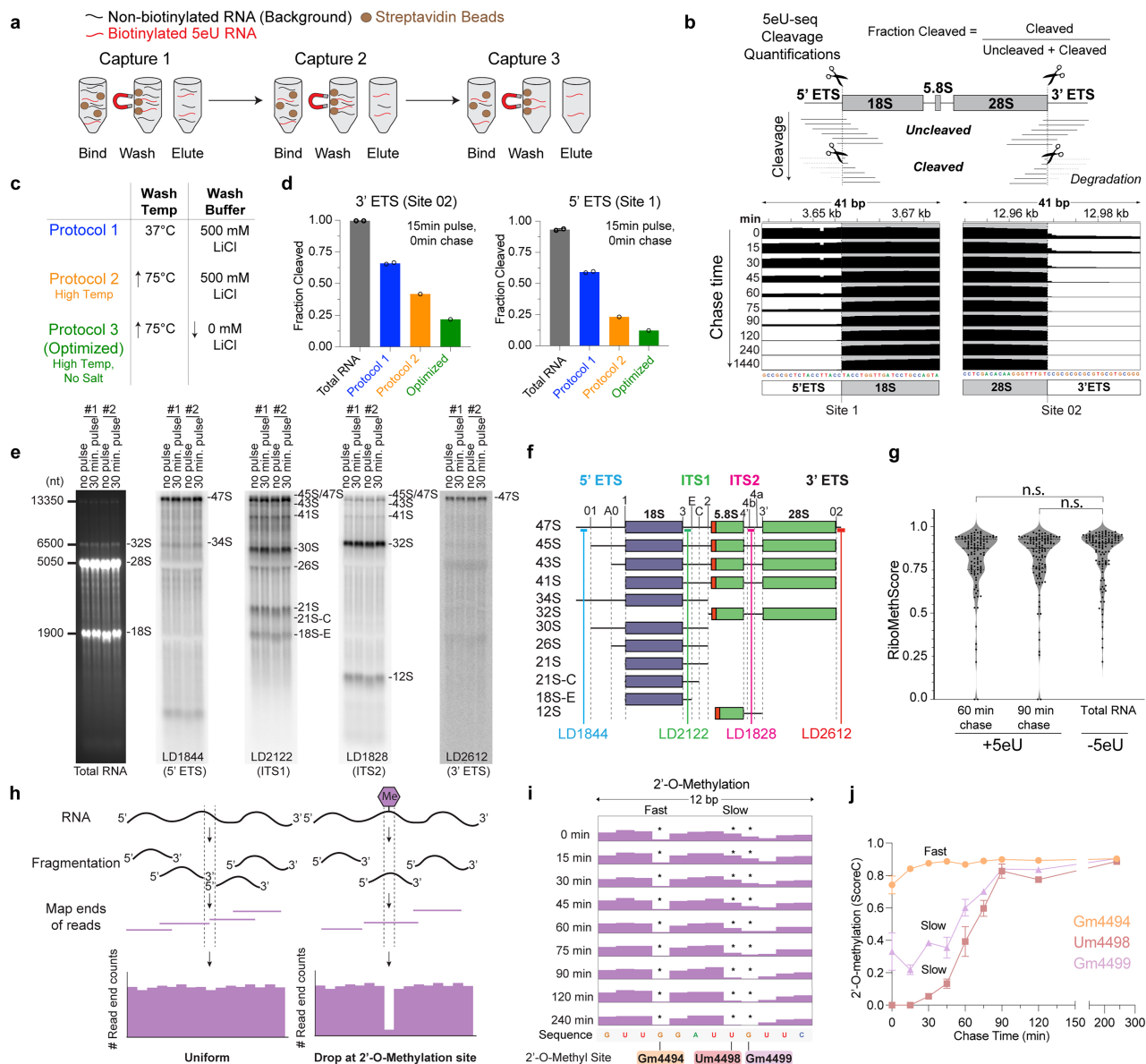
Extended Data Fig. 1 | 5eU-seq method description and validation.
**a**, Schematics of the 5eU-sequencing protocol with 3 rounds of sequential captures. **b**, The "fraction cleaved" metric is calculated by measuring the number of "cleaved" reads (ending at a cut site) divided by the total number of reads (uncleaved (spanning a cut site) + cleaved). Bottom, examples of 5eU-seq data demonstrating single nucleotide resolution mapping of rRNA cleavage at specific sites (1 and O2) over time in MCF10A cells. **c**, Optimization of wash temperature and buffer conditions to reduce background from mature rRNA. **d**, The fraction of reads cleaved at O2 and 1 sites comparing Protocols 1, 2, and 3 on 5eU pulse-labelled material (15 min pulse, 0 min chase) from HEK293T cells. Protocol 3 is the optimized protocol used for all datasets in this paper. Total RNA is a reference for mature rRNA. n = 1 (Protocol 2 and 3), 2 (Protocol 1, total RNA) replicates. **e**, Northern blot analysis of 5eU pulse-labelled material

(30 min) and unlabelled material as a control (no pulse) from HEK293T cells. Two replicates were performed. **f**, Northern blot probes used in e. **g**, RiboMethScore of 2′-O-Methylation for 5eU 30 min pulse labelled material (+5eU, 60 or 90 min chase) and unlabelled material as a control (−5eU). Modification levels are not significantly (n.s.) different across n = 108 2-O-Me sites between conditions (two-tailed t-test). **h**, Schematic (adapted from[85]) explaining the detection of 2′-O-methylation levels by mapping 5′ ends of reads. Drops in read end counts are observed at modified sites; see methods. **i**, Example 5′ end read coverage at fast (Gm4494, 28S) and slow (Um4498, Gm4499, 28S) 2′-O-methylation sites over 0-240 min chase timepoints. **j**, Quantification of 2′-O-methylation levels (ScoreC) over 0-240 min chase timepoints at 28S Gm4494, Um4498, Gm4499 2′-O-methylation sites shown in i. n = 2 per timepoint. Error bars are s.e.m.

a, 5eU Peak

b, t= 0 15 30 45 60 75 90 120 — 5eU-imaging

c, Early Middle Late — RNA FISH — ITS2-28S, Site 4', Site 3', Site 1, Site 2, 3' ETS, Site 01, 5' ETS

d, FISH-GC correlation — GC FISH — 5' ETS, Site 01, 3' ETS, Site 1, Site 2, Site 3', Site 4', ITS2-28S, 18S, 28S

e, □ RNA FISH ■ Endo:mTagBFP2-NPM1 ■ FBL IF ■ RPA194 IF

5' ETS | Site 01 | 3' ETS | Site 1 | Site 2 | Site 3' | Site 4' | ITS2-28S | 18S | 28S

1 µm

f, 400bp — MCF10A -/- NPM1 — F ; MCF10A +/- BFP NPM1 — F R

Genomic DNA PCR — MCF10A -/- MCF10A +/- — bp 500 400

g, Western Blot — MCF10A -/- +/- — kDa 70 55 40 — mTagBFP2-NPM1, NPM1

Western Blot — MCF10A -/- +/- — kDa 55 40 — β-actin

Extended Data Fig. 2 | RNA FISH and 5eU-imaging of rRNA flux as well as characterization of endogenously tagged mTagBFP2-NPM1 cells. a, Peak of 5eU signal (distance from the centre of FCs) over chase time quantified in Fig. 1e. **b**, Max normalized 5eU intensity over distance from the centre of FCs over time, quantified in Fig. 1e. **c**, Max normalized FISH intensity over distance from FC centre, quantified from images in e. **d**, Pearson correlation coefficient between all FISH probes and GC from images in e. Number of nucleoli (n) = 72 (5' ETS), 95 (3' ETS), 24 (Site 01), 111 (Site 1), 230 (Site 2), 38 (Site 3'), 105 (Site 4'), 318 (ITS2-28S), 72 (18S), 310 (28S). Violin plots are centred by median and quartiles are shown. **e**, Example images of RNA FISH probes in Fig. 1j, with FC (RPA194 IF), DFC (FBL IF), and GC (mTagBFP2-NPM1) shown. Scale bar = 3 µm. Bottom: averaged FISH images around individual FCs. Scale bar = 1 µm. **f**, Junction PCR of a 400 bp genomic region spanning the inserted mTagBFP2 in MCF10A -/- (parental) and +/- (one copy of NPM1 tagged) cells. For gel source data, see Supplementary Fig. 1b. **g**, Western blot for NPM1 in MCF10A -/- and +/- cells with β-actin as loading control. For gel source data, see Supplementary Fig. 1a.
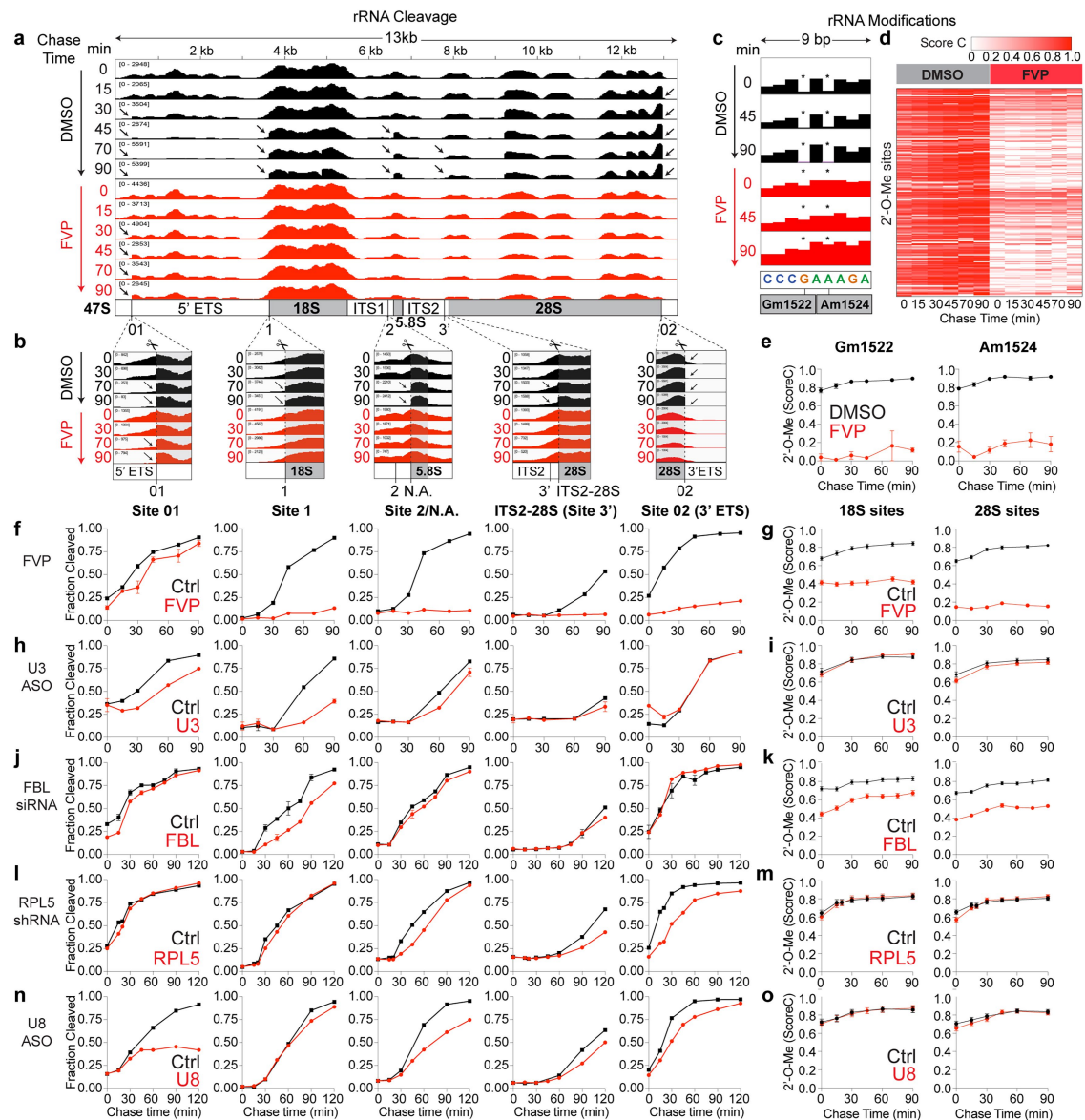
Extended Data Fig. 3 | Example 5eU-seq data and altered pre-rRNA cleavage and modification measured by 5eU-seq upon all perturbations. a, 5eU-seq reads over 47S pre-rRNA for 15 min pulse labelled material over 0-90 min chase timepoints in DMSO-treated (black) and FVP-treated (red) MCF10A cells. FVP-treated cells were pretreated with 2 µM FVP for 1 hr. prior to 5eU pulse-chase and throughout the time course. Arrows indicate where the sequencing reads are changing over time upon cleavage. **b**, Zoom-in examples of 5eU-seq reads at 01, 1, 2/NA, 3′/ITS2-28S and 02/3′ ETS regions in a. Dashed lines demarcate the cleavage sites and arrows indicate where the sequencing reads are changing over time upon cleavage. **c**, Zoom-in on 5′ end read counts in DMSO-control or FVP-treated conditions over 0-90 min chase timepoints in 28S rRNA at Gm1522 and Am1524 2′-O-methylation sites. FVP causes impaired 2′-O-methylation, observed by loss of characteristic drops at 2′-O-Me sites. **d**, Heatmap of 2′-O-Me levels (ScoreC) at all 18S and 28S rRNA sites in control (DMSO) and FVP-treated conditions over 0-90 min chase timepoints. **e**, Quantification of 2′-O-Me levels (ScoreC) over 0-90 min chase timepoints at the 28S Gm1522 and 28S Am1524 sites (plotted in c) upon DMSO and FVP treatment. n (replicates) = 2 per time point. **f-n**, Quantification of the fraction of RNA cleaved at each site displayed in b for MCF10A cells upon perturbations to rRNA processing (red): FVP-treatment or knockdown of U3 snoRNA (U3 ASO), Fibrillarin (FBL siRNA), RPL5 (RPL5 shRNA), and U8 snoRNA (U8 ASO) compared to their respective controls (black; DMSO for FVP, or scramble/negative control for ASO, siRNA, and shRNA treatments). n = 1 (U8, RPL5) or 2 (FVP, U3, Fib) per time point. **g-o**, Average 2′-O-Me levels (ScoreC) on 18S (left) and 28S (right) rRNA in perturbations (red) and control conditions (black) over 0-90 min chase timepoints. n = 1 (U8, RPL5) or 2 (FVP, U3, Fib) per time point. All error bars are s.e.m. All data collected from MCF10A cells.
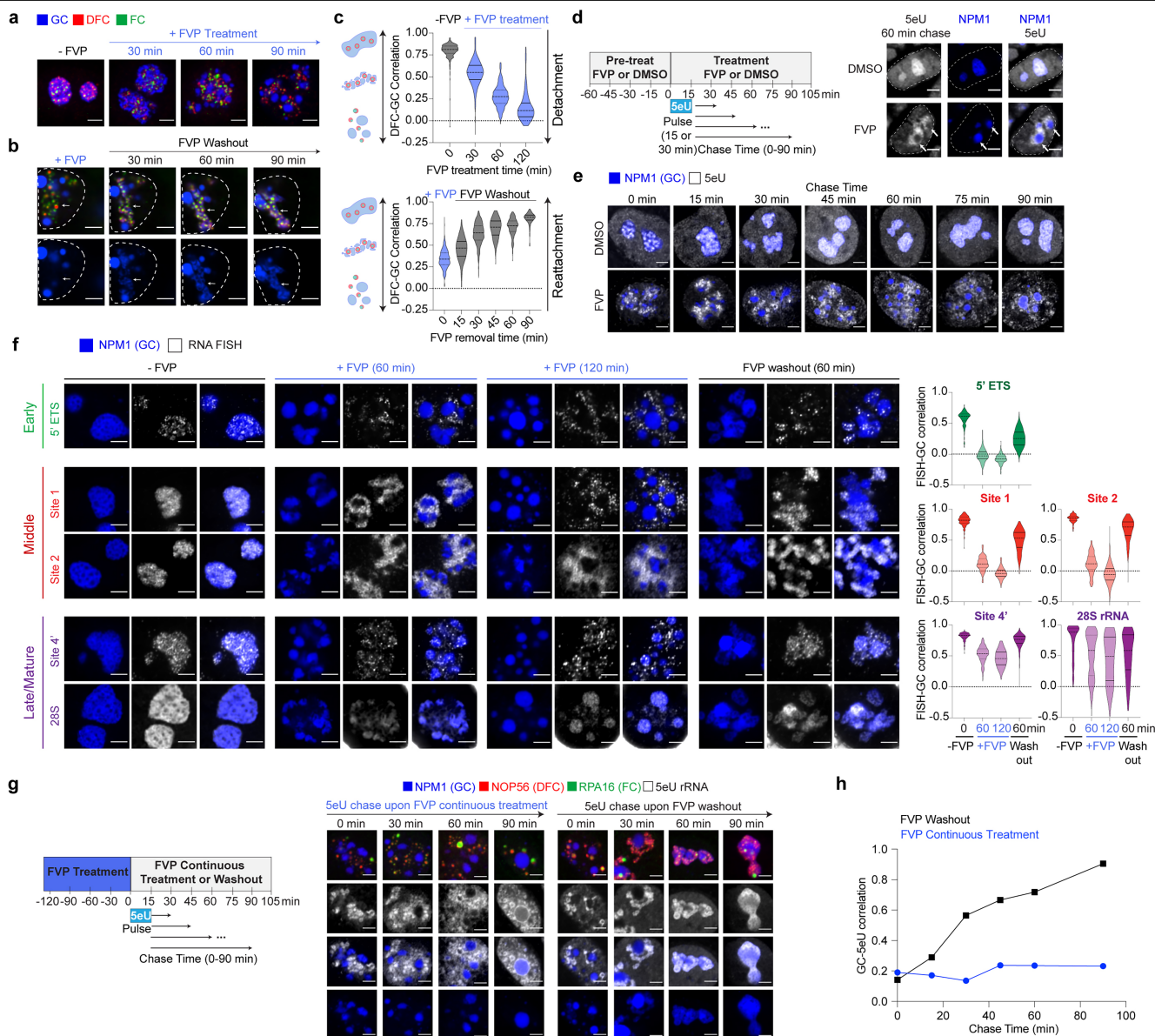
Extended Data Fig. 4 | Altered localization of RNA species and nucleolar morphology upon FVP treatment. a, Nucleolar morphology (IF for RPA194, FBL, and NPM1 for FC, DFC and GC) in DMSO (-FVP) and after 30-90 min of 2 μM FVP treatment. **b**, Nucleolar morphology–FC (RPA16-GFP), DFC (NOP56-mCherry), and GC (mTagBFP2-NPM1)–after 0-90 min of FVP washout. Dashed lines demarcate nuclei; arrows indicate examples of GC reattachment to FC/DFC. **c**, Pearson correlation between DFC and GC signals from **a** and **b**. Left: Schematics illustrate GC detachment. Detachment: n = 303, 383, 327, 87 cells (0-120 min); Reattachment: n = 464, 291, 490, 182, 230, 182 cells (0-90 min). **d-e**, Schematic of 5eU pulse-chase scheme and example images of 5eU labelled RNA upon FVP perturbations. d, Representative images of 5eU-labelled RNA (30 min pulse, 60 min chase) and GC (mTagBFP2-NPM1) upon DMSO or 2 μM FVP treatment. Arrows demarcate 5eU labelled rRNA at the periphery of GC. **e**, Example images of 5eU RNA (15 min pulse, 0-90 min chase)

and GC (mTagBFP2-NPM1) for correlation analysis in Fig. 2c (FVP-treated samples). **f**, RNA FISH upon 2 μM FVP treatment for 0 (-FVP), 60 (+FVP), and 120 min (+FVP), or 60 min FVP washout; GC (mTagBFP2-NPM1). Right: Pearson correlation between GC and FISH probes (5′ ETS: n = 91, 209, 320, 366; Site 1: n = 183, 58, 247, 291; Site 2: n = 127, 69, 272, 263; Site 4′: n = 139, 156, 86, 265; 28S rRNA: n = 138, 285, 196, 851 cells). **g**, 5eU pulse-chase scheme (15 min pulse, 0-90 min chase) and flux upon continuous FVP treatment or FVP washout. Bottom: FC (RPA16-GFP), DFC (NOP56-mCherry), and GC (mTagBFP2-NPM1), and 5eU RNA. **h**, Pearson correlation between 5eU and GC from g (Continuous: n = 221, 344, 358, 230, 273, 392 cells (0-90 min); Washout: n = 464, 291, 490, 182, 230, 182 cells (0-90 min)). Error bars are s.e.m. All scale bars = 3 μm. Violin plots are centred by median and quartiles are shown. MCF10A cells used except for d (HEK293T).
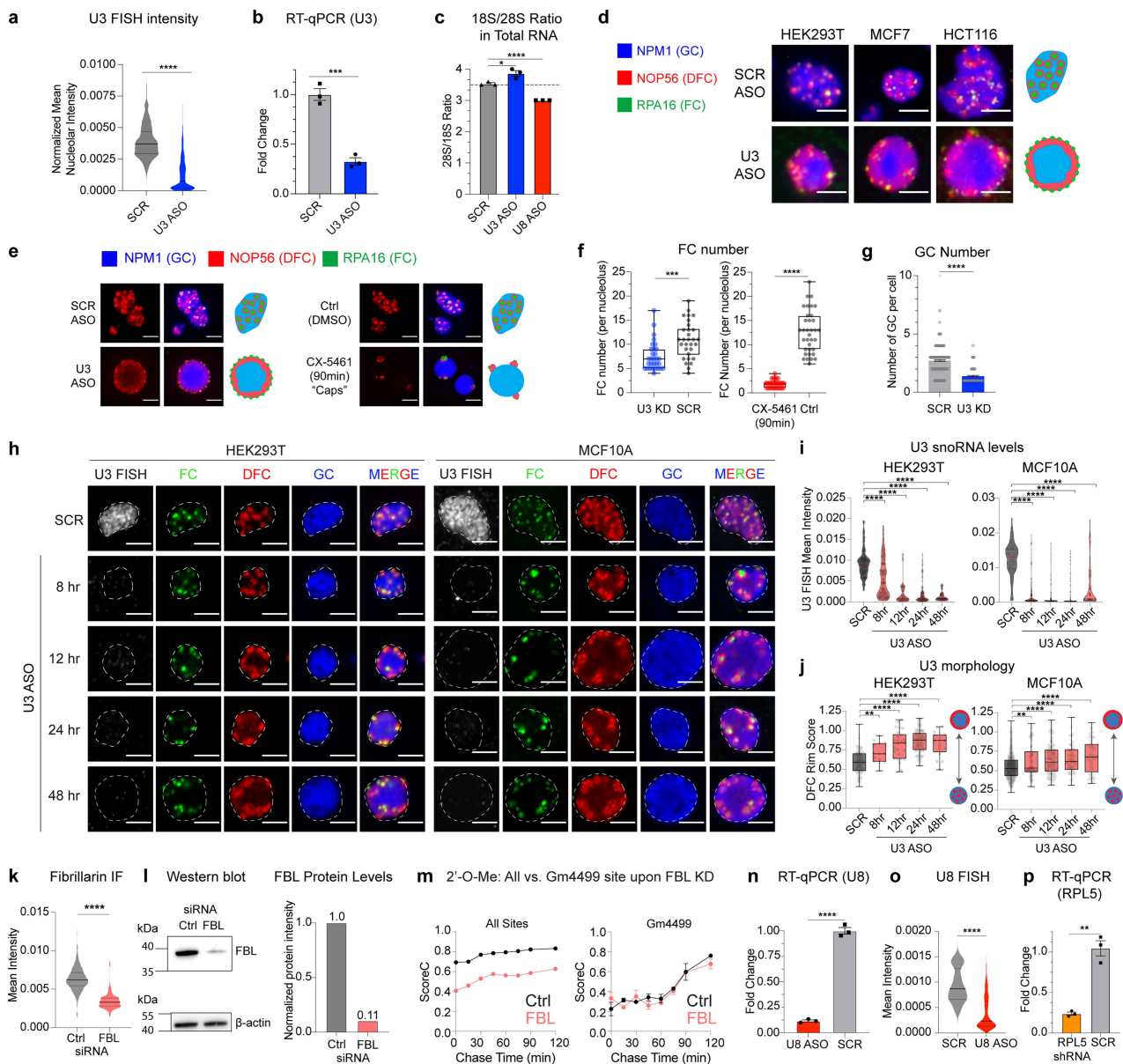
Extended Data Fig. 5 | Validation of all knockdowns performed in this study and comparison of nucleolar morphology between U3 snoRNA KD and Pol I inhibition. a, Quantification of U3 snoRNA FISH intensity in nucleoli from scramble (SCR, n = 479) and U3 ASO-treated (n = 329) cells. **** p-value < 0.0001. **b**, RT-qPCR analysis for U3 snoRNA levels 72 hrs. post-treatment with SCR or U3 ASO (n = 3 biological replicates per condition). *** p-value = 0.0006. **c**, 18S/28S rRNA ratio (RNA electrophoresis) in total RNA isolated 72 hrs. after SCR, U3, or U8 ASO treatment (n = 3 biological replicates per condition). * p-value = 0.0241, **** p-value < 0.0001. **d**, Nucleolar morphology in HCT116, HEK293T, and MCF7 cells following SCR or U3 ASO treatment. **e**, Nucleolar morphology following U3 ASO or CX-5461 (Pol I inhibition) treatment. Markers: GC (mTagBFP2-NPM1), DFC (NOP56-mCherry), and FC (RPA16-GFP) for d and e. **f**, Number of FCs per nucleolus in U3 ASO (n = 30), SCR ASO (n = 30), CX-5461 (n = 35), and control (n = 31) nucleoli. *** p-value = 0.0002, **** p-value < 0.0001. **g**, Number of GCs per cell in SCR (n = 384) and U3 ASO (n = 177) conditions. **** p-value < 0.0001. **h**, Time course of nucleolar reorganization following 8-48 h of U3 ASO treatment in MCF10A (immunofluorescence for FC: RPA194; DFC: FBL; GC: RRP1) and HEK293T (endogenously tagged UBTF-sfGFP (FC), FBL-Halotag (DFC), and NPM1-mtagRFP (GC)) cells. **i**, Quantification of U3 snoRNA FISH from h.

**** p-value: <0.0001 (two-tailed t-test), HEK293T: n = 160, 110, 46, 284, 27 nucleoli; MCF10A: n = 204, 147, 177, 97, 135 nucleoli. **j**, DFC rim score following U3 ASO treatment from h. ** p-value = 0.0069 (HEK293T), 0.0088 (MCF10A), **** p-value = <0.0001, HEK293T: n = 160, 14, 27, 167, 17 cells; MCF10A: n = 1050, 94, 138, 83, 68 cells. **k**, Mean nucleolar FBL intensity by IF upon FBL (n = 278) or control siRNA (n = 541) treatment. **l**, Western blot of FBL protein levels; β-actin serves as a loading control; For gel source data, see Supplementary Fig. 1c. **m**, 2′-O-Me levels (ScoreC) at 28S Gm4499 (right), a site modified independently from FBL, and averaged across all other 18S and 28S sites (left) in control and FBL KD treatment conditions measured by 5eU-seq over 15 min pulse, 0-120 min chase timepoints. n = 1-2 per time point. **n**, Fold change in U8 snoRNA levels (RT-qPCR; n = 3 biological replicates per condition). **o**, Quantification of U8 snoRNA FISH intensity in nucleoli upon SCR (n = 174) or U8 (n = 40) ASO treatment. **p**, Fold change in RPL5 mRNA expression by RT-qPCR (n = 3 biological replicates per condition). **** p-value < 0.0001, ** p-value = 0.0011. All scale bars = 3 μm. Box plots show medians (lines), boxes (25th-75th percentiles), whiskers (min-max). Violin plots: centred by median and quartiles shown. All error bars are s.e.m. Statistical tests are two-tailed Mann Whitney tests unless otherwise noted. MCF10A cells used unless otherwise stated.
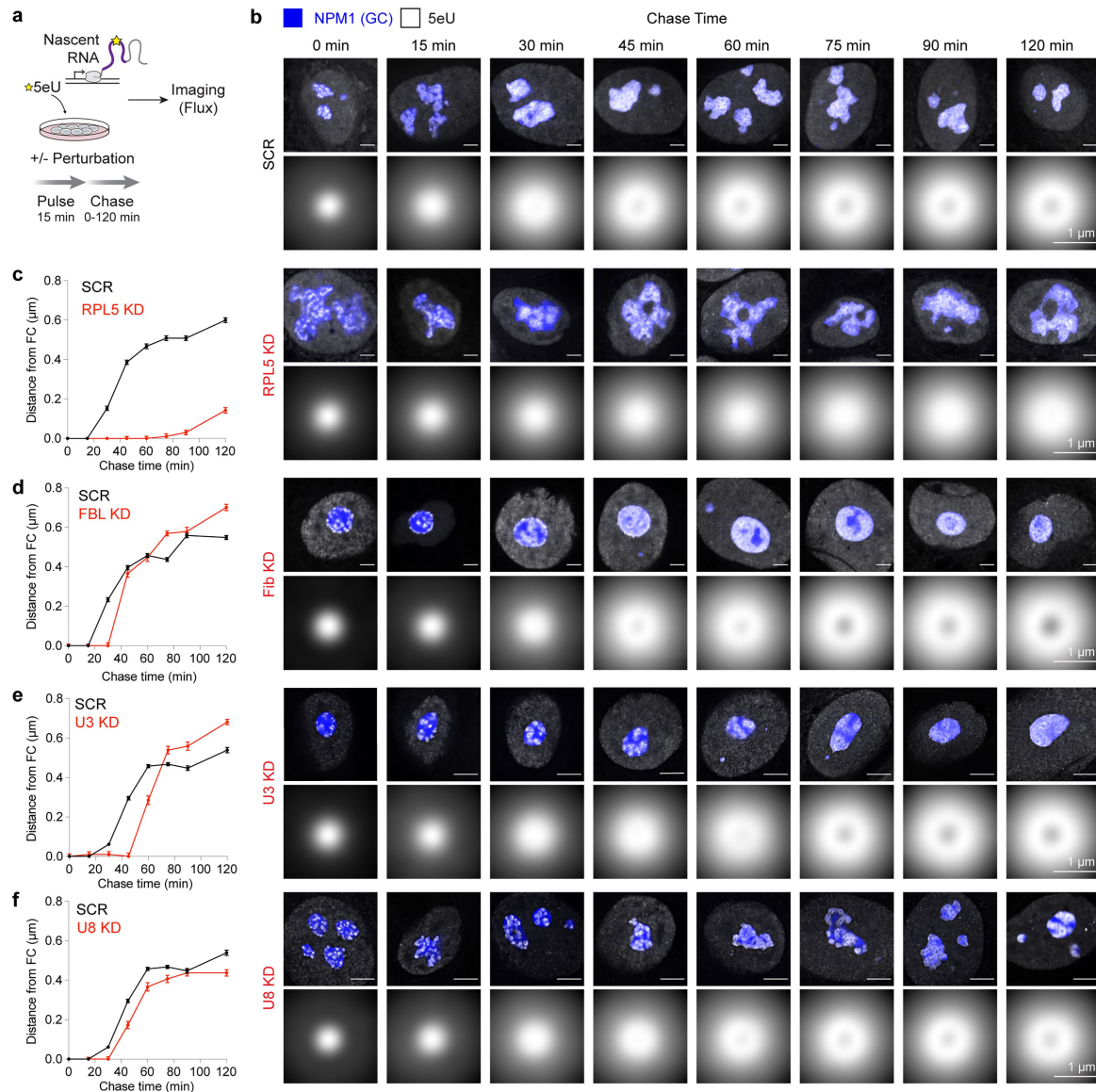
**Extended Data Fig. 6 | 5eU-imaging examples for processing perturbations.**
a, Schematic of experimental workflow: cells were treated with various
pre-rRNA processing perturbations followed by a 15 min 5eU pulse and chase
time course (0-120 min). **b**, Representative images of 5eU-labelled RNA (white)
and nucleoli (GC: mTagBFP2-NPM1, blue) in MCF10A cells over indicated chase
timepoints under control (SCR) and perturbation conditions. Bottom,
averaged 5eU intensity relative to individual FCs for each condition over time.
Scale bars = 3 µm (cells) and 1 µm (averaged images). **c-f**, Quantification of 5eU
peak distance from the centre of FCs over time for all perturbation conditions
shown in b compared to corresponding controls. Number of nucleoli >100 for
each time point per condition (see source data for specific n numbers). All error
bars are s.e.m.
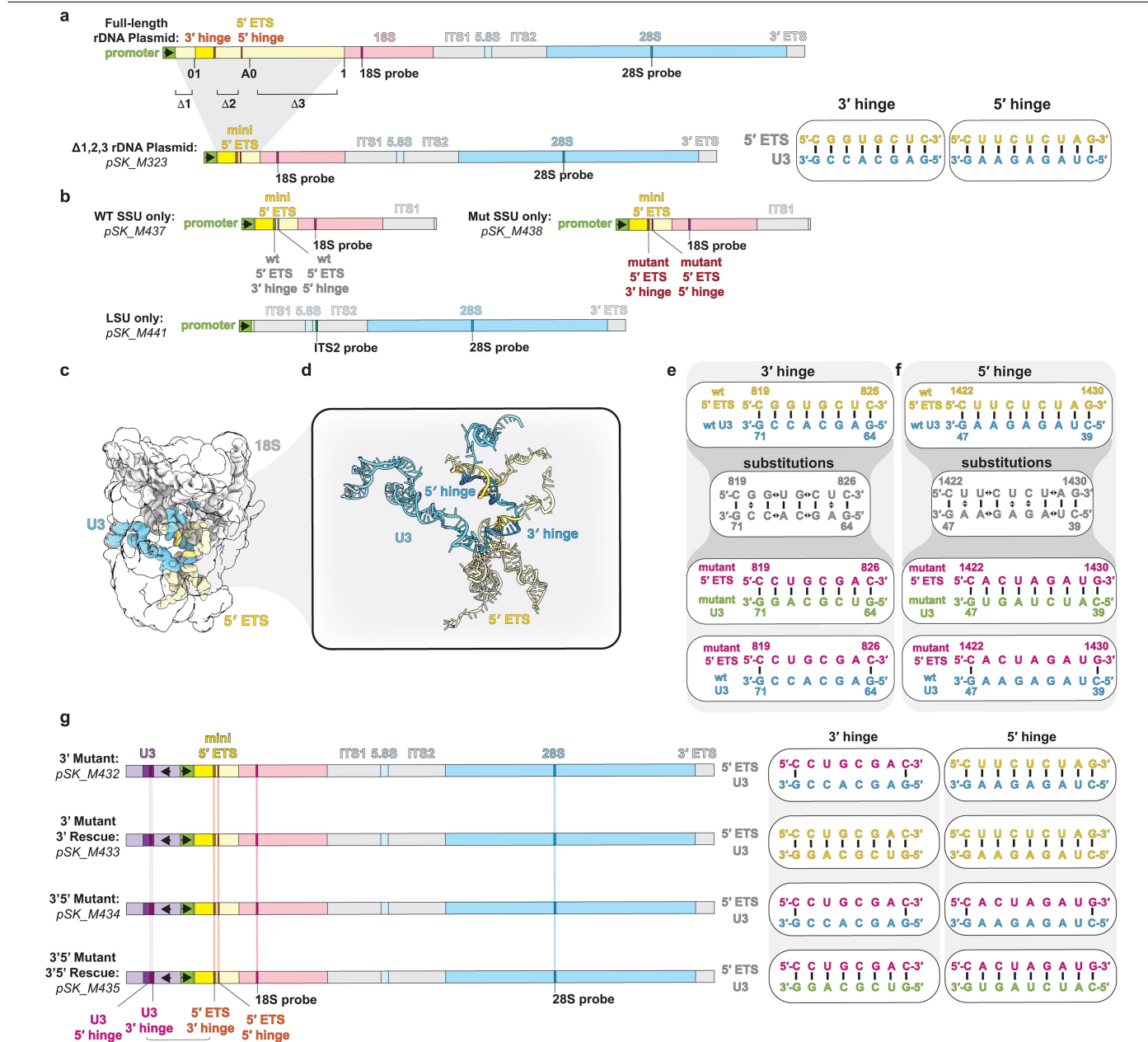
Extended Data Fig. 7 | Engineered rDNA plasmid designs used in this study. **a**, Schematics of endogenous (top) 47S rDNA and synthetic (bottom, pSK_ M323) rDNA plasmid with minimized (mini) 5′ ETS. Sequences of 3′ and 5′ hinge regions of 5′ ETS-U3 snoRNA base pairing are shown. **b**, Schematics of wildtype (WT) synthetic SSU-only, 5′ ETS 3′ hinge mutant SSU-only, and wildtype LSU-only rDNA plasmids. **c**, Structure of SSU processome in state pre-A1 (PDB: 7mq8). **d**, Zoom-in on 5′ and 3′ hinge RNA duplexes between the U3

snoRNA and 5′ ETS in c. **e-f**, Sequences of 3′ (e) and 5′ (f) hinges of 5′ ETS-U3 snoRNA base pairing in wildtype (WT), mutant 5′ ETS with mutant U3, and mutant 5′ ETS with WT U3 conditions. Sequence substitutions for mutants are marked by double-sided arrows. **g**, Schematics of complete U3 snoRNA gene combined with rDNA plasmids with 5′ ETS and U3 snoRNA 5′ hinge and 3′ hinge mutations.
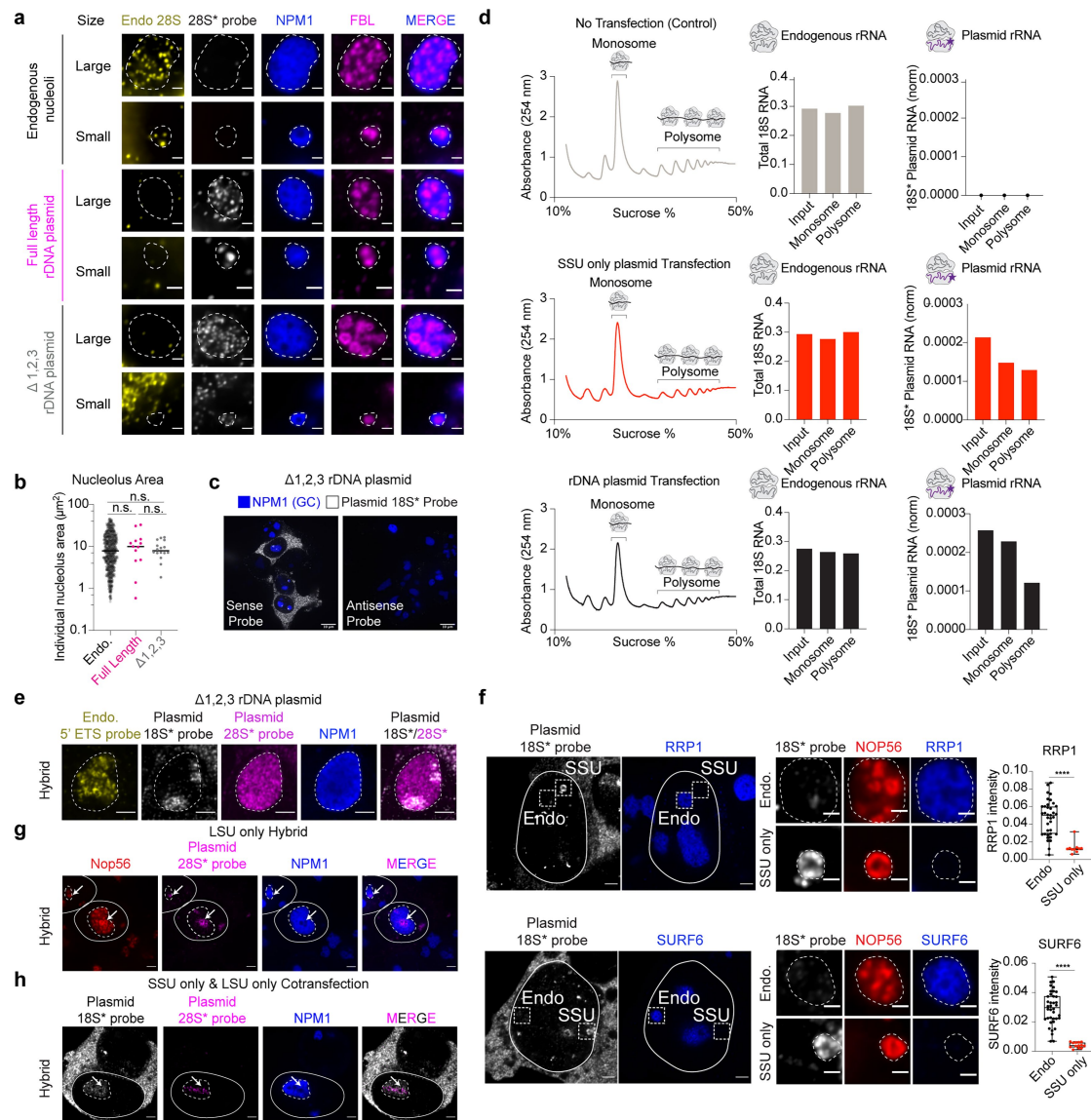
Extended Data Fig. 8 | Characterizing the synthetic nucleoli and mature rRNA produced from the engineered rDNA system. a, Size comparison of endogenous and synthetic nucleoli (IF for FBL and NPM1 for DFC and GC, respectively) from endogenous, full-length plasmid, and Δ1,2,3 plasmid rDNA. Scale bar = 1 μm. **b**, Quantification of nucleolar area from a. Nucleolar size is not significantly different between any two conditions (two-tailed t-test, endogenous (n = 829), full length rDNA (n = 13), and Δ1,2,3 rDNA (n = 16)). **c**, Strand-specific RNA FISH (sense and antisense probes) demonstrate that FISH signal is specific to RNA (not DNA) in cells transfected with Δ1,2,3 rDNA plasmid (GC, mTagBFP2-NPM1). Scale bar = 10 μm. **d**, Left, polysome profiling of cells transfected with SSU-only or rDNA plasmids, compared to untransfected controls. Right, RT-qPCR quantification of plasmid-derived rRNA (18S*) and total 18S rRNA in input, monosome, and polysome fractions. **e**, Representative image of a "Hybrid" nucleolus containing endogenous (endo.) 5′ ETS pre-rRNA (yellow) and plasmid-derived rRNAs: 18S* (white) and 28S* (magenta). Scale bar

= 3 μm. **f**, Localization of two GC markers, RRP1 and SURF6 (both detected by IF, blue), in endogenous and SSU-only nucleoli (DFC, NOP56-mCherry). Right, quantification of RRP1 (endogenous: n = 37; SSU-only: n = 10) and SURF6 (endogenous: n = 38; SSU-only: n = 13) intensity. Scale bars = 3 μm (left), = 1 μm (right). Box plots show medians (lines), boxes (25th-75th percentiles), whiskers (min-max). *** P-value < 0.0001 (two-tailed Mann-Whitney test). **g-h**, g, Cells transfected with LSU-only plasmid (28S* FISH, magenta) form a "hybrid" with endogenous nucleoli (endo. 5′ ETS, yellow). Note the absence of cytoplasmic 28S* signal despite the colocalization between plasmid-expressed 28S* rRNA in endogenous nucleoli. h, Co-transfection of SSU-only (18S* FISH, white) and LSU-only (28S* FISH, magenta) plasmids to test whether co-localization between plasmid-expressed 18S* and 28S* rRNA is sufficient to rescue cytoplasmic 28S* export. Dotted lines outline nucleoli; solid lines outline nuclei. Arrows indicate colocalization events. DFC: NOP56-mCherry; GC: mTagBFP2-NPM1. Scale bar = 3 μm. HEK293T cells used in all panels.
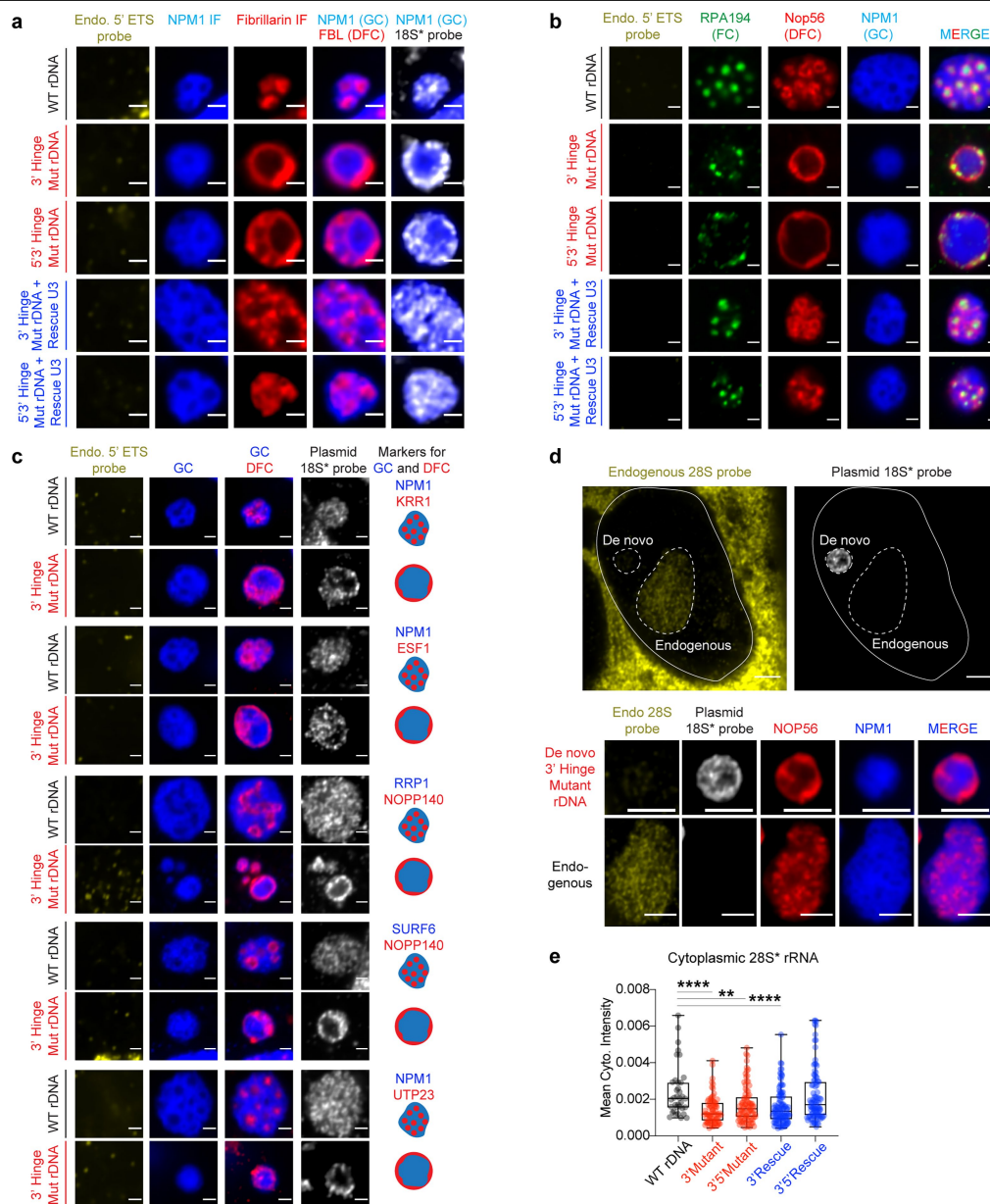
Extended Data Fig. 9 | Nucleolar morphology changes for engineered rDNA plasmids with impaired U3 snoRNA base pairing. a, De novo nucleolar morphology in HEK293T cells transfected with mutations with rDNA plasmids containing mutations in the 3′ or 5′ hinge U3 snoRNA binding sites within the 5′ ETS, along with compensatory U3 snoRNA mutations. Nucleoli were labelled by IF for DFC (FBL, red), GC (NPM1, blue), and RNA FISH for plasmid-derived 18S* rRNA (white) and endogenous 5′ ETS (yellow). **b**, De novo nucleoli labelled with markers for three nucleolar layers (FC, RPA194 IF; DFC, NOP56-mCherry; GC, mTagBFP2-NPM1) in HEK293T cells transfected with the same plasmids as in a. **c**, Validation of inverted nucleolar morphology using immunofluorescence staining for additional markers of the DFC (KRR1, ESF1, NOPP140 and UTP23)

and GC (NPM1, RRP1, SURF6) in HEK293T cells. **d**, Top, HEK293T cell transfected with 3′ hinge mutant rDNA plasmid. Endogenous and de novo nucleoli can be distinguished using RNA FISH for endogenous 28S rRNA (endo 28S, yellow) and plasmid-derived 18S* rRNA (white). Bottom, zoom in on the endogenous and de novo nucleoli labelled with DFC (NOP56-mCherry, red) and GC (mTagBFP2-NPM1, blue) markers. **e**, Quantification of cytoplasmic 28S* plasmid rRNA signal from cells transfected with the indicated plasmids (corresponding to Fig. 4b). n = 36, 74, 84, 103, 92 cells. ** p-value = 0.0026; **** p-value < 0.0001 (two-tailed Mann-Whitney test). Box plots show medians (lines), boxes (25th-75th percentiles), whiskers (min-max). Scale bars = 1 μm (a-c), 3 μm (d).
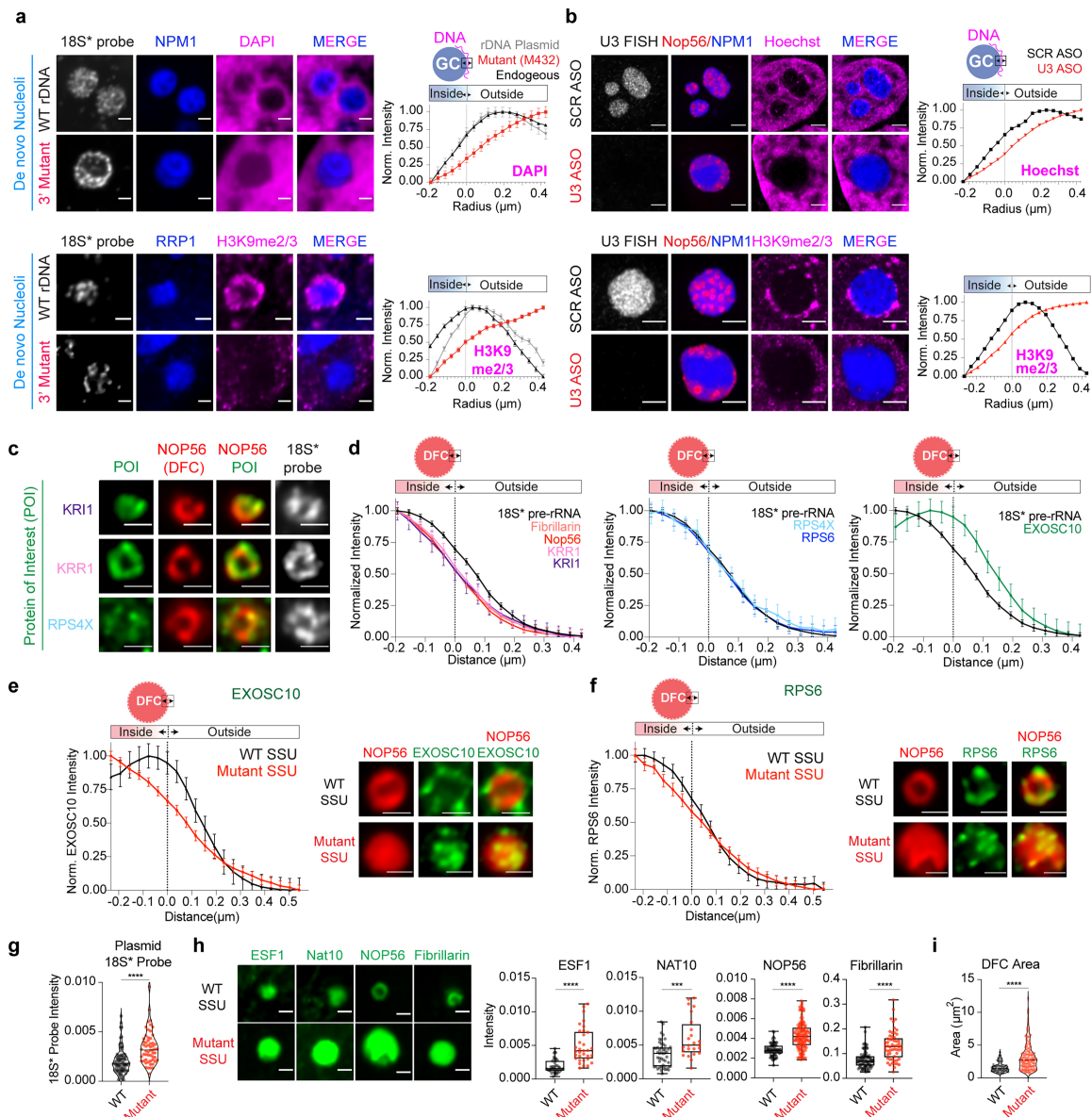
Extended Data Fig. 10 | Characterization of perinucleolar chromatin upon inversion and rRNA outflux defects in mutant SSU-only nucleoli. a, Staining of heterochromatin (H3K9me2/3; GC marked by RRP1 IF) and chromatin (DAPI; GC marked by NPM1 IF) surrounding de novo nucleoli from wild-type (WT) or 3′ hinge mutant rDNA-transfected cells. Right, radial distribution of (hetero) chromatin signal around the GC boundary (dashed line = 0 μm) in endogenous nucleoli, WT de novo nucleoli, or 3′ hinge mutant de novo nucleoli. DAPI: n = 1779 (Endogenous), 15 (rDNA plasmid), 15 (3′ hinge Mutant); H3K9me2/3 n = 37 (Endogenous), 33 (rDNA plasmid), 30 (3′ hinge Mutant). **b**, Radial distribution of chromatin (Hoechst) or heterochromatin (H3K9me2/3) around endogenous nucleoli in scramble (SCR) or U3 ASO treated cells. Hoechst: n = 1958 (SCR), 901 (U3 ASO), H3K9me2/3: n = 2556 (SCR), 562 (U3 ASO). **c-f**, Visualization of SSU processing factors and ribosomal proteins (proteins of interest (POIs), green) in WT and mutant SSU-only nucleoli demarcated by NOP56-mCherry. **c-d**, Radial distribution of KRI1 (IF, n = 17), KRR1 (IF, n = 26) and

RPS4X-Halotag (n = 15) around the DFC boundary of WT SSU-only nucleoli. See Fig. 4g for images of the other quantified POIs. **e-f**, Radial distribution of EXOSC10 and RPS6 in WT and mutant SSU-only nucleoli. EXOSC10: n = 12 (WT), 38 (Mutant), RPS6: n = 21 (WT), 47 (Mutant). **g**, Mean nucleolar 18S* rRNA intensity in WT (n = 87) and mutant (n = 57) SSU-only nucleoli. **** P-value < 0.0001. **h**, Mean nucleolar intensity of early SSU processing factors ESF1, NAT10, and FBL (IF) and NOP56-mCherry in WT and Mutant SSU-only nucleoli. WT: n = 38, 49, 74, 87; Mutant: n = 33, 24, 164, 57 for ESF1, Nat10, Nop56, and Fib. *** P-value = 0.0005; **** P-value < 0.0001. **i**, DFC area (NOP56-mCherry) in WT (n = 74) and mutant (n = 164) SSU-only nucleoli. **** P-value < 0.0001. All scale bars = 1 μm. Violin plots are centred by median. Box plots show medians (lines), boxes (25th-75th percentiles), whiskers (min-max). Statistical tests are two-tailed Mann-Whitney tests. All error bars are s.e.m. HEK293T cells are used except for b (MCF10A).

nature portfolio

Corresponding author(s): Clifford Brangwynne, Sebastian Klinge, Denis Lafontaine

Last updated by author(s): 4/29/2025

Reporting Summary

Nature Portfolio wishes to improve the reproducibility of the work that we publish. This form provides structure for consistency and transparency in reporting. For further information on Nature Portfolio policies, see our Editorial Policies and the Editorial Policy Checklist.

Please do not complete any field with "not applicable" or n/a. Refer to the help text for what text to use if an item is not relevant to your study.
For final submission: please carefully check your responses for accuracy; you will not be able to make changes later.

Statistics

For all statistical analyses, confirm that the following items are present in the figure legend, table legend, main text, or Methods section.

n/a	Confirmed	
☐	☒	The exact sample size (*n*) for each experimental group/condition, given as a discrete number and unit of measurement
☐	☒	A statement on whether measurements were taken from distinct samples or whether the same sample was measured repeatedly
☐	☒	The statistical test(s) used AND whether they are one- or two-sided *Only common tests should be described solely by name; describe more complex techniques in the Methods section.*
☒	☐	A description of all covariates tested
☐	☒	A description of any assumptions or corrections, such as tests of normality and adjustment for multiple comparisons
☐	☒	A full description of the statistical parameters including central tendency (e.g. means) or other basic estimates (e.g. regression coefficient) AND variation (e.g. standard deviation) or associated estimates of uncertainty (e.g. confidence intervals)
☐	☒	For null hypothesis testing, the test statistic (e.g. *F*, *t*, *r*) with confidence intervals, effect sizes, degrees of freedom and *P* value noted *Give P values as exact values whenever suitable.*
☒	☐	For Bayesian analysis, information on the choice of priors and Markov chain Monte Carlo settings
☒	☐	For hierarchical and complex designs, identification of the appropriate level for tests and full reporting of outcomes
☐	☒	Estimates of effect sizes (e.g. Cohen's *d*, Pearson's *r*), indicating how they were calculated

Our web collection on statistics for biologists contains articles on many of the points above.

Software and code

Policy information about availability of computer code

Data collection	Images were acquired with the NIS-Elements AR (Nikon, 5.42.02) with Nikon CSU-W1 SoRa spinning disk confocal system. Denoising (when applicable) was performed using the built-in NIS-Elements Denoise.ai module.
Data analysis	All statistical analyses and graphing were performed using Graphpad Prism 10 and Microsoft Excel. For creating example images, imageJ (1.53f) was used. All codes and pipelines used for this study are provided in the following repositories: https://github.com/SoftLivingMatter/image-analysis-quinodoz-jiang-2024 (https://zenodo.org/records/14908468) https://github.com/SoftLivingMatter/snakemake-cellprofiler (https://zenodo.org/records/14908470) https://github.com/SoftLivingMatter/5eU-seq-pipelines (https://zenodo.org/records/14908466) Example images & analysis notebooks: https://doi.org/10.5281/zenodo.14910509

For manuscripts utilizing custom algorithms or software that are central to the research but not yet described in published literature, software must be made available to editors and reviewers. We strongly encourage code deposition in a community repository (e.g. GitHub). See the Nature Portfolio guidelines for submitting code & software for further information.

Data

Policy information about [availability of data](#)

All manuscripts must include a [data availability statement](#). This statement should provide the following information, where applicable:
- Accession codes, unique identifiers, or web links for publicly available datasets
- A description of any restrictions on data availability
- For clinical datasets or third party data, please ensure that the statement adheres to our [policy](#)

> All data supporting these findings are available in the manuscript and associated source data. All genomics data are available at the Gene Expression Omnibus (GEO) with accessions: GSE296080 and GSE296162.

Research involving human participants, their data, or biological material

Policy information about studies with [human participants or human data](#). See also policy information about [sex, gender (identity/presentation), and sexual orientation](#) and [race, ethnicity and racism](#).

Reporting on sex and gender	n.a.
Reporting on race, ethnicity, or other socially relevant groupings	n.a.
Population characteristics	n.a.
Recruitment	n.a.
Ethics oversight	n.a.

Note that full information on the approval of the study protocol must also be provided in the manuscript.

Field-specific reporting

Please select the one below that is the best fit for your research. If you are not sure, read the appropriate sections before making your selection.

☒ Life sciences   ☐ Behavioural & social sciences   ☐ Ecological, evolutionary & environmental sciences

For a reference copy of the document with all sections, see [nature.com/documents/nr-reporting-summary-flat.pdf](#)

Life sciences study design

All studies must disclose on these points even when the disclosure is negative.

Sample size	Sample sizes were not predetermined. For imaging experiments, sample size were chosen to make sure a representative population were captured. For sequencing experiments, number of replicates, time points, and cells were determined based on technical requirements that ensure reproducibility and maintain high data quality.
Data exclusions	For imaging, cells that are out of focus are excluded. For 5eU sequencing, samples that failed quality control (such as failed click reactions, streptavidin captures, or library amplifications) were excluded from downstream analysis.
Replication	Microscopy imaging, western blotting, and RT-qPCR were repeated independently for at least three times with similar results. 5eU-sequencing were conducted with 1 or 2 replicates per time point. P-values and number of observations (n) are provided in figure legends. All attempts at replication were successful.
Randomization	For all experiments, cells were randomized such that within a biological or technical replicate all cells were analyzed equally with no sub-sampling.
Blinding	Blinding not performed due to standardized data collection procedures. Imaging and sequencing analyses were performed using automated pipelines whenever possible to minimize observer biases.

Reporting for specific materials, systems and methods

We require information from authors about some types of materials, experimental systems and methods used in many studies. Here, indicate whether each material, system or method listed is relevant to your study. If you are not sure if a list item applies to your research, read the appropriate section before selecting a response.

Materials & experimental systems

n/a	Involved in the study
☐	☒ Antibodies
☐	☒ Eukaryotic cell lines
☒	☐ Palaeontology and archaeology
☒	☐ Animals and other organisms
☒	☐ Clinical data
☒	☐ Dual use research of concern
☒	☐ Plants

Methods

n/a	Involved in the study
☒	☐ ChIP-seq
☒	☐ Flow cytometry
☒	☐ MRI-based neuroimaging

Antibodies

Antibodies used

1. Antibodies for Immunofluresence
Antibody Name supplier name catalog number -working dilution
RPA194 Santa Cruz sc-48385 AF488 1:200
RPA194-488 Santa Cruz sc-48385 1:200
NPM1-488 Thermo Fisher MA3-25200-A488 1:400
Fibrillarin Abcam ab5821 1:300
Fibrillarin-568 Abcam ab202540 1:300
RRP1B Sigma HPA017893 1:100
SURF6 Thermo Fisher PA5-54841 1:100
Nat10 Thermofisher 13365-1-AP 1:100
ESF1 proteinTech 23496-1-AP 1:100
EXOSC10 Sigma-Aldrich HPA028484 1:100
Nucleolin ThermoFisher 39-6400 1:100
DDX21 Sigma-Aldrich HPA036593 1:100
KRI1 proteintech 16243-1-AP 1:100
KRR1 Assay Genie CAB4487-20 1:100
H3K9me2/3 Cell Signaling Technology 5327T 1:100
UTP23 proteinTech 15950-1-AP 1:100
NOPP140 Santa Cruz Biotechnology sc-374033 1:200
Goat anti-Mouse IgG (H+L) Cross-Adsorbed Secondary Antibody, Alexa Fluor™ 568 Thermofisher A-11004 1:1000
Goat anti-Rabbit IgG (H+L) Cross-Adsorbed Secondary Antibody, Alexa Fluor™ 488 Thermofisher A-11008 1:1000
Goat anti-Rabbit IgG (H+L) Cross-Adsorbed Secondary Antibody, Alexa Fluor™ 405 Thermofisher A-31556 1:1000

2. Antibodies for Western blotting
Antibody Name -Source -Identifier-Working dilution
Fibrillarin Abcam ab5821 1:1000
β-Actin Antibody #4967 Cell Signalling 4967S 1:1000
NPM1 Monoclonal Antibody (4TOU-1B2) Thermofisher MA3-086 1:1000
Peroxidase AffiniPure™ Goat Anti-Rabbit IgG (H+L) Jackson ImmunoResearch 111-035-144 1:10, 000
Peroxidase AffiniPure™ Goat Anti-Mouse IgG (H+L) Jackson ImmunoResearch 115-035-062 1:10, 000

Validation

All antibodies used for immunofluorescence (IF) are validated by confirming that the intracellular localization matches the reported cellular localization. Western blotting (WB) antibodies are validated by the molecular weight of the band detected and the reduced intensity upon knockdown for fibrillarin. In addition, antibodies were validated by the manufacturer: e.g.,ESF1 (proteinTech 23496-1-A) has been tested in mouse heart tissue for WB and MCF-7 cells for IF and it has tested reactivity against mouse and human. Fibrillarin (Abcam ab5821 and ab202540) has been tested for WB and IF in human, mouse and Drosophila melanogaster. RRP1B (Sigma HPA017893), SURF6 (Thermo Fisher PA5-54841), Nat10 (Thermofisher 13365-1-AP), DDX21 (Sigma-Aldrich HPA036593), NPM1-488 (Thermo Fisher MA3-25200-A488), Nucleolin (ThermoFisher 39-6400), RRP1B (Sigma HPA017893), and RPA194 (Santa Cruz sc-48385) have been tested in IF with localization to nucleoli.

Eukaryotic cell lines

Policy information about cell lines and Sex and Gender in Research

Cell line source(s)

The following cell lines are used in this study: MCF10A (gift from Yibin Kang, ATCC, female), HEK293T (ATCC, female), HCT116 (gift from Yibin Kang, ATCC, male) and MCF7 (gift from Yibin Kang, ATCC, female). All cell lines were derived from human participants

Authentication

All the gifted cell lines were validated by STR profiling with > 90% match. Vendors of each of the commercially-available cell lines (ATCC) provide further information about the authentication of cells on their website.

Mycoplasma contamination

All cell lines used in this study tested negative for mycoplasma contaminiation.

Commonly misidentified lines
(See ICLAC register)

No cell lines used in this study were among the commonly misidentified lines

Plants

Seed stocks	n.a.
Novel plant genotypes	n.a.
Authentication	n.a.

Mapping and engineering RNA-driven architecture of the multiphase nucleolus

Supplementary Figure 1: Unprocessed gel source images for western blotting and electrophoretic gels
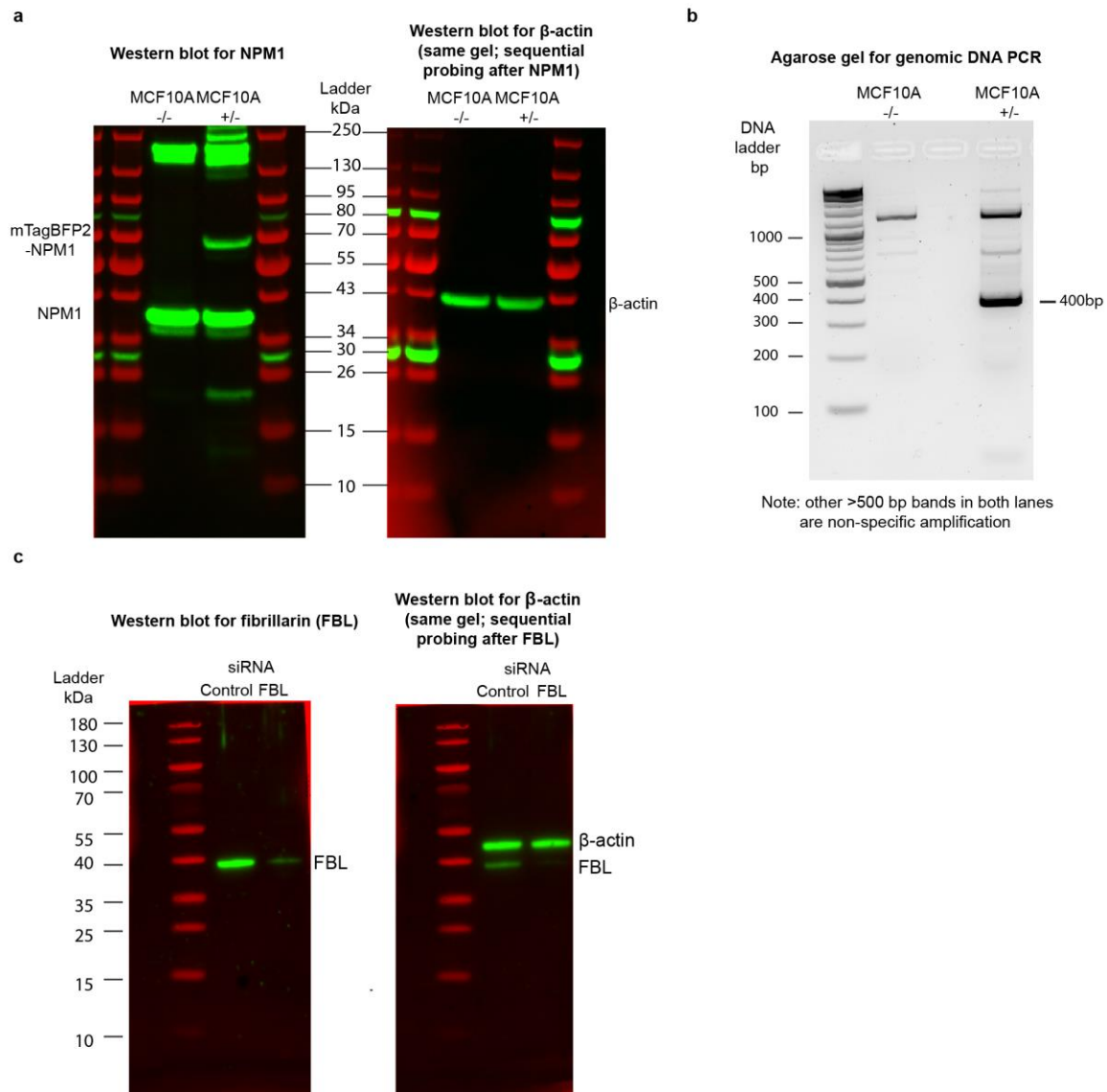
a, Gel source image for ED Fig. 2g. Western blot for endogenously-tagged MCF10A cells. Sequential probing for NPM1 (left) and β-actin (right) was performed from the same gel. MCF10A -/-: parental line with no tagging. MCF10A +/-: single copy tagged mTagBFP2-NPM1 cell line. **b**, Source image for ED Fig. 2f. Gel electrophoresis for genomic DNA PCR of samples described in a. **c**, Gel source image for ED Fig. 5l. Western blot for validating FBL knockdown (Control siRNA vs. FBL siRNA). Sequential probing for FBL (left) and β-actin (right) were performed from the same gel.

Supplemental Note 1: Kinetic model of transcription and processing of nascent ribosomal RNA

In this Supplementary Note, we present a chemical kinetics model to describe the transcription and processing of pre-ribosomal RNA (pre-rRNA) in the 5eU pulse-chase experiments. Fitting the model to the sequencing and imaging data allows us to extract effective reaction rates of transcription and processing, which can be used to infer steady-state properties such as the relative abundance of rRNA precursors.

A. Kinetic model for 5eU incorporation into pre-rRNA

In the 5eU pulse-chase experiments, the total amount of pre-rRNA can be measured by imaging the total 5eU intensity in the nucleus (Fig. 1). We model the production of 5eU-labeled pre-rRNA with a two-step process: first, 5eU needs to be uptaken by the cell into the nucleus; second, the available 5eU is incorporated into pre-rRNA during transcription. Both steps are described by linear kinetics:

$$\frac{\mathrm{d}c_0}{\mathrm{d}t} = k_0 \Theta(-t)\Theta(t + t_{\mathrm{pulse}}) - k_1 c_0, \tag{1}$$

$$\frac{\mathrm{d}c_1}{\mathrm{d}t} = k_1 c_0, \tag{2}$$

where c_0 is the amount of nuclear 5eU available for transcription, and c_1 is the amount of 5eU in pre-rRNA. k_0 and k_1 are the reaction rates of 5eU uptake and transcription, respectively. The Heaviside step functions $\Theta(-t)$ and $\Theta(t + t_{\mathrm{pulse}})$ describe the pulse of 5eU, during $t \in (-_{\mathrm{pulse}}, 0)$.

The model can be solved analytically to obtain the total 5eU signal in the pre-rRNA:

$$c_1(t) = \begin{cases} 0, & t < -t_{\mathrm{pulse}}, \\ \frac{k_0}{k_1}\left(-1 + e^{-k_1(t + t_{\mathrm{pulse}})} + k_1(t + t_{\mathrm{pulse}})\right), & -t_{\mathrm{pulse}} \le t < 0, \\ \frac{k_0}{k_1}\left(k_1 t_{\mathrm{pulse}} - e^{-k_1 t} + e^{-k_1(t + t_{\mathrm{pulse}})}\right), & t \ge 0. \end{cases} \tag{3}$$

Eq. (4) agrees well with the total 5eU signal measured by imaging, with fitting parameters $k_0 = 0.052 \pm 0.006$ min^{-1} and $k_1 = 0.051 \pm 0.026$ min^{-1} (Fig. 1). The fit allows us to extract the rate of transcription (of rRNA labeled by 5eU) $k_0 c_0$, with c_0 given by

$$c_0(t) = \begin{cases} 0, & t < -t_{\mathrm{pulse}}, \\ \frac{k_0}{k_1}\left(1 - e^{-k_1(t + t_{\mathrm{pulse}})}\right), & -t_{\mathrm{pulse}} \le t < 0, \\ \frac{k_0}{k_1}e^{-k_1 t}\left(1 - e^{-k_1 t_{\mathrm{pulse}}}\right), & t \ge 0. \end{cases} \tag{4}$$

B. Kinetic model for rRNA processing

Next, we consider the kinetics of rRNA processing as measured by sequencing in the pulse-chase experiments. For simplicity, we assume the processes to be limited by reaction rather than diffusion, which allows ignoring spatial degrees of freedom. We model each cleavage step as a first order reaction with rate k_i, with $i = 2, 3, 4, 5$. k_2 corresponds to the cleavage of junctions 01 and 02, k_3 junctions 1 and 2, k_4 junction 3', and k_5 junction 4'. The abundance of individual pre-rRNA species is represented by c_i, with i labeling the next cleavage step. The kinetic model is given by

$$\frac{\mathrm{d}c_2}{\mathrm{d}t} = k_1 c_0 - k_2 c_2, \quad \frac{\mathrm{d}c_3}{\mathrm{d}t} = k_2 c_2 - k_3 c_3, \tag{5}$$

$$\frac{\mathrm{d}c_4}{\mathrm{d}t} = k_3 c_3 - k_4 c_4, \quad \frac{\mathrm{d}c_5}{\mathrm{d}t} = k_4 c_4 - k_5 c_5, \tag{6}$$

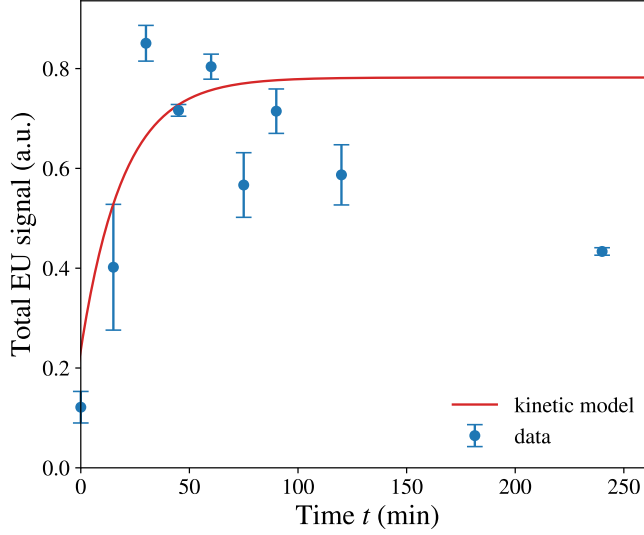$$\frac{\mathrm{d}c_6}{\mathrm{d}t} = k_5 c_5, \tag{7}$$

FIG. 1. Fitting the total 5eU signal in the nucleus to the model [Eq. (4)]. The fit only used data in the first two hours after the pulse.

where $c_1 = \sum_{i=2}^{5} c_i$ is the total amount of pre-rRNA. We fit the model to the cleavage fraction of each junction as measured by 5eU-sequencing:

$$f_{01} = \frac{c_3}{c_2 + c_3}, \quad f_{02} = 1 - \frac{c_2}{c_1}, \quad f_{1,2} = 1 - \frac{c_2 + c_3}{c_1}, \quad f_{3'} = 1 - \frac{c_2 + c_3 + c_4}{c_1} = \frac{c_5 + c_6}{c_1}, \quad f_{4'} = \frac{c_6}{c_1}, \tag{8}$$

where f_i is the fraction of junction i cleaved as measured by sequencing. Junctions 1 and 2 are averaged to obtain $f_{1/2}$. Junction 3' is not used in the fit. The definition of f_{01} is slightly different from all the other fractions because the cleavage of junction 01 can no longer be detected once junction 1 is cut, while the cleavage of junction 2 is detectable in all the later species.

The kinetic model provides an excellent fit to the data (Fig. 2). The best fit parameters are $k_2 = 0.061$ min^{-1}, $k_3 = 0.035$ min^{-1}, $k_4 = 0.046$ min^{-1}, and $k_5 = 0.046$ min^{-1}. This also allows us to estimate the relative abundance of individual pre- rRNA species at steady state:

$$c_2 : c_3 : c_4 : c_5 \sim k_2^{-1} : k_3^{-1} : k_4^{-1} : k_5^{-1} = 19\% : 32\% : 25\% : 25\%. \tag{9}$$

The abundance of 18S is slightly different since its processing does not involve cutting junctions 3' and 4'. We estimate that it is exported at rate $\tilde{k}_4 \sim 30$ min^{-1} after the cleavage of junctions 1 and 2. The relative abundance of 18S is then given by

$$\tilde{c}_2 : \tilde{c}_3 : \tilde{c}_4 \sim k_2^{-1} : k_3^{-1} : \tilde{k}_4^{-1} = 22\% : 38\% : 40\%. \tag{10}$$

This provides an estimate of the fraction of processed versus unprocessed 18S in the multiphase reaction-diffusion model (Figure 5 in the main text).

C. Deconvolving the radial distribution of pre-rRNA

The kinetic model allows us to deconvolve the pre-rRNA distribution measured by 5eU imaging into the distribution of different pre-rRNA species. Let $\phi_i(r)$ be the steady-state radial distribution of pre-rRNA species i (e.g. i is a particular cleavage state), which is normalized by $\int_0^\infty \phi_i(r) 4\pi r^2 dr = 1$. Assuming that pre-rRNA processing is reaction limited (i.e. diffusion within each phase is much faster than cleavage), the radial distribution of the total pre-rRNA (since 5eU-imaging labels all the pre-rRNA species) $\phi(r, t)$ is given by a linear combination of the individual species:

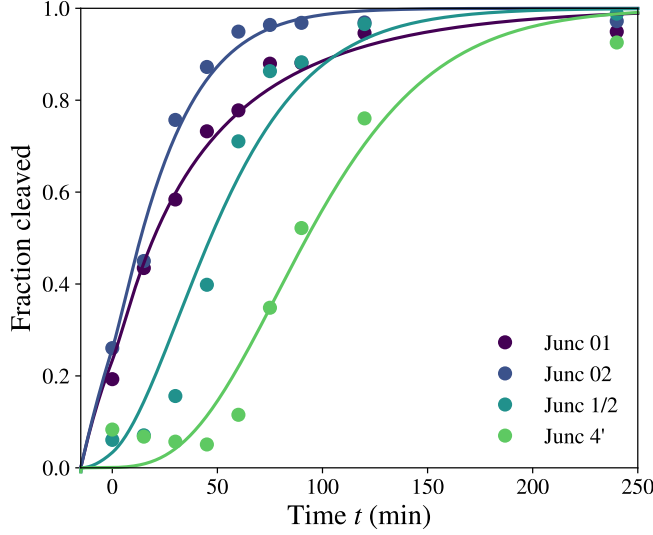$$\phi(r, t) = \frac{\sum_i c_i(t) \phi_i(r)}{\sum_i c_i(t)} = \sum_i \gamma_i(t) \phi_i(r), \tag{11}$$

2

FIG. 2. The kinetic model [Eq. (8)] captures the cleavage fraction of pre-rRNA as measured by 5eU-sequencing.

where $\gamma_i(t) = c_i(t)/\sum_i c_i(t)$ is the fraction of pre-rRNA species i at time t. $\phi(r, t)$ is normalized by $\int_0^\infty \phi(r, t) 4\pi r^2 dr = 1$ for all t.

Thus, the steady-state distribution of individual species can be obtained by solving a constrained non-negative least squares problem:

$$\min_{\phi_i(r)} \sum_t \int_0^\infty \left(\phi(r, t) - \sum_i \gamma_i(t)\phi_i(r) \right)^2 4\pi r^2 dr, \tag{12}$$

subject to $\int_0^\infty \phi_i(r) 4\pi r^2 dr = 1$ and $\phi_i(r) \geq 0$ for i running over all the pre-rRNA species.

Here, we divide rRNA into early (ϕ_2), middle (ϕ_3), late ($\phi_4 + \phi_5$), and cytoplasmic (ϕ_6) species.

The relative abundance $\gamma_i(t)$ is predicted by the kinetic model (Fig. 3A). $\phi(r, t)$ is measured by 5eU imaging(Fig. 3B). Solving the optimization problem gives the radial distribution function $\phi_i(r)$ for each species ii (Fig. 3C) and probability distribution function $4\pi r^2 \phi_i(r)$ (Fig. 3D), which demonstrate that pre-rRNA processing correlates with its outward movement. A similar deconvolution can be done to the RNA FISH measurements. The normalized FISH signal for junction i is given by

$$y_i(r) = \frac{\sum j \leq i c_j^{\mathrm{ss}} \phi_j(r)}{\sum_{j \leq i} c_j^{\mathrm{ss}}}, \tag{13}$$

where c_j^{ss} is the steady-state abundance of pre-rRNA species j. Solving Eq. (13) gives the spatial distribution of intermediates predicted by FISH, which can be compared with that from 5eU-seq and imaging (Fig. 4).
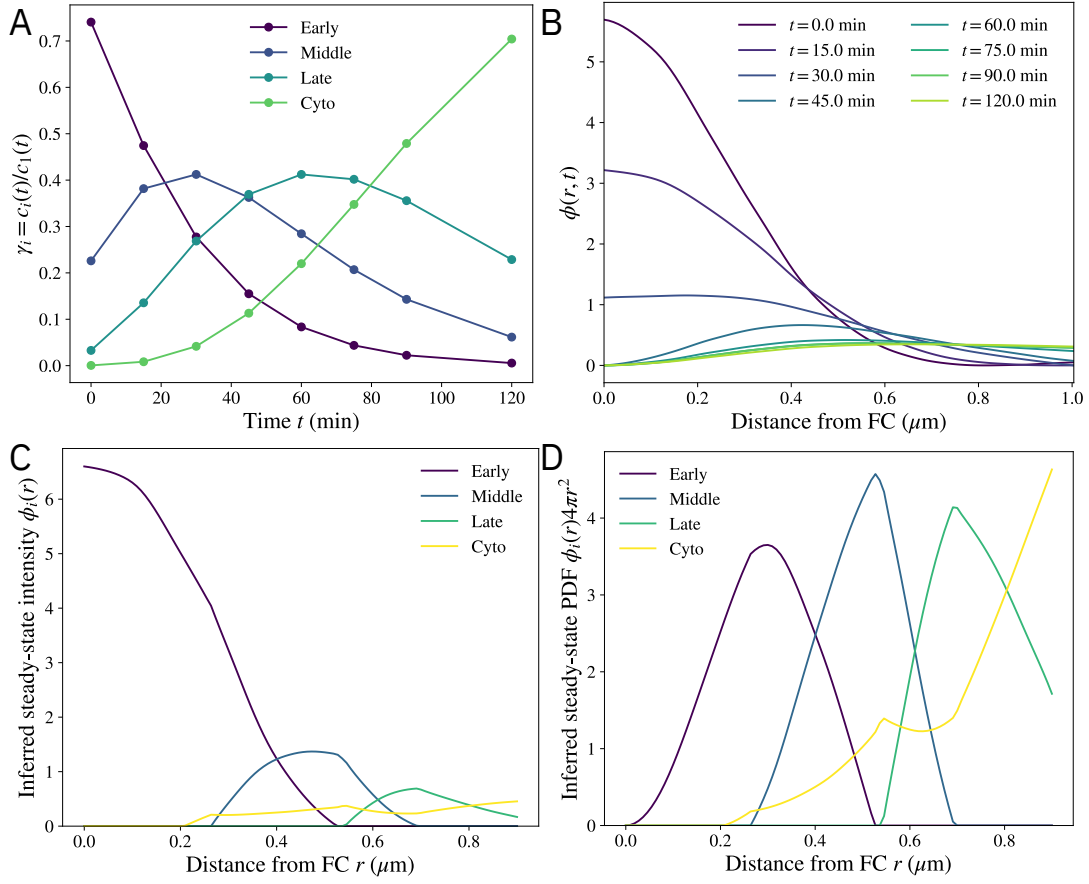
3

FIG. 3. Deconvolving the radial distribution of pre-rRNA. (A) rRNA abundance $\gamma_i(t)$ as a function of time, obtained from the kinetic model. (B) the radial distribution of pre-rRNA at different times, obtained by normalizing the 5eU imaging data. (C—D) the radial distribution function $\phi_i(r)$ (C) and probability distribution function $4\pi r^2 \phi_i(r)$ (D) of individual rRNA species, inferred by solving the optimization problem [Eq. (12)].
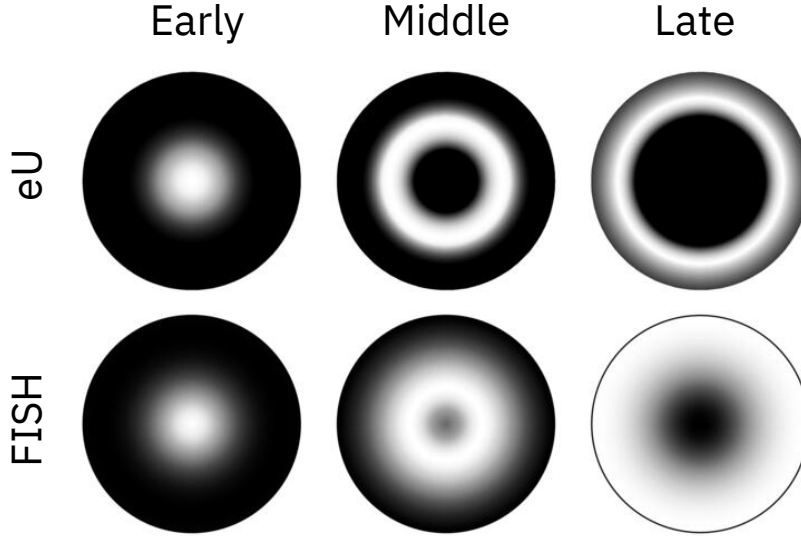

FIG. 4. The radial distribution of early, middle, and late pre-rRNA species as inferred from 5eU-imaging (top) and FISH (bottom). For 5eU-imaging, the distribution is inferred by solving the optimization problem Eq. (12). For FISH, the spatial distribution is obtained by solving Eq. (13) for $\phi_i(r)$. The radius of the circles is 0.9μm.

A. Thermodynamic model

Given the experimental evidence of nucleolar morphology changes as a result of the perturbations of rRNA composition, we seek to develop a model that captures the change in the surface tensions between nucleolar phases as well as the changes in the partitioning of rRNA in the different phases upon rRNA perturbations. We first consider the Flory-Huggins model, a well-established thermodynamic model that describes polymer phase separation. To capture the essential physics, the system consists of the nucleolar species [DFC, GC, and nucleoplasm (NP)], and the rRNA species [SSU before 5'ETS cleavage, i.e. unprocessed 18S (u18S), SSU after 5'ETS cleavage, i.e. processed 18S (p18S), and 28S]. We denote the set of nucleolar species and nucleoplasm as $N = \{DFC, GC, NP\}$ and the set of rRNA species as $R = \{u18S, p18S, 28S\}$. The free energy density of the mixture g follows

$$\frac{g}{k_B T} = \sum_i \quad \frac{1}{N_i} \phi_i \, ln \, \phi_i + \frac{1}{2} \sum_{ij} \quad \chi_{ij} \phi_i \phi_j, \qquad (1)$$

where k_B is the Boltzmann constant, T is the temperature; N_i and ϕ_i are the degree of polymerization and the volume fraction of component i, respectively. The volume fractions satisfy the normalization condition $\sum_i \quad \phi_i = 1$. The summation indices i and j iterate over all chemical components mentioned above. For simplicity, we set all degrees of polymerization to be equal to N_0. In the free energy density in the above Eq. (1), the first and second terms correspond to the entropy and enthalpy of mixing, respectively. χ_{ij} is the interaction parameter between components i and j – a higher value means stronger repulsion between the two, and $\chi_{ij} = \chi_{ji}$ ($i \neq j$), $\chi_{ii} = 0$. This determines the phase separation between nucleolar compartments as well as the affinity of rRNA to each nucleolar phase. For example, if $\chi_{GC,28S} < \chi_{NP,28S}$, then 28S is more enriched in the GC compared to the nucleoplasm. When χ_{ij} is sufficiently high, the system undergoes phase separation into a phase that is rich in component i and another coexisting phase that is rich in component j. Following the Cahn-Hilliard theory of phase separation, the free energy of such a spatially heterogeneous system where phase separation occurs is

$$G = c_0 \int \quad \left(g + \frac{1}{2} \kappa \sum_i \quad |\nabla \phi_i|^2 \right) dV, \qquad (2)$$

where the gradient term corresponds to the energy of interaction at the interface, and c_0 is the number concentration of monomers. The phase equilibrium condition corresponds to the minimization of the free energy subject to the mass conservation of all chemical components. This is equivalent to a uniform chemical potential μ_i, which is defined to be the variational derivative of the free energy with respect to the volume fraction,

$$\mu_i \equiv \frac{1}{c_0} \frac{\delta G}{\delta \phi_i} = {\mu_i}^0. \qquad (3)$$

Suppose that phases α and β form a flat interface in an infinitely large domain, the surface tension between the two phases $\gamma_{\alpha\beta}$ is defined to be the excess energy associated with the interface joining the two bulk phases,

$$\gamma_{\alpha\beta} = c_0 \int_{-\infty}^{\infty} \quad \left(g + \frac{1}{2} \kappa \sum_i \quad |\nabla \phi_i|^2 - \sum_i \quad {\mu_i}^0 (\phi_i - {\phi_i}^{(\alpha)}) \right) dx, \quad (4)$$

where x is in the direction normal to the interface, ϕ_i is the volume fraction at equilibrium, ${\phi_i}^{(\alpha)}$ is the volume fraction in phase α away from the interface.

It is known that when χ_{ij} is large, the surface tension between the two phases is approximately proportional to χ_{ij} [1,2]. However, it is unclear how the presence and partitioning of non-phase-separating species such as rRNA, affects the surface tension. Therefore, we numerically calculate the surface tension by performing a phase field simulation that finds the equilibrium state. Specifically, we perform one-dimensional simulations with periodic boundary conditions and find an equilibrium state where three phases, which are rich in DFC, GC, and NP, separately, coexist. We then calculate the integral in Eq. (4) between all bulk phases to find the surface tensions.

In the following text, we use $\gamma_{DFC,GC}$ to denote the surface tension between the DFC and GC phases, and similarly $\gamma_{DFC,NP}, \gamma_{GC,NP}$. Under normal conditions, the DFC phase is surrounded by the GC phase, indicating that the surface tensions satisfy inequality $\gamma^{(1)}{}_{DFC,NP} \geq \gamma^{(1)}{}_{DFC,GC} + \gamma^{(1)}{}_{GC,NP}$, where the superscript (1) indicates a system (1) where the concentration of processed 18S is high, unprocessed 18S is low, and that of the 28S is normal. Under U3 ASO treatment and treatment with mutant plasmids, the GC phase is surrounded by the DFC phase, indicating that $\gamma^{(2)}{}_{GC,NP} \geq \gamma^{(2)}{}_{DFC,GC} + \gamma^{(2)}{}_{DFC,NP}$, where the superscript (2) indicates a system (2) where the concentration of processed 18S is low, unprocessed 18S is high, and that of the 28S is normal, and the average volume fraction of DFC and GC are equal to that of the system (1).

Therefore, in order to find a set of parameters χ_{ij} to recapitulate these two morphologies, we perform the following optimization

$$\min_{\chi_{ij}} \Gamma(\gamma^{(1)}{}_{DFC,GC} + \gamma^{(1)}{}_{GC,NP} - \gamma^{(1)}{}_{DFC,NP}) + (1 - \Gamma)(\gamma^{(2)}{}_{DFC,GC} + \gamma^{(2)}{}_{DFC,NP} - \gamma^{(2)}{}_{GC,NP}), \quad (5)$$

where $0 < \Gamma < 1$ is a weighting factor. In the optimization, the interaction parameters between rRNA species is set to 0, i.e., $\chi_{i \in R, j \in R} = 0$, while the interaction between nucleolar components $\chi_{i \in N, j \in R}$ and between nucleolar and rRNA species $\gamma_{i \in N, j \in R}$ are free variables. The optimization results show that while it is possible to achieve full wetting in one system and partial wetting in the other (e.g., $\gamma^{(1)}{}_{DFC,GC} + \gamma^{(1)}{}_{GC,NP} = \gamma^{(1)}{}_{DFC,NP}$ and $\gamma^{(2)}{}_{DFC,GC} + \gamma^{(2)}{}_{DFC,NP} < \gamma^{(2)}{}_{GC,NP}$), it fails to find a set of parameters that achieve full wetting in both systems with different orderings of DFC and GC. This indicates that the pairwise Flory-Huggins model is insufficient to explain the change of nucleolus from a normal to an inverted morphology as a result of rRNA processing.

These results motivate us to consider a higher-order model that includes the interaction terms between three components. This correction is not merely a mathematical construction, but also stems from the physics of three-body interaction that is reflected in the third virial coefficient. Specifically, we consider the following free energy density

$$\frac{g}{k_B T} = \sum_{i \in N \cup R} \frac{1}{N_i} \phi_i \ln \phi_i + \frac{1}{2} \sum_{ij \in N, k \in R} (\chi_{ij} + w_{ijk} \phi_k) \phi_i \phi_j + \sum_{i \in N, k \in R} \chi_{ik} \phi_i \phi_k. \quad (6)$$

The new three-body term indicates that rRNA species can directly control the effective interaction between two nucleolar compartments and hence the surface tension. When $w_{ijk} > 0$ ($w_{ijk} < 0$), rRNA species k increases (decreases) the surface tension between i-rich and j-rich phases. The pairwise interaction between rRNA and nucleolar species dictates the partitioning of rRNA. For simplicity, we set the degrees of polymerization as $N_i = N_n, i \in N$ and $N_i = N_r, i \in R$. To simplify the model, we assume that the concentration of rRNA is low compared to that of the nucleolar components and define normalized rRNA volume fraction to be $\tilde{\phi}_k = \phi_k / \phi_0$, where ϕ_0 is a characteristic volume fraction of rRNA such that $\tilde{\phi}_k \sim O(1)$ and $\phi_0 \ll 1$. As a result, the

normalization condition for the volume fractions is approximately $\sum_{i \in N} \phi_i = 1 - \phi_0 \sum_{k \in R} \tilde{\phi}_k \sim O(1)$. We then define normalized interaction parameters $\tilde{\chi}_{ij} = \chi_{ij} N_n \ (i, j \in N)$, $\tilde{w}_{ijk} = w_{ijk} \phi_0 N_n \ (i, j \in N, k \in R)$, $\tilde{\chi}_{ik} = \chi_{ik} N_r \ (i \in N, k \in R)$. Therefore, Eq. (6) becomes

$$\frac{g}{k_B T} = \frac{1}{N_n}\left(\sum_{i \in N} \phi_i \ln \phi_i + \frac{1}{2}\sum_{ij \in N, k \in R} (\tilde{\chi}_{ij} + \tilde{w}_{ijk}\tilde{\phi}_k)\phi_i\phi_j\right) + \frac{\phi_0}{N_r}\left(\sum_{k \in R} \tilde{\phi}_k \ln (\phi_0 \tilde{\phi}_k) + \sum_{i \in N, k \in R} \tilde{\chi}_{ik}\phi_i\tilde{\phi}_k\right). \quad (7)$$

Note that the term involving $\ln \phi_0$ does not influence the phase diagram and surface tension because it is a linear term with respect to $\tilde{\phi}_k$. For simplicity, we set $\frac{1}{N} = \frac{\phi_0}{M}$.

Because $\tilde{\chi}_{ij} \ (i, j \in N)$ and $\tilde{w}_{ijk} \ (i, j \in N, k \in R)$ primarily control the surface tensions and $\tilde{\chi}_{ik} \ (i \in N, k \in R)$ primarily controls the affinity of rRNA to nucleolar components, these interaction parameters can be set based on the experimentally observed nucleolus morphology and rRNA partitioning. Table 1 displays the parameters used in our subsequent simulations.

Pairwise interaction parameters between nucleolar species $\tilde{\chi}_{ij} \ (i, j \in N)$			
(i, j)	(DFC, NP)	(GC, NP)	(DFC, GC)
	3	2.1	2.5
Three-body interaction parameters between rRNA and nucleolar species $\tilde{w}_{ijk} \ (i, j \in N, k \in R)$			
k (i,j)	(DFC, NP)	(GC, NP)	(DFC, GC)
Unprocessed 18S	-0.6	1	-1.6
Processed 18S	2.3	-2.5	-0.6
28S	0	1	1
Pairwise interaction parameters between rRNA and nucleolar species $\tilde{\chi}_{ik} \ (i \in N, k \in R)$			
	DFC	GC	NP
Unprocessed 18S	-1	-0.4	0
Processed 18S	0.8	-1	0
28S	0	-1.05	0.15

Table 1 Interaction parameters used in the simulations

Because rRNA is a non-phase-separating species with low concentration, we omit the contribution of the energy associated with its gradient. Hence for a spatially heterogeneous system, the total free energy is

$$G = c_0 \int \left(g + \frac{1}{2}\kappa \sum_{i \in N} |\nabla \phi_i|^2\right) dV \quad (8)$$

We define normalized quantities, $\tilde{g} = gN/(c_0 k_B T)$, $\tilde{G} = GN/(c_0 k_B T)$, $\tilde{\kappa} = \kappa N/(k_B T)$, and the dimensionless chemical potentials

$$\tilde{\mu}_i \equiv \frac{\delta \tilde{G}}{\delta \phi_i} = \frac{\partial \tilde{g}}{\partial \phi_i} - \frac{\partial \tilde{g}}{\partial \phi_{NP}} - \tilde{\kappa}(\nabla^2 \phi_i - \nabla^2 \phi_{NP}) \ (i = DFC, GC), \quad (9)$$

$$\tilde{\mu}_k \equiv \frac{\delta \tilde{G}}{\delta \tilde{\phi}_k} = \frac{\partial \tilde{g}}{\partial \tilde{\phi}_k} \ (k \in R), \quad (10)$$

where the Laplacian term involving ϕ_{NP} is due to the normalization condition $\phi_{NP} = 1 - \phi_{DFC} - \phi_{GC}$.

Based on the parameters in Table 1, we calculate the surface tension between phases at equilibrium for some typical average compositions that represent the normal, inversion, transcription-inhibited, and SSU-only plasmid phenotypes, as shown in Table 2. Note that in the normal phenotype (wild type), the ratio of unprocessed 18S to processed 18S rRNA is 0.1:0.9, consistent with the kinetic modeling results. The average volume fractions of the nucleolar components are kept the same across all simulations. From Table 2, we see that the normal phenotype satisfies $\gamma_{DFC,NP} = \gamma_{DFC,GC} + \gamma_{GC,NP}$. In 1D simulations, this corresponds to a complete GC wetting at the DFC-NP interface. In contrast, the inversion phenotype satisfies $\gamma_{GC,NP} = \gamma_{DFC,GC} + \gamma_{DFC,NP}$, which corresponds to a complete DFC wetting at the GC-NP interface. Moreover, we find that $\gamma_{DFC,NP}$ and $\gamma_{GC,NP}$ is higher for the inversion phenotype than the normal phenotype, consistent with the observation that the nucleoli fuse upon U3 ASO treatment. It is also consistent with the experimental observation that the nucleoli under the mutant SSU only plasmid where 5'ETS cleavage is disrupted have a higher sphericity than the normal SSU only plasmid. In contrast, $\gamma_{DFC,GC}$ is lower for the inversion phenotype than the normal phenotype, and the DFC phase in the inversion phenotype shows more DFC-GC mixing than that in the normal phenotype, consistent with experimental observations. The SSU only plasmid does not have a GC phase, instead, GC is about equally distributed in the DFC and NP phases.

Typical average composition	Normal phenotype	Inversion phenotype	Transcription inhibited	SSU only
ϕ_{DFC}	0.12	0.12	0.12	0.12
ϕ_{GC}	0.32	0.32	0.32	0.32
$\tilde{\phi}_{u18S}$	1.5	1	0.18	0.6
$\tilde{\phi}_{p18S}$	1	0.01	0.12	0.4
$\tilde{\phi}_{28S}$	1	0.75	0.3	0.01
Normalized surface tension	Normal morphology	Inversion morphology	Transcription inhibited	SSU only
$\gamma_{DFC,NP}$	0.755	0.769	0.240	0.311
$\gamma_{GC,NP}$	0.302	0.970	0.194	NaN

$\gamma_{DFC,GC}$	0.453	0.201	0.119	NaN
Equilibrium composition (ϕ_{DFC}, ϕ_{GC})	Normal morphology	Inversion morphology	Transcription inhibited	SSU only
DFC phase	0.589, 0.406	0.516, 0.464	0.738, 0.170	0.577, 0.383
GC phase	0.002, 0.660	0.028, 0.966	0.089, 0.742	NaN
NP phase	0.006, 0.032	0.032, 0.030	0.075, 0.178	0.023, 0.307
Equilibrium composition $(\tilde{\phi}_{u18S}, \tilde{\phi}_{p18S}, \tilde{\phi}_{28S})$	Normal morphology	Inversion morphology	Transcription inhibited	SSU only
DFC phase	3.262, 0.579, 0.901	1.959, 0.009, 0.628	0.396, 0.045, 0.230	1.352, 0.212, 0.010
GC phase	1.096, 1.806, 1.304	1.040, 0.019, 1.420	0.205, 0.193, 0.440	NaN
NP phase	1.040, 0.587, 0.819	0.687, 0.007, 0.533	0.151, 0.100, 0.255	0.441, 0.440, 0.010

Table 2. Equilibrium properties of different phenotypes. The normalized surface tension is defined to be $\tilde{\gamma}_{ij} = \gamma_{ij}/\left(c_0 k_B T N^{-1}\sqrt{\tilde{\kappa}}\right)$

B. Dynamic model

Next, we proceed to model the nonequilibrium process in the nucleolus. To capture the essential physics, we consider and simplify two major pathways of rRNA synthesis that produce SSU and LSU in parallel. The SSU pathway is simplified to consist of one intermediate, that is, an unprocessed 18S is produced and then converted into a processed 18S in the DFC with rate coefficient $k_{0,18S}$ and k_c, respectively. The LSU pathway omits all processing steps, i.e. 28S is produced in the DFC with rate coefficient $k_{0,28S}$. The production rates for the SSU and LSU pathways are assumed to be equal ($k_{0,18S} = k_{0,28S} = k_0$) except for the SSU-only plasmid, for which there is no 28S production. All rRNA species degrade and are exported from the NP with rate constant $k_{d,i}$. All reactions are assumed to follow first-order reaction kinetics. All components are assumed to have the same normalized mobility constant L. The normalization of the mobility constant absorbs all constants from normalizing the chemical potential. DFC and GC nucleolar species are chemically inert and they follow

$$\frac{\partial \phi_i}{\partial t} = L\nabla^2 \tilde{\mu}_i \ (i = DFC, GC). \quad (8)$$

The normalized volume fraction of rRNA components satisfy

$$\frac{\partial \tilde{\phi}_{u18S}}{\partial t} = L\nabla^2 \tilde{\mu}_{u18S} + k_{0,18S}\phi_{DFC} - k_c\phi_{DFC}\tilde{\phi}_{u18S} - k_{d,u18S}\phi_{GC}\tilde{\phi}_{u18S} , (9)$$

$$\frac{\partial \tilde{\phi}_{p18S}}{\partial t} = L\nabla^2 \tilde{\mu}_{p18S} + k_c \phi_{DFC}\tilde{\phi}_{u18S} - k_{d,p18S}\phi_{GC}\tilde{\phi}_{p18S}, \qquad (10)$$

$$\frac{\partial \tilde{\phi}_{28S}}{\partial t} = L\nabla^2 \tilde{\mu}_{28S} + k_{0,28S}\phi_{DFC} - k_{d,28S}\phi_{GC}\tilde{\phi}_{28S}. \qquad (11)$$

We define a reaction-diffusion length scale based on the production of 18S and 28S, $l_d = \sqrt{L/(k_0 \phi^{(DFC)}_{DFC})}$, where $\phi^{(DFC)}_{DFC}$ is the volume fraction of DFC nucleolar species in the DFC phase in the normal phenotype as tabulated in Table 2. Given the reaction-limited assumption in the kinetic modeling, we set $l_d/L_0 = 5$, where L_0 is the size of the domain. We define the characteristic time scale $t_* = (k_{d,28S}\phi^{(GC)}_{GC})^{-1}$, where $\phi^{(GC)}_{GC}$ is the volume fraction of GC nucleolar species in the GC phase in the normal phenotype as tabulated in Table 2. The characteristic interfacial width relative to the domain size is set to be $\sqrt{\tilde{\kappa}}/L_0 = 0.02$. The relative ratios of the rate constants in the normal phenotypes are determined by the overall mass balance based on the equilibrium states computed based on the average composition in Table 2. The transcription-inhibited phenotype has a lower production rate than the normal phenotype. The 28S degradation rate is lowered slightly to prevent dissolution of the GC phase due to the lack of 28S. Compared to the normal phenotype, all rate constants of the inversion phenotype remain the same except for the processing rate constant $k_c = 0$, all rate constants of the SSU-only plasmid remain the same except for the production rate of 28S $k_{0,28S} = 0$.

Phenotype	18S production rate constant $k_{0,18S}/k_0$	28S production rate constant $k_{0,28S}/k_0$	18S processing rate constant k_c/k_0
Normal	1	1	0.024
Inversion	1	1	0
Transcription inhibited	0.235	0.235	0.024
SSU only	1	0	0.024
Phenotype	Unprocessed 18S degradation rate constant $k_{d,u18S}/k_0$	Processed 18S degradation rate constant $k_{d,p18S}/k_0$	28S degradation rate constant $k_{d,28S}/k_0$
Normal	0.295	0.019	0.234
Inversion	0.295	0.019	0.234
Transcription inhibited	0.295	0.019	0.181
SSU only	0.295	0.019	0.234

Table 3 Reaction rate constants used in the following dynamics simulations

Based on the parameters above, we perform simulations for the different phenotypes based on the average composition in Table 2 and obtain the steady-state solution as shown in Fig. 1. The results agree with the morphology and rRNA partitioning observed in experiments.

Next, we perform perturbation simulations that cause the system to transition from one state to the other. In one case, we start from the steady state of the normal phenotype as the initial condition and at t = 0, the rate constants are switched to those of the inversion phenotype, in order to simulate the process of U3 ASO treatment. Fig. 2 shows that the average concentration of unprocessed 18S increases while that of the processed 18S decreases, correspondingly the snapshots below show that the DFC phase first moves to the edge of the GC, and then gradually envelops GC. In another case, we start from the steady state of the normal phenotype and switch the rate constants to those of the transcription-inhibited phenotype to simulate the CX treatment. Fig. 3 shows that the concentrations of all rRNA species decrease and the simulation shows that DFC moves to the edge of the GC.
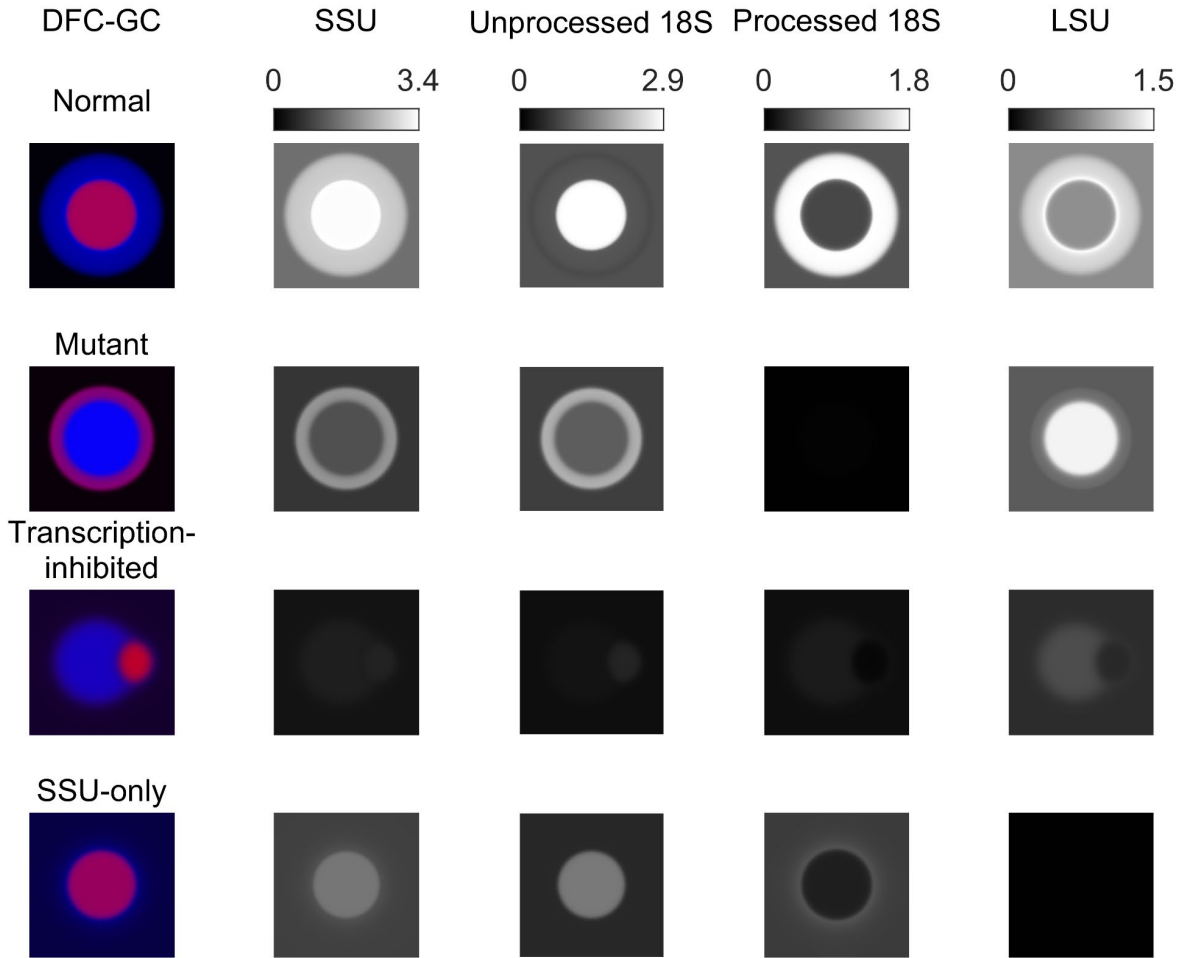

Figure 1. Nucleolus simulation (based on Eqs. (9)-(11)) at nonequilibrium steady state for some typical phenotypes whose average compositions are given in Table 2. From left to right, the images are DFC-GC merged (where the RGB values are $R = \phi_{DFC}, G = 0, B = \phi_{GC}$), total SSU normalized concentration ($\tilde{\phi}_{u18S} + \tilde{\phi}_{p18S}$), the normalized concentrations of unprocessed and processed 18S, and that of 28S (LSU), separately.
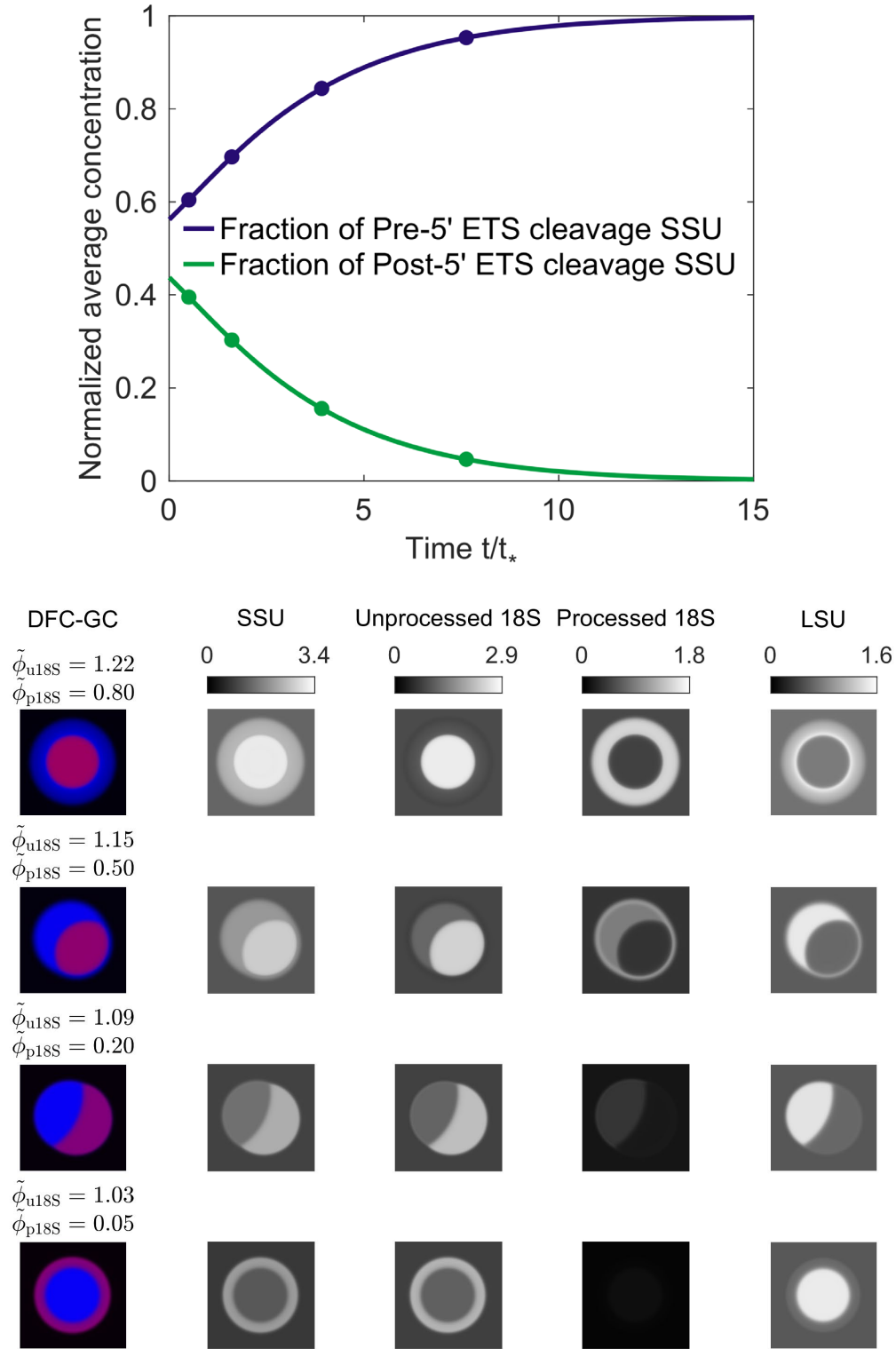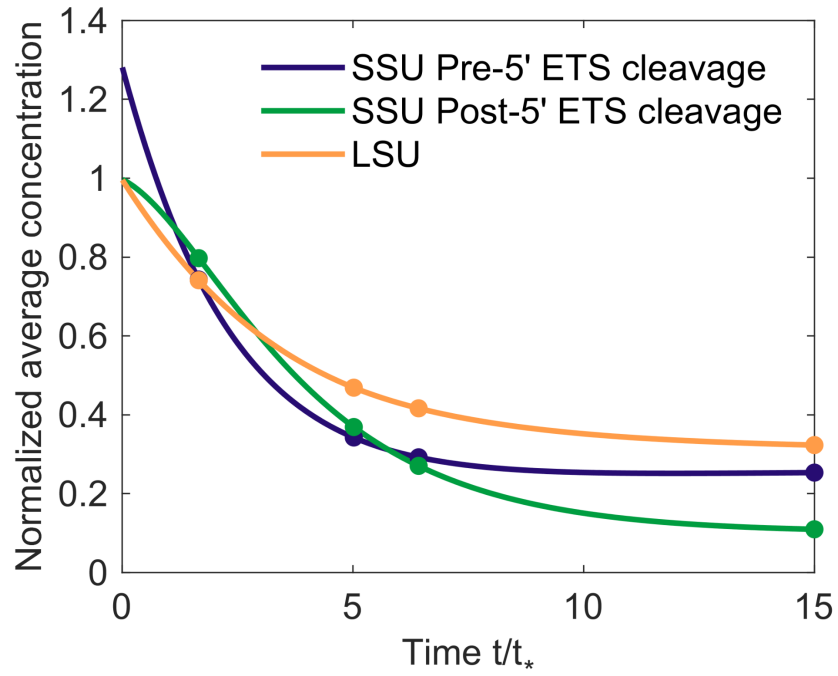
Figure 2 (a) Evolution of the normalized average concentration of unprocessed and processed 18S over time. The system is initialized at the normal phenotype steady state as shown in Fig. 1. At t = 0, the processing 18S is turned off. (b) Snapshots of the nucleolus morphology and

rRNA distribution over time from top to bottom. The system at t=0 and $t/t_* \to \infty$ are the same as the steady state profiles of the normal and inversion phenotypes in Fig 1 and hence not shown. Snapshots are taken at time points that correspond to the circles in (a).
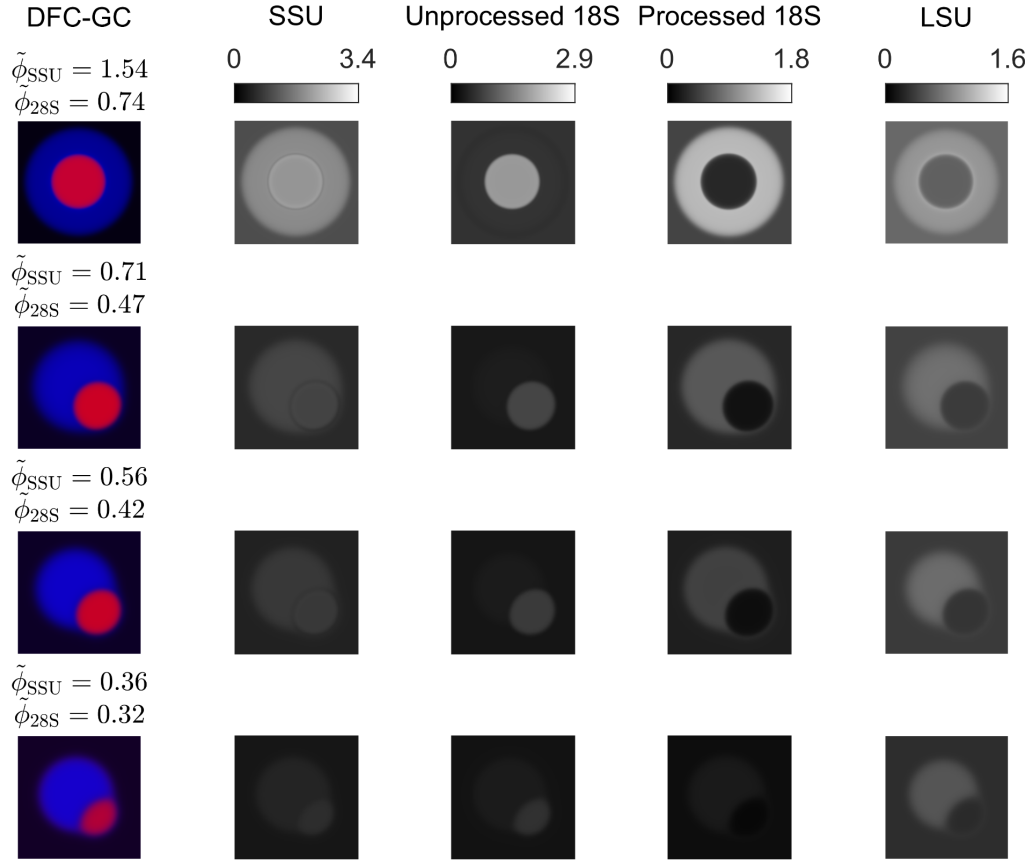
Figure 3 (a) Evolution of the normalized average concentration of SSU ($\tilde{\phi}_{u18S} + \tilde{\phi}_{p18S}$) and 28S over time. The system is initialized at the normal phenotype steady state as shown in Fig. 1. At t = 0, the production of 18S and 28S is turned off. (b) Snapshots of the nucleolus morphology and rRNA distribution over time from top to bottom. The system at t=0 and $t/t_* \to \infty$ are the same as the steady state profiles of the normal and transcription-inhibited phenotypes in Fig 1 and hence not shown. Snapshots are taken at time points that correspond to the circles in (a)

References

1. Mao, S., Kuldinow, D., Haataja, M.P. and Košmrlj, A., 2019. Phase behavior and morphology of multicomponent liquid mixtures. *Soft Matter*, *15*(6), pp.1297-1311.
2. Mao, S., Chakraverti-Wuerthwein, M.S., Gaudio, H. and Košmrlj, A., 2020. Designing the morphology of separated phases in multicomponent liquid mixtures. *Physical review letters*, *125*(21), p.218003.

Supplementary Note 3
We note that 18S* rRNA expressed from the SSU-only plasmid exports successfully to the cytoplasm, suggesting that the GC may not be needed for SSU processing. However, we cannot exclude the possibility that these SSU particles undergo further processing in the GC of adjacent native nucleoli or hybrid nucleoli.

Supplementary Note 4
Notably, the defect in cytoplasmic LSU export cannot be rescued by co-transfecting LSU-only and SSU-only plasmids. Consistent with this, there is also no detectable cytoplasmic 28S* rRNA signal in cells with or in "hybrid" nucleoli. This demonstrates that LSU assembly remains compromised even when LSU-only plasmids fuse with endogenous nucleoli and are in proximity with endogenous SSU precursors, suggesting that LSU rRNA must be co-transcribed with SSU rRNA for proper LSU assembly (Extended Data Fig. 8g-h).